AD-A241 619

Technical Report 1370
November 1990

# Eigenvalues of Covariance Matrix for Two-Source Array Processing

S. I. Chou

91-12889

# NAVAL OCEAN SYSTEMS CENTER
## San Diego, California 92152-5000

J. D. FONT NA, CAPT, USN
Commander

H. R. TALKINGTON, Acting
Technical Director

## ADMINISTRATIVE INFORMATION

## ACKNOWLEDGMENT

MA

# Summary

We begin this report with a survey of direction-finding algorithms restricted to the narrowband case in element space. We then set out to search for a simple satisfactory stress measure to direction-finding algorithms applied to scenarios with two sources. The word "stress" for a scenario is used to indicate the difficulty that an algorithm has in determining the direction of arrival of each of the two sources. A scenario is said to be "stressful" to an algorithm if it causes difficulty in resolving the sources or in determining their directions of arrival. The apparent lack of understanding of the effect of phase difference between two signals in direction-finding made such an ideal stress measure illusive. Regardless of all its deficiencies, eigenvalue ratio is still a useful measure in summarizing stressing factors in many aspects for two-arrival direction-finding scenario.

Eigenvalue weighting appears in some noise subspace methods, in parametric signal subspace fitting methods, and in nonparametric subspace adaptive nulling beamforming. For a two-source array-processing scenario, normalized large and small eigenvalues $\lambda_1$ and $\lambda_2$ are reduced to forms depending only on a real triplet: phase-dependent variable $\xi$, phase-independent variable $\eta$, and power ratio $\frac{\pi_1}{\pi_2}$. The pairs $(\xi, \eta)$ are confined to an isosceles-like region. We characterize
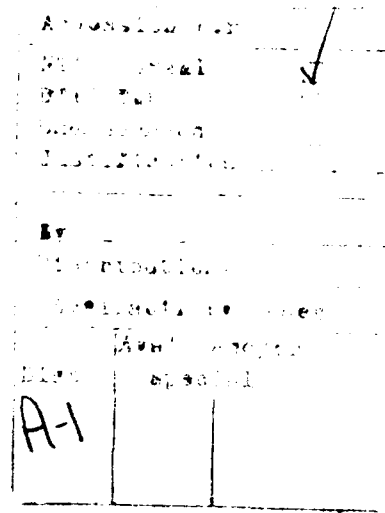
- this isosceles-like region and the many-to-one mapping from the Cartesian product of the temporal and spatial correlation unit-disks onto this region,

- the behavior of the eigenvalues and their ratios as functions of the real triplet both analytically and graphically with respect to direction-finding.

The main contribution of this work is a manageable presentation of a compact map showing $\lambda_1$, $\lambda_2$, and $\frac{\lambda_1}{\lambda_2}$ as functions of $\xi$, $\eta$, and $\frac{\pi_1}{\pi_2}$ over all possible scenarios. This enables one to see the relative positions among different scenarios. We also present some easy-to-remember formulas that enable one to exercise "back-of-envelope" assessment of scenarios.

The small eigenvalue is shown to diminish qualitatively and quantitatively for two-arrival scenarios increasingly stressed with high temporal and/or spatial correlations. The special case of equal-strength signal arrivals ($\frac{\pi_1}{\pi_2} = 1$), also important in low-angle radar tracking, shares many rich structures of general $\frac{\pi_1}{\pi_2}$. The equal-strength case also has several additional unique features for signal eigenvalue ratio $\frac{\lambda_1}{\lambda_2}$, which is important in direction-finding:

- an extra 6 dB over the vertical axis $\xi = 0$ as compared to the general $\frac{\pi_1}{\pi_2}$ case,

- a 6-dB increase for equipower arrivals highly correlated both temporally and spatially from changing the angle difference between the two unit-disk vectors from 90°(orthogonal waveforms) to 0°(in-phase waveforms),

- the lower left corner of the isosceles-like triangle is a point of discontinuity for the eigenvalue ratio $\frac{\lambda_1}{\lambda_2}$.

The developed results are used to assess some scenarios used by Cadzow and Ottersten.

# Contents

# Appendix

# List of Figures

# List of Tables

# Chapter 1

# Introduction

High-resolution algorithms for direction-finding (DF) using general array configurations are still maturing. For the parametric approach to the narrowband (NB) problem in element space, some consensus appears to be emerging. Therefore, the scope of this report on direction-finding is restricted to the narrowband case in element space.

Because of the different scenarios used among the reported analytic or simulation performance results, the evaluation of the various high-resolution NB DF algorithms is made difficult by the lack of a common footing in relating and assessing them. The possible combination of all parameters to specify scenarios to test and evaluate candidate algorithms is just too vast. Even if one conducts such an exhaustive evaluation, the effective presentation of results poses another problem. The lack of any simple yardstick to measure some sort of scenario stress makes it difficult to effectively grasp the different reported results and to form a broad brush mental picture summarizing the very complicated scene. The word "stress" for a scenario is used to indicate the difficulty that an algorithm has in determining the direction of arrival of each of the two sources. A scenario is said to be "stressful" to an algorithm if it causes difficulty in resolving the sources or in determining their directions of arrival. From a DF user's point of view, it is highly desirable to have some guidelines developed to help draw an envelope of scenario parameters corresponding to a potential stressful operating environment.

We limit the scope of our attempt to search of yardsticks measuring stress of DF scenarios to only two sources. This is because of the ease of obtaining a measure to evaluate scenarios by dealing with only solutions of quadratic characteristic equation and that most of the reported simulation results in the literature involve only two-source scenarios. Even then some non-negligible effort is required to display such results.

So far, we found such a stress measure illusive. The effect on direction-finding of the phase difference between two signals' source amplitudes is apparently not a well-understood subject. When this phase difference does not come into play in the eigenvalue expressions, such as when the two arrivals are temporally uncorrelated or spatially orthogonal, eigenvalue ratio seems to be a plausible stress measure. A large value of the eigenvalue ratio will reflect the cumulative effect of large magnitudes of the normalized spatial and temporal correlation coefficients and the power ratio of the two arrivals. Most reporting on the phase difference effect is for the low-angle radar tracking problem with two closely spaced, coherent, equipowered plane-wave arrivals impinging on a uniform line array. In examining candidates for stress measures, we have considered eigenvalue ratio, Cramer-Rao lower-bound (CRLB), and asymptotic performance results of some subspace algorithms for such scenarios. Somehow we cannot reconcile all the differences among these candidates together with our physical intuition.

1

In conducting the illusive search for a simple satisfactory stress measure for scenarios to direction-finding algorithms, we start the main body of chapter 1 with a survey of narrowband DF algorithms for general sensor arrays in element space. This includes a taxonomy table, characterization and asymptotic performance of the main algorithm categories, and the initialization procedure, which is the critical item of most high-resolution algorithms. Then, the idea of formulating guidelines desired for DF scenario design is developed for the following: too many parameters for a two-source DF scenario for a given sensor array, simple map(s) to show relative positions of scenarios and yardstick for measuring stress of scenarios to direction-finding algorithms, and dominant eigenvalues chosen as the key items. Next, we discuss eigenvalues for the noise-free covariance matrix of two discrete sources by considering the following issues: treatment of this subject in Hudson's text[23], the original 6-dimensional parameter space for a given sensor array under the noise-free assumption, compact map(s) — another many-to-one reduction, and 3-d map with the power ratio between the two arrivals as third coordinate.

Chapter 2 addresses the notion of stress to direction-finding algorithms and scenarios. First, the following three main sources for the signal eigenvalue spread or causes for small signal eigenvalues are reviewed: high spatial and/or temporal correlation and/or high contrast of signal strength between the two arrivals. Next, the eigenvalues in weighting expressions are discussed for three categories: noise subspace methods, parametric signal subspace fitting methods, and nonparametric subspace adaptive nulling beamforming. Then, the drawbacks of the oversimplifying stress-measuring yardstick using condition numbers are mentioned: infinite condition number for all 100%-correlated two arrivals, equal condition numbers corresponding to different CRLBs, CRLB not appealing to intuitive expectation, and the redeeming value for signal eigenvalue ratio. At the end, we explain the reasons why special treatment is given for equal-power arrivals.

During the course of this search of a good stress measure, we thoroughly characterized the eigenvalues and their ratio for two-source scenarios and came up with an effective way to present results. Chapter 3 is about the analytical characterization of eigenvalues for two arrivals. Chapter 4 is about the fractional beamwidth separation between two plane waves impinging on a uniform line array (ULA). Chapter 5 is about the plots of signal eigenvalues and their ratio in dB scale. The large and small eigenvalues as well as their ratio are functions of a phase-dependent variable and a phase-independent variable, both derived from the normalized spatial and temporal correlation coefficients, and the power ratio between the two arrivals. The main contribution of this report is a manageable presentation of a compact map showing these three functions over all possible scenarios. This enables one to see the relative positions among different scenarios. We also present some easy-to-remember formulas that enable us to exercise back-of-envelope assessment of scenarios during presentations or discussions.

These developed results are used to assess some scenarios used by Cadzow and Ottersten in chapter 6. Chapter 7 serves to conclude the main findings of this the report.

## 1.1 A Brief Survey of Narrowband DF Algorithms for General Sensor Arrays in Element Space

For the reader interested in the DF algorithms for general sensor arrays, a classification chart of some of the candidate narrowband algorithms is helpful. To this end, we provide table 1.1. Some brief discussions of this taxonomy table are provided in the following subsections. They are about characterization, performance, and implementations.

### 1.1.1 A Broad-Brush Taxonomy Table

Over-simplification and oversight is unavoidable, but this table serves as a starting point. Hopefully, the discussion will remedy some of the simplistic presentation. The reader is cautioned not to read too much into the performance comparison parts of this table. A single measure of resolution performance, sometimes based on asymptotic performance expressions and often evaluated subjectively, using symbols + or -, is employed here to compare entries in the same columns or rows. This appears strange as the report discusses a multitude of scenarios for even a two-arrival case. The measure is even less meaningful when entries not in the same column or row are compared. A broad-brush table such as this, together with only a few pages of discussion, definitely will not suffice for some workers in the field. The complexity involved in just comparing the simulation work from two researchers can be inferred by reading chapter 6, which is about some of Cadzow's and Ottersten's scenarios. One alternative is a similar large-scale study of such scope as the 1984 MIT/Lincoln Lab report [3].

### 1.1.2 Characterization of Some Algorithms

Ottersten and Viberg [34,35,36,38,59,60,61] jointly formulated a unified subspace fitting framework that relates several existing methods including Conventional BeamForming (CBF), MUltiple SIgnal Classification (MUSIC), multidimensional MUSIC, and Deterministic Maximum Likelihood (Det-ML). Directions of arrivals (DOAs) are estimated individually by CBF and MUSIC; i.e., by searching over a grid in a nonparametric fashion as is done by the Minimum Variance Distortionless Response (MVDR) Adaptive Beamforming (ABF) algorithms. DOAs are estimated jointly by multidimensional MUSIC and Det-ML by using parametric methods without a grid. Those using a grid cannot deal with coherent (100% correlation) arrivals for general array configurations.

The generalized MUSIC by Ferrara and Parks [18] for diverse polarizations, and by Haber and Zoltowski [21] for coherent multipath, is a hybrid of the above two categories but is still of the spectrum type; i.e., the search is over a product DOA parameter space. The dimension of the product space depends on the maximum number of multipaths modeled for the emitters within the coverage. For each grid point in the product domain, we consider all linear combinations of known multipaths corresponding to the product angle coordinates. The linear combination that has the minimum projection onto the noise subspace is found. The reciprocal of the magnitude-squared of this quantity is defined as the spectrum. The spectrum at each grid point involves the computation of the smallest generalized eigenvalue of a small matrix, the size of which is the number of multipaths modeled. The display and extraction of parameters for the generalized MUSIC are difficult when the dimension of the underlying parameter space for the product domain exceeds two, i.e., except for the simplest azimuthal-only scenarios having at most two multipaths from each emitter.

Even though we try to limit consideration to algorithms applicable to general array configurations and signal models, an exception is made for Estimation of Signal Parameters via Rotational Invariance Techniques (ESPRIT) [45,65]. This is because of the many attractive features of ESPRIT for doublet array configurations including the case of plane-wave arrivals impinging on a ULA. The main features are the simplicity of computation and the ability to provide signal parameter estimates in the absence of detailed knowledge of the sensor array characteristics. Because of the misconception that ESPRIT avoids the calibration problem entirely, Zoltowski and Stavrinides [65] comment that the required calibration involved in the doublet arrays is not a trivial task. The inherent redundancy built into the ideal ESPRIT array structure, which causes the degraded resolution for a ULA using Root MUSIC, can compensate for imperfect calibration

Element-Space Narrowband Direction-Finding Algorithms: A Summary Chart

| Category | Conventional Beamforming | Adaptive Beamforming | High Resolution Direction Finding | | | | | | |
|---|---|---|---|---|---|---|---|---|---|
| | | | Subspace Decomposition | | | | | Maximum Likelihood Estimation | |
| | | | Noise Eigenvector | | Signal Eigenvector | | | | |
| Name | CBF | ABF | MUSIC | ESPRIT | Generalized MUSIC | Signal Eigenvector SE | Weighted Sub-Space Fitting WSF | Deterministic Det-ML | Stochastic Sto-ML |
| Math | DOAs Separately Estimated Spectrum Search Over Grid | | | | In-Between | DOAs Parametrically & Jointly Estimated | | | |
| Character | Inner Product Only | Constrained Linear LS & Inner-Product | Inner-Product | Closed-Form Solution | Eigen-Decomposition | | | Whole Space (Not Subspace) | |
| | | | | | Small Size EVD | Nonlinear Least Squares | | Likelihood Maximization | |
| | | | | | Fitting Linear Comb of Steering Vectors with RHSs | | | | |
| ization | | | | | Perpendicular To Noise Eigenvctrs | SEs | Weighted SEs | Snapshot Data Vectors | |
| | | | | | | Over $\vartheta$ | | Over $\vartheta, P, \sigma$ | |

Spatial Smoothing

| | | x | x | x | + | ++± | +++ | ++ | +++ |
| | | ? | + | +? | ++ | ++± | +++? | ++? | +++? |
| | | | ++ | ++ | ++ | +++ | ++++ | +++? | ++-+ |

| Array Configuration | | | Doublet Array Plane Wave Only | | Legends: | $\vartheta$ | Direction of Arrival (DOA) Parameters | | |
| | | | | | | P | Source Covariance Matrix | | |
| Computation | ±? | | Root Music | | | $\sigma$ | Standard Deviation of White Noise | | |
| Application to Large Array | | | | No | | x | Incapable | | |
| | | | | | | + | Advantage | | |
| Art | | | | Further Restriction | | - | Disadvantage | | |
| | | | | | | ± | Can Be Either + or - | | |
| | | | | | | ? | Half a + | | |

| | | | +Calibration | | -Initial Estimates Costly & Critical | | | | |
| Key | | | +Computation | | Choice On # of SEs | | -Resolutn +Best | | |
| | | | +Coherency | | -Hard | +Tolerant | Worsening Resolution | | |
| | | | +Array Rest. | | Handling Diff SNRs | | At High- -Worst | | |
| | | | | | -Not So | +Good | Correlatn Computation | | |

Table 1.1: Narrowband direction-finding algorithms in element space: a summary chart.

so that corresponding sensors in the doublet arrays need be only approximately identical [65].

There are some convergence in thoughts about the MVDR, and the subspace or MUSIC algorithms, especially in the sonar community. This is discussed later in subsection 2.2.3.

### 1.1.3 Asymptotic Performance

The asymptotic properties of the parameter estimates from a general weighted fitting criterion were derived by Ottersten and Viberg, and by applying an appropriate weighting and parameterization, they obtained distributions of different estimators. They minimized the asymptotic variance with respect to the subspace weighting, leading to a novel method termed Weighted Subspace Fitting (WSF). They also examined the asymptotic behavior of the Stochastic Maximum Likelihood (Sto-ML) and the distribution is shown to be the same as for WSF. Therefore, WSF achieves the best resolution performance attainable by Sto-ML, which requires a nonlinear $(d^2 + d + 1)$-dim optimization where $d$ is the number of modeled arrivals for azimuthal problems, with the much smaller burden of only a $d$-dim one similar to that of Det-ML. For uncorrelated arrivals such as in matched-field processing (MFP), the $d^2$ term is reduced to $d$. For a plane-wave model with both azimuthal and elevation measurements, the original linear term $d$ becomes $2d$.

The MUSIC algorithm is a "one arrival at a time" search of the parameter space, and this inherently leads to a large bias due to the finite sample, which dominates the variance until the amount of data is very large. The multidimensional techniques (those using joint estimation of multiple arrivals) have a smaller bias and the asymptotic expressions can even be used for smaller samples.

The asymptotic performance analysis by Ottersten and Viberg patterned after Stoica and Nehorai [53,54,55] who had many results similar to those of Ottersten and Viberg. The Signal Eigenvector (SE) approach by Cadzow [6,7] uses only dominant eigenvectors. Therefore, according to Ottersten (private communication with the author of this report), its finite sample performance has nonzero bias and the mean square error may have the advantage of those of the reduced rank principle by Scharf and Tufts [47,48]; i.e., bias is traded for reduced variance. A paper has been submitted by H. Wang and G.H. Wakefield, on nonasymptotic performance analysis of eigenstructure-based direction-of-arrival estimation using perturbation theory.

### 1.1.4 Initialization: The Critical Item in Implementation

The jointly estimating types of algorithms, with the exception of Stochastic Maximum Likelihood Estimation (Sto-MLE), involve fitting a linear combination of steering vectors of unknown DOA parameters to data. They all solve a separable nonlinear least squares problem [20,26,46] or its equivalent, sometimes called reduced or concentrated form. They differ only in the right-hand sides of the fitting equations. For Deterministic Maximum Likelihood Estimation (Det-MLE), the right-hand sides are snapshot data vectors. For SE and WSF, the right-hand sides are the unweighted and weighted signal eigenvectors respectively. They can differ in performance considerably. Computationally, these approaches are similar to each other in that some Gauss-Newton algorithms, or their approximations, can solve the parameter fitting problem very well if a good initial estimate is available; i.e., one close to one of the global minimum (nonunique to within permutations). Note that the DOA parameters for the multiple emitters are estimated jointly as they correspond to a single point in the parameter space over which the least squares problem is carried out. This is contrasted to the spectrum estimation methods where each emitter's (or arrival's) parameter values are read off one at a time.

Getting a good initial estimate is definitely no small feat, as the cost function of the global minimum search has many relative or local minima. The abstract by Degerine as announced in the manuscripts in review of the August 1990 IEEE ASSP Transaction [14] has the following: The likelihood function, in estimating a Toeplitz covariance matrix, can present a local maximum close to the global maximum. An analytical proof is conducted for the matrices of order 3 and numerical examples are given for orders 3, 4, and 5.

Both Ottersten and Viberg, and Cadzow used the initialization scheme by Ziskind and Wax [63] to tackle this critical problem. The major share of the overall direction-finding computation is essentially from this initialization. Starting from a CBF to choose the first strongest arrival, the Gram-Schmidt orthogonal procedure is successively applied to form (multiple) null(s) at previously selected arrival(s) [23, pages 41-46] to choose the next strongest arrival. In a two-signal scenario we sized for azimuthal and elevation angle measurements for a Mill-cross array, the initial estimate is 99% of the total computation count.

There have been published works promoting the use of Expectation-Maximization (EM) algorithm or its variants for the direction-finding problem. While this was met with skepticism during off-the-record discussions, as usual such skepticism was not openly reported. But the recent dissertation by Wu [62] shows, through both simulation and theoretical analysis, that conventional methods such as the gradient and the Newton methods have more desirable performance in (local) convergence than the EM algorithm.

Note that the EM algorithm and its variant depend equally on the choice of a good initial estimate as do the more conventional methods. In fact, some of these EM numerical experiments such as in Wu's dissertation [62] used exactly the same Ziskind and Wax's algorithm to find an acceptable initial estimate. In a recent paper, Ziskind and Wax [64] incorporated some a priori periodicity structural information of the spatial covariance function for a ULA with uncorrelated arrivals in a Det-ML scheme. They obtained higher resolution than MUSIC but used these "lower" resolution algorithms to initialize the EM method. (Interestingly, Ziskind and Wax did not use the initialization scheme bearing their own names.) Lo, Nagaraj, and Rukhin [31] also used the Ziskind and Wax [63] initialization scheme in their DF algorithm using cyclic regression for WSF. While their claim of great reduction of computational complexity is highly debatable, they obtained interesting results by modifying Det-ML to achieve an asymptotically equivalent expression of the WSF criterion. We are somewhat sold on the principle of rank-reduction and still consider the rank-reduced version of the original WSF as the favored baseline candidate.

As the initialization is where resource should be allocated and the description of the most commonly used Ziskind and Wax's algorithm was terse, we characterize it here to provide insights. Hopefully, someone can provide less expensive alternatives in the future. Starting from a CBF to choose the first strongest arrival, the initialization continues in a recursive fashion using successive adaptive nulling. Suppose k-1 strongest arrivals have been selected. The next or the k-th strongest arrival is selected from the highest peak of the next adaptive nulling spectrum in the following way. The weight vector of the adaptive nulling at each grid point is made orthogonal to the steering vectors of all the k-1 strong arrivals previously selected to produce a distortionless response for an arrival with the DOA parameters corresponding to this grid point. Because of the adaptive nulling application, the resolution of this initialization is at least medium high, so a grid finer than that for the CBF is needed. Such orthogonal beamforming effectively subtracts out strong signals from sensor data by using orthogonal projection without performing the dangerous subtraction of large numbers. Ziskind and Wax used a projection matrix update formula based on sequential one-step application of the Gram-Schmidt procedure. As the simplicity of this algorithm derives from initializing or updating only one source's DOA parameters at each adaptive nulling scan, it

is similar to the coordinate descent method well-known in multivariate optimization. The original paper by Ziskind and Wax went beyond just initialization. The same procedure was proposed to continue cyclically, i.e., wrapping around the source indices: $1, \cdots, d$, if $d$ contacts are modeled. This DF algorithm proper has not been received well because of the exceedingly slow convergence rate, which is no surprise given the reputation of coordinate descent methods. However, the similarity between the coordinate descent and Ziskind and Wax's methods stops here, as Ziskind and Wax's initialization aims at a global multivariate search while coordinate descent method does not.

Some potential improvements on the Ziskind and Wax initialization scheme are obvious. For those sources interfering with each other at most marginally because of wide spatial separations and the lack of strength contrast, one may entertain the idea of selecting them simultaneously in one adaptive nulling scan. On the other hand, for a pair of nearby sources interfering with each other within a mainlobe, a fixed grid spacing throughout the sequential orthogonal beamforming may not serve the purpose well. We may refine the grid spacing near the selected strong sources so that potentially present nearby sources may be selected. We may also perturb the grid system locally by offsetting some grid lines because we cannot reuse for later adaptive nulling scans those old grid points already occupied by selected strong sources.

The delineation shown in the taxonomy chart between subspace DF and ABF is of broad-brush nature. For MUSIC-type algorithms, there are proposed implementations without the need to perform eigen-decompositions. The works by Munier and Delisle [33], Reilly, Chen, and Wong [43], and Friedlander [19] all appeared in 1988 within a short duration. On the other hand, the traffic is not just one-way. Clark and Roberts [12] advocated using rank-one eigenstructure updating in realtime ABF.

## 1.2   A Yardstick to Measure Stress of a Two-source Scenario Exacting on a DF Algorithm

### 1.2.1   Guideline Desired for DF Scenario Design

From the perspectives of High-Frequency Direction-Finding (HFDF) system development and the user's point of view, it is important to test and evaluate the various algorithms against realistic scenarios by using either measured or simulated data. These scenarios can be used to evaluate the relevancy and deficiency of the basic assumptions underlying algorithm development, and to calibrate simulation results. The cost of collecting measured data determines the number of scenarios possible. Therefore, guidelines are needed to select scenarios to meet the time and budget constraints for data collection and postanalysis.

### 1.2.2   Too Many Parameters for Two-Source DF Scenarios for a Given Sensor Array

Even for highly idealized scenarios with just two discrete sources and a given array with perfectly specified calibration, there are too many parameters to be exhaustively covered. These parameters are the two signal-to-noise ratios (SNRs), number of snapshots, source correlation coefficient, and DOAs of sources.

As a real data set is difficult to obtain and the understanding of algorithms are still maturing, a performance study using simulation is the only vehicle available for most algorithm investigators. For each chosen set of the above mentioned parameters, a large Monte Carlo simulation is

needed to evaluate each candidate algorithms with their various algorithm settings. Analytical performance predictions, when available, can significantly reduce the cost of such Monte Carlo simulations and sometimes provide understanding of the algorithms not possible to obtain by simulation. Even then, the number of possible scenarios makes comparison of algorithms difficult.

### 1.2.3 Simple Map(s) to Show Relative Positions of Scenarios and Yardsticks for Measuring Stress of Scenarios to Direction-Finding Algorithms

Typically, each author of a particular algorithm tends to present scenarios favorable to the algorithms he or she (re)invented. Objectivity and modesty is not pervasive. Even for the many well-conducted comparisons separately conducted, it is difficult to relate these seemingly "apple and orange" scenarios. Because of the bodies of reported results available in the literature and the cost of duplicating such tests for even limited standardized scenarios, we settle for a combination of simple map(s) and a realistic yardstick. We mentioned earlier that there are too many parameters to be covered for even a two-source scenario. The compact map or maps will enable us to show, on some common footing, the relative positions of the noise-free version of the various scenarios already reported or yet to be used. The yardstick is intended for measuring the stress factor of the scenarios presented to the DF algorithms already reported or two-source simple scenarios to be planned in the future. Such a measure does not account for the cost issues, such as operation count or implementation ease, which are very important algorithmic issues in a DF system. But it connects to the issues related to resolution or standard deviation of the DOA estimates when the noise floor is considered. The relative level of the noise floor is determined by the SNR and the number of snapshots available.

Hopefully, we can relate a sonar scenario using a 3-d random array with azimuth and elevation angle measurements reported in one publication to a HF scenario using ULA with azimuth measurement only reported in another publication. We leave the actual performance evaluation of the various candidate algorithms to either analytical or numerical methods reported or yet to be carried out. What we provide is a common footing for comparing the noise-free versions of one scenario to another using a stress measure.

### 1.2.4 Dominant Eigenvalues Chosen as the Key Items

The key components of a DF problem are the detection and estimation of dominant arrivals. Evidence appeared recently that the WSF approach is the leading candidate for a baseline high-resolution HFDF algorithm for a general sensor array. Furthermore, Viberg and Ottersten have provided a unified frame for the many subspace and Det-MLE algorithms.

The various algorithms are different in this unified frame in the weights used. These weights are expressions of the eigenvalues of the data covariance matrices. To this end, we investigated the eigenvalues for noise-free two-source problems.

## 1.3 Eigenvalues for the Noise-Free Covariance Matrix of Two Discrete Sources

### 1.3.1 Treatment of this Subject in Hudson's Text

Hudson's text on ABF contains a four-page section[23, pages 52-55] on the eigenvalues for the data covariance matrix of two discrete sources. He provides the general formula of the two eigenvalues

and some special case treatment. Apparently, eigen-decomposition methods were not mature then, the treatment did not realize its full potential. Here we interpret Hudson's expressions differently and use graphs from our yardstick's point of view to provide compact maps to relate the various scenarios and to provide a "stress" measure that can ultimately cause some algorithms to break down in the standard deviation performance of their DOA estimates. We adhere as much as possible to Hudson's original notations in his four-page treatment.

## 1.3.2 The Original Six-Dimensional Parameter Space for a Given Sensor Array under the Noise-Free Assumption

For a given sensor array with noise-free assumption for two sources, the eigenvalues depend upon the following six parameters:

- $\pi_1$ and $\pi_2$, signal powers for signals 1 and 2 with $\pi_1 \geq \pi_2$

- $\rho$, normalized multipath correlation coefficient between the two signals' complex amplitude, a complex number constrained on a unit-disk,

- $\phi$, normalized spatial correlation coefficient between the two arrivals' steering vectors, also a complex number constrained on a unit-disk.

For simplicity, we may assume that the eigenvalues have been scaled with respect to the product of the number of sensors and $\pi_2$. This way, we reduce the number of parameters to five; i.e., $\frac{\pi_1}{\pi_2}$ and an element from a four-dimensional region formed by the Cartesian product of two unit-disks. We have achieved a many-to-one mapping from the set of all possible noise-free scenarios to the admissible set of five parameters.

While we let the point on each unit-disk be arbitrary, this may not be the case for specific scenarios. In the case of the spatial correlation disk for a ULA with a given number of elements, the normalized complex inner product of two steering vectors is a (real) sinc function with an associated phase term. The modulus and argument are related in some way and together trace out a curve on the polar plot on the unit-disk. Such curves depend upon the number of sensors used. Similar cases may be made on the multipath correlation unit-disk, perhaps by using some argument from ray-tracing or other propagation models. Also, we will see that the stress factor is not a strong function of the phase terms when the strength ratio is away from unity.

While this mapping from an arbitrary sensor scenario to a five-dimensional data point in the parameter space accomplishes a significant reduction, it is still not easy to gain insight of the problem. Hudson considered some important special cases, but several important features were left out.

## 1.3.3 Compact Map(s): Another Many-to-One Reduction

In the following, we provide an additional many-to-one mapping such that for a given value of the strength ratio $\frac{\pi_1}{\pi_2}$, the Cartesian product of the two unit-disks can be mapped into an isosceles-like region in two new parameters. The two new parameters are:

$$\xi = |\rho||\phi| \cos(\arg \rho - \arg \phi),$$

$$\eta = (1 - |\rho|^2)(1 - |\phi|^2).$$

For convenience, we call $\eta$ the phase-independent variable and $\xi$ the phase-dependent variable. The rationale for the names is provided in section 3.1.

9

Note the symmetry between $\rho$ and $\phi$ in the above expressions. Given $\pi_1$ and $\pi_2$, they are the only expressions needed in computing the general formula for the two eigenvalues. These two new parameters are not entirely independent of each other as will be explained in detail later. This is in contrast to the original six parameters, which could be varied independently with some minor qualifying remarks.

We can further identify points corresponding to the following four special cases that were pointed out by Hudson:

- Arrivals 0% correlated with respect to both multipath and steering vectors,

- Arrivals 0% correlated with respect to either multipath or steering vectors but not to both,

- Arrivals 0% correlated with respect to either multipath or steering vectors and 100% correlated with respect to the other,

- Constructive interference with the two arrivals 100% correlated with respect to both multipath and steering vectors with cosine term $+1$.

Because of the nature of this many-to-one mapping, the same $(\xi, \eta)$ point can come from several different special cases in the original four-dimensional parameter region that is a Cartesian product of two unit-disks. For example, the point $(\xi, \eta) = (0,0)$ corresponding to the special case:

Arrivals 0% correlated with respect to either multipath or steering vectors and 100% correlated with respect to the other,

also corresponds to the following special case:

"Quadrature summed" interference with the two arrivals 100% correlated with respect to both multipath and steering vectors with zero phase-difference term; i.e., the two multipath sources are in the same direction but are 90° out of phase.

The vertical symmetry line, $\xi = 0$, corresponding to the special cases:

Arrivals 0% correlated with respect to either multipath or steering vectors but not to both

also corresponds to the following special cases:

Arrivals with the phasor directions on the two unit-disks perpendicular to each other; i.e., $\arg \rho - \arg \phi = 90°$.

Hudson also ignored the important special case:

Destructive interference with the two arrivals 100% correlated with respect to both multipath and steering vectors and with the cosine term $-1$.

The whole baseline of the isosceles-like region can be interpreted as special cases with the two arrivals 100% correlated with respect to either multipath or steering vectors. It can also be interpreted as special cases with the two arrivals 100% correlated with respect to both the multipaths and steering vectors in addition to having a proper valued cosine term. We note that Hudson unnecessarily restricted this just mentioned special case to the single point corresponding to the constructive interference.

10

We also provide the characterizations with respect to the cosine term in the $\xi$-definition. The right-half of the isosceles region corresponds to arrivals with the phase on the two unit-disks differing less than 90°. The left-half of the isosceles region corresponds to arrivals with the phase on the two unit-disks differing more than 90°.

Later in figure 3.2, we will see that Hudson's textbook presented 4 out of the 17 characterizations shown there. These 4 cases are denoted by asterisks.

### 1.3.4   A 3-D Map with Power Ratio $\frac{\pi_1}{\pi_2}$ as the Third Coordinate?

We can add the ratio $\frac{\pi_1}{\pi_2}$ as the third coordinate. However, the observations made after examining the three surfaces of $\lambda_1$, $\lambda_2$, and their ratio indicate that their dependence of $\frac{\lambda_1}{\lambda_2}$ on the ratio $\frac{\pi_1}{\pi_2}$ is essentially translational in the dB scale especially away from the unity ratio base plane. Therefore, the treatment of the parameter $\frac{\pi_1}{\pi_2}$ should be handled more economically as an additive term $\frac{\lambda_1}{\lambda_2}$ in the dB scale. In other words, there is no need to go to a three-dimensional map, if ever possible.

# Chapter 2

# In Search of a Simple Stress Measure for Direction-Finding Algorithms and Scenarios

We will first discuss the three main sources for the signal eigenvalue spread or causes for small signal eigenvalues. Next, we elaborate on eigenvector weighting expressions: in noise subspace methods, in parametric signal subspace fitting methods, and in nonparametric subspace adaptive beamforming. Finally we mention the drawbacks of oversimplifying the stress measuring yardstick: infinite condition number for all 100%-correlated two arrivals, equal condition numbers corresponding to different Cramer-Rao lower bounds (CRLBs), and CRLB not appealing to intuitive expectation.

## 2.1 The Three Main Sources for the Signal Eigenvalue Spread or Causes for Small Signal Eigenvalues

Schmidt's dissertation qualitatively pointed out the following three stressing factors to a direction-finding algorithm. For small- or medium-sized sensor arrays, the resolution is not sufficiently high so we can have unresolved arrivals. Furthermore 100% source correlation will cause rank deficiency of the noise-free data covariance matrix as well. The other stress factor to a direction-finding algorithm or scenario is the strength ratio between the two signals.

Hudson presented some eigenvalue results[23, pages 52-55] of the sensor data covariance matrix for two discrete sources. We can use his results here to infer that it is not unusual to find a 30-dB spread in the signal eigenvalues. Much more detailed treatment will be provided later in this report. The three multiplicative factors that contribute to the eigenvalue spread are: the signal-strength ratio, the angular proximity, and the high correlation between the two sources. A high signal-strength ratio, say 10 dB, almost directly translates into the eigenvalue ratio. The generalized cosine between the two steering vectors corresponding to the two arrivals is equivalent to the source correlation coefficient, as far as their effect on the eigenvalue spread is concerned. A value of 95% source correlation will contribute to 10 dB in the spread. A ULA with 10 elements at half-wavelength spacing and a 2-degree source spacing between a second source and a broadside one will yield 0.95 value of the generalized cosine between the two steering vectors, and therefore, another 10-dB spread.

The condition number, which in this case is the ratio of the two dominant eigenvalues of

the sensor data covariance matrix, is a good candidate to quantitatively describe the cumulative stress of scenarios. It is of interest to know how the eigenvalues behave when spatially resolved or unresolved (with respect to conventional beamforming) and/or temporally highly (including 100%) correlated arrivals are present, and as the ratio between the two signals' strength increases.

## 2.2  Eigenvector Weighting Expressions

### 2.2.1  In Noise Subspace Methods

Johnson and DeGraaf [25] proposed to modify the original noise subspace MUSIC algorithm by weighting the noise eigenvectors with the noise eigenvalues. The modification was derived in a somewhat ad hoc fashion. Some real data experience trading off Johnson and DeGraaf's weighting scheme to Schmidt's unweighted MUSIC was reported by Martin [32]. Martin's result, based on measured data, contradicted Johnson and DeGraaf's result, which was based on simulation and showed promise using noise eigenvector weighting.

As Martin did not give an explanation of why this was so from using a specific HFDF data set, we make the following conjecture. The noise eigenvalues appeared in the cost function through a setting of "reciprocal of reciprocals" of noise eigenvalues. When dealing with real data, as contrasted with simulated data under the ideal noise eigenvalues assumption, those small and furthermore nonequal eigenvalues may indeed play havoc.

On the other hand, this specific HFDF data set was severely marred by nonrandom calibration error. Furthermore, the input data to these two noise-subspace processors were the output from a de-chirping process because the signal waveform was Linear Frequency Modulated (LFM).

What could be cast as uncertain or inconclusive result from studying this specific HFDF data set is, however, remedied by the recent analytical result from Stoica and Nehorai [54] which shows that the minimum variance in the class of weighted noise subspace MUSIC estimators is achieved by the nonweighted MUSIC.

### 2.2.2  In Parametric Signal Subspace Fitting Methods

After Schmidt's MUSIC algorithm [49], Viberg and Ottersten's recent work [34,35,36,38,59,60,61] on weighted subspace fitting (WSF) direction-finding is among the most important works in array processing. In earlier multidimensional MUSIC algorithms, the residuals from fitting each signal eigenvectors by a linear combination of steering vectors with unknown DOA parameters are weighted equally in the separable nonlinear least squares formulation to jointly estimate these DOA parameters. Viberg and Ottersten found that a suitable weight for each eigenvector's fitting can be used to minimize the asymptotic estimation error of DOA parameters.

The weighting mentioned here is different from Johnson and DeGraaf's noise eigenvector weighting [25], because here signal eigenvector weighting is involved. The optimal WSF method for parametric array processing has (dominant) signal eigenvalues appearing in the weight expressions in the cost function. WSF is an optimal solution using a well-defined criterion. We note that signal eigenvalues are much more stable than the noise eigenvalues both numerically and statistically.

For high SNRs, the weights used in the Det-ML and the optimal WSF methods are very nearly equal. However, Cadzow's simulation results [8] using two coherent sources with high SNRs indicate that the Det-ML, which should be close to WSF in performance, is outperformed by the single signal eigenvector fitting method. During a private communication with us discussing this apparent discrepancy, Ottersten attributed this to the rank reduction principle by Scharf and

Tufts [47] and Scharf [48]. The rank reduction principle trades off model bias and model variance in the analysis and synthesis of signals to minimize the mean squared error. Even though the rank reduced approach provides biased estimates, the mean square error could be lower than the CRLB, which is asymptotically approached by Det-ML, an asymptotically unbiased estimator. This suggests that only dominant eigenvectors should be used.

The paper by Swindlehurst and Kailath [57] discusses phase and amplitude gain uncertainty and sensor position errors. The optimal weights are different from the ideal calibration case.

### 2.2.3 In Nonparametric Subspace Adaptive Nulling Beamforming

We need a brief description of the evolution of the well known Sampled Matrix Inverse (SMI) method in adaptive beamforming (ABF) to the subspace adaptive nulling method before we can address the equivalent version of weighted subspace variants.

For sonar applications, large arrays lead to problems in collecting enough snapshots for the SMI method within the constraint of stationarity. Snapshot sample requirements results are expressed in terms of the SNR degradation because of the inaccurate covariance matrix estimation. For SMI, the number of snapshots must exceed twice the number of sensors if the tolerable SNR degradation is to be no more than 3 dB. Perhaps SNR is better written as SBR (Signal-to-Background Ratio) or SINR (Signal-to-Interference-and-Noise ratio) as some people prefer. wIn this case, the increased background level is due to the interference left over because of the inadequate adaptive cancellation, whether in the presence or absence of signal. The net result is a decrease in SNR or SBR, which in turn leads to the system performance loss such as probability of detection from using a higher absolute detection threshold (with respect to the white noise, e.g.) to maintain a fixed probability of false alarm.

Subspace adaptive nulling depends upon the number of dominant eigenvectors. In their Principal Component Inverse (PCI) papers, Kirsteins and Tufts [28,29] concluded that the number of snapshots needs to exceed only twice the number of dominant eigenvectors if the tolerable SNR degradation is to be no more than 3 dB. The numerical experiment results reported by Hung et al. [24] agree with the results of Kirsteins and Tufts [29]. Even if PCI is used, a large sonar array may still have the number of sources within the array coverage exceeding the number of available snapshots. The natural question is: How small can the number of dominant eigenvectors be as compared to the number of sources?

Weights can be used in both MUSIC or its PCI beamforming equivalent and other recent subspace fitting methods, such as in Owsley's Enhanced Minimum Variance Beamforming (EMVDR) [39,1,2]. (The term "weights" used here refers to weighting the signal eigenvectors. It is not the "weight vector" used in the better known MVDR ABF algorithm.)

It is only a matter of time before someone starts to apply the optimal weights, used in the WSF for the parametric signal subspace approach, to subspace beamforming, e.g., PCI which can be considered as MUSIC's beamforming variant.

The recent papers by Farrier and Prosper [16], and Farrier [17] are very important. They managed to arrive at the performance of those jointly estimating DOA algorithms with the cost of those searching one-at-a-time spectrum type. They made a more efficient modification of Reilly, Wong, and Reilly's Bayesian approach in unknown colored noise [44]. While Reilly et al.'s approach can handle 100%-correlated arrivals and colored noise, Farrier and Prosper [16] are not far off as one of their methods managed to resolve two 98%-correlated arrivals in one scenario. By using this same method, they also improved the noise threshold by 13 dB in another case as compared to MUSIC. Among the three weighting schemes evaluated by Farrier and Prosper for

this method, the optimum weights by Viberg and Ottersten outperformed two less sophisticated ones by at least 3 dB in noise threshold.[1]

The word beamformer in Farrier and Prosper's paper is a misnomer as a beamformer produces a time series at each grid point and their method is a direction-finding one producing a null spectrum. Consequently, we note that their method can use the interpolation scheme by Schmidt [50]. There he shows that for simple scenarios with a second signal at least a Beamwidth (BW) away, the grid spacing can be as modest as 0.25 BW for an interpolation accuracy of 0.01 BW.

## 2.3 Drawbacks of Oversimplifying Stress Measuring Yardsticks

It turns out that condition number is not the only stressing factor for a direction-finding scenario and there are quite a few drawbacks in using it as stress-measuring yardstick. Most of these deficiencies are manifested under the following special cases either singly or jointly: the two arrivals are 100% correlated, of equal signal strength, and with temporal phase difference 0° or 180°. Regardless of these deficiencies, it is still a useful measure summarizing many stressing factors in many aspects.

### 2.3.1 Infinite Condition Number for All 100%-Correlated Arrival Pairs

When the two arrivals are 100% correlated so that the smaller eigenvalue is zero, the stress measured by condition number will go to infinity. Such a stress measure may be appropriate for the MUSIC algorithm, as the algorithm fails for this scenario, but not appropriate for the scenario. An algorithm like weighted subspace fitting can handle the scenario with no problem and furthermore asymptotically realize the (finite) stochastic CRLB. We know that some 100%-correlated scenarios are less stressful than others, and in these cases, the efficiency defined by the ratio of the asymptotic standard deviation of the parameter estimation to CRLB apparently is a better stress measure. As CRLB is available for all scenarios, one would naturally wish to use this as a universal yardstick. However, there is a practical problem: how do you represent all possible scenarios and present the results compactly? So far, the CRLB is presentable only for uniform line array, and even then not compactly.

### 2.3.2 Equal Condition Numbers Corresponding to Different CRLBs

Apparently, Schmidt [49, page 130] was the first one to use the noise-free signal eigenvalue ratio for stress measurement of a two-arrival direction-finding scenario. He recognized that the "stress" at the combination of $(\xi, \eta, \frac{\pi_1}{\pi_2}) = (0, 1, 1)$ is the least [2] of all possible ones. The two signal-eigenvalues equal the normalized unity power level at the sensor level. We believe that this led him to use an expression depending only on the eigenvalue ratio as a stress measurement. Evidently he was hampered by the lack of an effective visual aid to grasp the nontrivial functional dependence of these two eigenvalues on all possible combination of the product of the two unit-disks representing the temporal and spatial correlation between the two arrivals. This possibly led him to conclude,

---

[1] These less sophisticated weight choices include the one that Cadzow used in his recent papers [9,10] where he showed that his eigenvalue weighting produced results marginally better than the ones with unit weighting. It is somewhat confusing as the weight choice should not have any effect when there is only one dominant eigenvector involved such as in the case of two 100%-correlated arrivals used in these papers. If the dominant-eigenvector-only choice was abandoned, the rank-reduction advantage as pointed out by Ottersten will be missed too.

[2] We will discuss this in subsections 3.3.1, 3.3.3, and section 3.4.

without proof, a statement equivalent to one that the eigenvalue ratio can be one only at this $(\xi, \eta, \frac{\pi_1}{\pi_2}) = (0, 1, 1)$ combination.

We will see that when the two arrivals are of equal strength, i.e., $\frac{\pi_1}{\pi_2} = 1$, the two eigenvalues are equal over the left boundary of an isosceles-right-triangle-like region. Furthermore, the two equally dominant eigenvalues can go down to zero jointly so that the condition number stays unity throughout. That is, the condition numbers are the lowest possible there. However, both eigenvalues tend to zero as $\eta$ tends to zero, i.e., the baseline of the region. So, when the noise floor is brought in for example in the symmetrical multipath scenario, the direction-finding system can still be stressed significantly. Yet the final scenario would correspond to the case of two strong colocated coherent signals exactly equal in amplitude but totally out of phase. Even though the condition number remains as favorable as possible, i.e., of unity value, the scenario starts from the most benign one in stress and progressively gets more and more stressful and eventually gets to the point of being totally hopeless. The final DF problem amounts to determine the value of two equal numbers when it is only known that the difference is zero. Because the two signals cancel out each other exactly at the colocated emitters' location before the waves can propagate out, the sensor measures zero. Therefore, the magnitude of largest eigenvalue in unit of the smaller signal strength at the sensor level is a good complementary stress measurement.

### 2.3.3 CRLB Not Appealing to Intuitive Expectation

The effect of the phase difference between two signals on direction-finding is apparently not a well-understood subject. Most work about the effect of phase difference in direction-finding is for the low-angle radar tracking problem with two closely spaced, coherent, equipowered plane-wave arrivals impinging on a ULA. In examining candidates for the stress measure, we have considered eigenvalue ratio, CRLB, and asymptotic performance results of some subspace algorithms for such scenarios. However, we cannot intuitively reconcile the differences among these candidates.

If the center of the array is chosen as coordinate origin, the CRLB is symmetric, is maximum at $0°$ or $180°$, and is minimum at $90°$. The analytical derivation of this result is available in the report by Evans, Johnson, and Sun [15]. When we have two 100%-correlated signals, the scenario points in the isosceles region are located at the baseline where the smaller eigenvalue is zero. Furthermore, when the two signals are equipowered, the larger eigenvalue has [3] a linear variation varying from 0 to 2 to 4 when we move from the left-end to the middle and then the right-end point on the baseline. We try to use CRLB for the ULA case to serve as the stress measure. Note that the scenario with constructive interference has the same CRLB as the destructive one, i.e., it is symmetric about $90°$. The CRLB has its minimum occurring at this $90°$ phase difference point. For the extreme case of colocated signals, intuitively one would think that the constructive interference case is a more favorable scenario than the destructive one. This is because one can decide the DOAs from the constructively combined arrivals, even though one cannot infer whether more than one arrival contributes to the measurement. Neither can one reconstruct the original two-component amplitudes given only the final total. We believe this dilemma arises because of the derivation of CRLB from a rank-deficient composite steering vector matrix. If we allow the two equipowered arrivals to be colocated to start with in the basic data model, the constructive scenario may be differentiated from the destructive one for the CRLB.

For the equipowered case, the destructive interference scenario point is at the left apex of the isosceles region. Both eigenvalues are zero and they are global properties. The eigenvalue ratio $\frac{\lambda_1}{\lambda_2}$ at this point is of the 0/0 form. It is shown in subsections 3.4.1, and 3.4.4 that the contours

---

[3]We will discuss this in subsection 3.3.2.

of $\frac{\lambda_1}{\lambda_2} = 1$ pass through this point. This point corresponds to the total cancellation of signals at the sensor element level. The total cancellation happens not only at the center of the array but at every sensor. The two steering vectors coincide and the temporal waveforms negate each other completely. Consider two strong sources behaving this way. As the SNR is measured by turning off one source at a time, so the equal SNRs are considered as high and CRLB and asymptotic results apply.

The unified framework of subspace-fitting methods leading toward Ottersten and Viberg's WSF formulation for this two-source problem involves different weights. The optimum weights for the high SNR case involve the eigenvalue ratio. This ratio is indeterminate, and the asymptotic standard deviation can assume different paths leading toward the anomaly point.

Tran [58] derived and plotted the 2-d mesh surfaces of CRLB, Det-ML, WSF, and MUSIC against phase difference and SNR. For 90% temporal correlation, the CRLB surface is a lower bound for the other asymptotic surfaces and is symmetric with respect to the phase difference at 90°. Both WSF and Det-ML are fairly similar to each other because the SNR used is high. They lost the symmetry at 0.2-BW separation but retained a dip with 180° lower standard deviation at 180° than at 0°. MUSIC at 0.2-BW separation is monotonically increasing starting from 180° passing thru 90° and all the way to 0°. The mesh plots show that the symmetry conditions are present at 1-BW separation.

We need to reexamine the derivation of these asymptotic results and determine whether the rationale in dropping high-order terms remains valid when the parameters of these scenarios are taken into consideration. There is also the possibility that either the results are right but we need some interpretation or there is some flaw in our formulation. Numerical simulation seems to support those asymptotic results. Another question is whether high SNR is relevant under the condition of perfect cancellation.

### 2.3.4 Redeeming Value for Condition Number

Even with all these deficiencies, condition number is still a useful measure summarizing stressing factors in many cases. When the phase difference between two signals does not come into play in the eigenvalue expressions, such as when the two arrivals are temporally uncorrelated or spatially orthogonal, eigenvalue ratio seems to be a plausible stress measure. There, a large eigenvalue ratio will reflect the effects of either large normalized spatial- or temporal- correlation coefficient or high signal-strength ratio or any combination of them. For those problems with 100%-correlated and closely spaced arrivals, such as in the low-angle (microwave) radar tracking problem, mean square errors or CRLBs may be substituted for condition numbers as better stress measures, and the compact presentation for scenario parameter tradeoff need be used with cautions.

Schmidt's original MUSIC algorithm[4] uses the signal eigenvalues in a binary manner. That is, a hard decision between noise and signal is made. Viberg and Ottersten avoided making a binary decision by introducing a scale equivalent to the eigenvalue ratios. While much more information may be gained by using eigenvalue ratios, we are still constrained by the information that is conveyed. Other measures will provide us more information if there exists a manageable way to

---

[4]Here, we include the MultiDimensional (MD)-MUSIC described in his thesis for jointly estimating DOAs simultaneously which was motivated by considering the rank deficiency caused by 100%-correlated arrivals. There, he also pointed out the separable nonlinear least squares approach for MD-MUSIC. The name MD-MUSIC was coined in Roy's thesis [45] and later used in Viberg and Ottersten's works. While we have occasionally followed their usage, it is regretfully a misnomer. Without prior exposure of its definition, people tend to conjecture that some elevation measurement in addition to that of azimuthal one is involved. A better replacement is "jointly estimating MUSIC" contrasting the original one of searching one-at-a-time type.

present it, such as a compact map showing CRLB or asymptotic performance over all possible scenarios. We note that CRLB depends on the steering vectors not just through the function values but also the local behavior as functions of the direction-of-arrival (DOA) parameters. This is contrasted to the real triplet $(\xi, \eta, \frac{\pi_1}{\pi_2})$ required for the two noise-free eigenvalues and their ratio. Therefore, the next step of advancing from condition numbers to CRLBs is a very significant one.

## 2.4 Special Treatment Given for Equal Power Arrivals

The following are the reasons for giving equal-power arrivals special treatment:

1. It happens naturally in physical phenomena, e.g., for the case of low-angle radar tracking, see Haykin [22], Reilly and Haykin [41,42], Haber and Zoltowski [21], and Zoltowski and Lee [66]. The problem is the estimation of DOAs of a radar target located over a smooth reflecting sea when the main beam is pointed at or near the horizon.

2. Shown in subsection 3.4.2 is that for given $\frac{\pi_1}{\pi_2}$ power ratio, the $\lambda$ slices for constant phase-dependent variable $\xi$s are parabolas. The equal-power arrival case has some unique analytical properties stemming from the fact that it has the vertices of half of parabola sections fall within the range of parameters of interest. Consequently, there are infinite slopes involved here, unlike any other power ratios between the two arrivals. This is also the only case in which it is possible to have the two signals to cancel each other completely.

3. Most of the performance characterization using either Monte Carlo simulation or asymptotic analysis include equal-power arrivals as examples. For instance, see Cadzow et al. [6,7,8], Kaveh and Barabell [27], Ottersten, Viberg, et al. [34,36,37,59,60], Pillai and Kwon [40,30], Reilly and Haykin [41,42], Stoica and Nehorai [53,54,55], Haber and Zoltowski [21], and Zoltowski and Lee [66].

4. The concept of resolution threshold has been exploited by assuming two signals of equal power impinge on a ULA. The concept was started by Cox [13] for CBF and ABF. Kaveh and Barabell [27] used the same scenario for the MUSIC algorithm for incoherent arrivals. Pillai and Kwon [40] extended the treatment to MUSIC for coherent arrivals via spatial smoothing. Kwon and Pillai [30] further considered the resolution threshold issues for some special cases[5] of three equal-power arrivals. However, the concept of resolution threshold has outlived its usefulness with the arrival of the asymptotic analysis results such as those from Stoica and Nehorai [53,54,55], Ottersten, Viberg, et al. [34,36,59,60]. These asymptotic analysis results yield more insight, provide much more information enabling one to make parametric studies, and furthermore, are applicable to general sensor array configuration and general scenarios.

---

[5] For the case with the arrivals equally spaced in electric angle, the required threshold SNRs for the three-arrival case to resolve the three are about twice those for the two-arrival cases in dB scale. That is, the presence of a third source which is symmetrically located with respect to the center source increases the SNR required to resolve the original sources approximately by a factor of two in dBs.

For the general case, Stoica and Nehorai [55] proved that the asymptotic Det-CRLB increases monotonically when one more emitter is added while the directions of and the signals emitted by the original old sources remain the same. Furthermore, if the new source signal is uncorrelated with the older ones, then the Sto-CRLB increases monotonically. They stated that it is an open problem whether the assumptions of uncorrelated signals might be relaxed.

# Chapter 3

# Eigenvalues for Two Arrivals

## 3.1 Eigenvalue Equations

We follow the notations in Hudson's text[23, pages 37-38,52-55].

| | |
|---|---|
| $(.)^H$ | Hermitian transpose |
| $(.)^T$ | ordinary transpose |
| $(.)^*$ | complex conjugation |
| $Re(.)$ | real part of a complex number |
| $E(.)$ | expectation operator |
| $\tilde{\phantom{x}}$ | the quantity for the new coordinate |
| $j$ | $\sqrt{-1}$ |

| | |
|---|---|
| $N$ | number of sensors in array |
| $x$ | $N$-dimensional array data vector, $x = Sm + n$ |
| $R$ | data source covariance matrix, $E[xx^H]$ |
| $s_i$ | steering (column) vector for the $i$th source |
| $S$ | composite steering vector matrix, $S = \{s_i\}$ |
| $\phi$ | generalized cosine between $s_1$ and $s_2$ |
| $\rho$ | normalized correlation between first and second baseband signals |
| $\pi_1$ | signal power for the stronger source |
| $\pi_2$ | signal power for the weaker source |
| $\mu_i$ | $i$th eigenvalue of $R$ |
| $\lambda_1$ | larger eigenvalue of the noise-free part of $R$, normalized to $N\pi_2$ |
| $\lambda_2$ | smaller eigenvalue of the noise-free part of $R$, normalized to $N\pi_2$ |
| $\eta$ | $(1 - |\phi|^2)(1 - |\rho|^2)$, independent of the angle difference between the normalized temporal and spatial correlation coefficients $\rho$ and $\phi$, both constrained to unit disks. |
| $\xi$ | $Re(\rho\phi^*) = |\rho||\phi| \cos(\arg \rho - \arg \phi)$, dependent on angle difference |
| $a$ | the coefficient vector expressing an eigenvector as a linear combination of steering vectors |
| $z_i$ | position vector of the $i$th sensor element |
| $\kappa$ | unit direction cosine vector for the direction of arrival(DOA) of a signal |
| $c$ | speed of wave propagation |
| $\delta$ | the difference between two coordinate origins |
| $\omega_0$ | the center frequency for the narrowband signals |

| $(x_n, y_n)$ | $x_n = (n-1)d$, $y_n = 0$, the elements' location of Uniform Line Array (ULA) |
|---|---|
| $d$ | the uniform interelement spacing |
| $\alpha, \alpha_0$ | directions of two arrivals relative to broadside |
| $\theta$ | $\sin\alpha - \sin\alpha_0$, the reduced angular variable |
| $k$ | $2\pi/\texttt{wavelength}$, wave number |
| $kd\theta$ | the electrical phase angle from element to element along the ULA |
| $4\_dB\_down\_bw\_in\_\theta$ | 4 dB down beamwidth |
| $\theta_{frac\_bw}$ | separation between two arrivals in fractional beamwidth |

In complex notation, the $N$-dimensional sensor output vector $x$ is modeled by a linear combination of steering vectors $s_i$ of $M$ sources plus an $N$-dimensional noise vector $n$

$$x = Sm + n,$$

where $m_l$ is the complex amplitude of the $l$-th arrival. The usual assumptions of white noise and zero correlation between each signal and noise lead to

$$R = E[xx^H] = S\,E[mm^H]\,S^H + \sigma^2 I,$$

where $\sigma^2$ is the variance of the spacial white noise. The eigenvalue $\mu$ and eigenvector $u$ of $R$ is defined by

$$Ru = \mu u.$$

Hudson in [23] used the following developments restricted to the two-arrival case. The eigenvalues $\mu_i$ of $R$ are related to the eigenvalues $\lambda_i$ of $E[mm^H]\,S^H S$ through the relation

$$\mu_i = \lambda_i + \sigma^2.$$

The general case was mentioned in Kwon and Pillai[30]. These known results are rederived in the following. We start from

$$(S\,E[mm^H]\,S^H + \sigma^2 I)u = \mu u,$$

or

$$(S\,E[mm^H]\,S^H)u = (\mu - \sigma^2)u = \lambda u.$$

Therefore, the non-noise eigenvectors are linear combinations of the steering vectors of the DOAs,

$$u = S\left(\frac{E[mm^H]\,S^H u}{\lambda}\right) = Sa.$$

The non-noise eigenvalue can be derived from

$$S(\,E[mm^H]\,S^H S - \lambda I)a = 0.$$

With the usual assumptions that the steering vectors for different DOAs are linearly independent, we have

$$(\,E[mm^H]\,S^H S - \lambda I)a = 0.$$

Note here, the components of each eigenvector in this new non-Hermitian eigenproblem correspond to the coefficients expressing the corresponding eigenvector of the original Hermitian eigenproblem expressed as a linear combination of steering vectors.

In general, the product of two Hermitian matrices is not Hermitian. In fact, for the two-arrival case, we can see from the product matrix in Hudson's text[23, pages 52-55] that the diagonals are no longer real and the off-diagonal entries are not complex conjugate of each other. However, the eigenvalues of this product matrix should be real and non-negative as they are from the original Hermitian eigenproblem. Therefore, the sum of the diagonal entries are still real because of the invariant property of the trace after orthogonal transformations. By using a similar but simpler factoring argument, Speiser and Arnold[51] in fact derived useful bounds for singular values of direction-finding problems for the general case. As the emphasis of this report is on two arrivals, we will evaluate his bounds in section 3.6 in this context.

We return to the consideration of two-arrival noise-free dominant eigenvalues. These two eigenvalues for the eigenproblem

$$
\begin{bmatrix} \pi_1 & \sqrt{\pi_1\pi_2}\rho \\ \sqrt{\pi_1\pi_2}\rho^H & \pi_2 \end{bmatrix} \begin{bmatrix} N & N\phi \\ N\phi^H & N \end{bmatrix} a = \lambda a
$$

are

$$
\begin{pmatrix} \lambda_1 \\ \lambda_2 \end{pmatrix} = \frac{1}{2} N \left[ \pi_1 + \pi_2 + (\pi_1\pi_2)^{\frac{1}{2}}2\xi \right] \times \left[ 1 \pm \sqrt{1 - \frac{4\pi_1\pi_2\eta}{\left[ \pi_1 + \pi_2 + (\pi_1\pi_2)^{\frac{1}{2}}2\xi \right]^2}} \right]
$$

where

$$
\eta = (1 - |\phi|^2)(1 - |\rho|^2),
$$

$$
\xi = \mathrm{Re}(\rho\phi^*) = |\rho||\phi|\cos(\arg\rho - \arg\phi).
$$

Let $\pi_1 \geq \pi_2$. The eigenvalue problem can be rewritten as

$$
\begin{bmatrix} \frac{\pi_1}{\pi_2} & \sqrt{\frac{\pi_1}{\pi_2}}\rho \\ \sqrt{\frac{\pi_1}{\pi_2}}\rho^H & 1 \end{bmatrix} \begin{bmatrix} 1 & \phi \\ \phi^H & 1 \end{bmatrix} a = \left( \frac{\lambda}{N\pi_2} \right) a.
$$

Henceforth, the eigenvalues will be redefined as their normalized values with respect to $N\pi_2$, so that

$$
\begin{pmatrix} \lambda_1 \\ \lambda_2 \end{pmatrix} = \frac{1}{2} \left[ \frac{\pi_1}{\pi_2} + 1 + (\frac{\pi_1}{\pi_2})^{\frac{1}{2}}2\xi \right] \times \left[ 1 \pm \sqrt{1 - \frac{4(\frac{\pi_1}{\pi_2})\eta}{\left[ \frac{\pi_1}{\pi_2} + 1 + (\frac{\pi_1}{\pi_2})^{\frac{1}{2}}2\xi \right]^2}} \right].
$$

Before finishing the introduction of symbols and definitions, we point out the importance of the sensor coordinate origin. When two arrivals are 100% correlated, the phase difference between the two source signals plays an important role. The specification of this variable depends on the choice of the coordinate origin. Frequently, performance such as CRLB is plotted against this variable. If two different origins are used, the same results can be seen differently but are equivalent with a horizontal shift and possibly with the help of $2\pi$-modulo wrap-around. Naturally, the covariance matrix and their eigenvalues are not dependent on the choice of the origin, but the expressions for the phase angles of both the steering vectors and complex source amplitudes of the signals are. The following make these discussions clearer.

Denote the difference between the two coordinate origins by $\delta$, i.e., the sensor position descriptions in these two coordinate systems are related by $z_i = \tilde{z}_i + \delta$ for all sensor elements. The signal part of the sensor data vector at the $i$th sensor is

$$
(Sm)_i = \sum_{k=1}^{2} S_{ik}m_k = \sum_{k=1}^{2} e^{j\omega_0 \kappa_k^T z_i / c} m_k
$$

$$= \sum_{k=1}^{2} \left( e^{j\omega_0 \kappa_k^T \tilde{z}_i/c} \right) \left( e^{j\omega_0 \kappa_k^T \delta/c} m_k \right) = \sum_{k=1}^{2} \tilde{S}_{ik} \tilde{m}_k$$

$$= (\tilde{S}\tilde{m})_i.$$

Define $D = diag(e^{j\omega_0 \kappa_k^T \delta_i/c} m_k)$. Then we have $\tilde{S} = SD^{-1}$, and $\tilde{m} = Dm$. Note

$$( E[\tilde{m}\tilde{m}^H] )_{il} = (D\, E[mm^H]\, D^H)_{il} = e^{j\omega_0(\kappa_i - \kappa_l)^T \delta/c} ( E[mm^H] )_{il},$$

and

$$(\tilde{S}^H \tilde{S})_{il} = (D^{-H} S^H S D^{-1})_{il} = e^{j\omega_0(\kappa_i - \kappa_l)^T \delta/c} (S^H S)_{il}.$$

The angular difference between the temporal and spacial correlation coeffients is therefore independent of the coordinate choices, as

$$\arg( E[\tilde{m}\tilde{m}^H] )_{il} - \arg(\tilde{S}^H \tilde{S})_{il} = \arg( E[mm^H] )_{il} - \arg(S^H S)_{il}.$$

The assignment of an array coordinate origin synchronizes the angles of zero references of the two disks.

In the special case of plane waves, an array is called pairwise symmetric or inverse symmetric [13] if for each sensor located away from the origin at position coordinates $(x_i, y_i, z_i)$ there is also a sensor located at $(-x_i, -y_i, -z_i)$. The inner product of two steering vectors for plane waves impinging onto a pairwise symmetric array is real. For such case, the usual two-dimensional unit-disk associated with spatial-correlation $\phi$ degenerates into a one-dimensional one. Then the angle difference between the temporal- and spatial-correlation coeffients is reduced to the temporal phase difference between the two arrivals measured at the origin of the symmetric array.

Even though such relation is derived from plane waves impinging onto pairwise symmetric arrays for convenience, we call $\eta$ the phase-independent variable and $\xi$ the phase-dependent variable.

## 3.2  An Isosceles-Right-Triangle-Like Region

One can see easily that the normalized $\lambda$s and their ratio $\lambda_1/\lambda_2$ are functions of the three parameters $\eta$, $\xi$, and $\pi_1/\pi_2$. It is clear that $0 \leq \eta \leq 1$. But $\eta$ and $\xi$ are not entirely independent of each other. In the following, we will show that given $\eta$, $\xi$ is bounded depending upon the $\eta$ value which in turn depends only on $|\rho|$ and $|\phi|$.

As $\xi$ is the triple product of $|\rho|$, $|\phi|$, and $\cos(\arg \rho - \arg \phi)$, it suffices to bound

$$|\xi|_{\text{max, given } \eta} = |\rho||\phi|$$

subject to the equality constraint

$$(1 - |\phi|^2)(1 - |\rho|^2) = \eta.$$

Using

$$
\begin{aligned}
(|\rho||\phi|)^2 &= |\rho|^2(1 - \frac{\eta}{1 - |\rho|^2}) = |\rho|^2 - \eta(-1 + \frac{1}{1 - |\rho|^2}) \\
&= -(1 - |\rho|^2) + (1 + \eta) - \frac{\eta}{1 - |\rho|^2},
\end{aligned}
$$

and setting to zero the derivative of the above expression with respect to $(1 - |\rho|^2)$ to maximize $\xi$, we have

$$-1 + \frac{\eta}{(1 - |\rho|^2_{\text{max } \xi, \text{ given } \eta})^2} = 0,$$

then we have

$$|\rho|^2_{\text{max } \xi, \text{ given } \eta} = 1 - \sqrt{\eta}.$$

From the definition of $\eta$, a similar relation holds for $\phi$, i.e.,

$$|\phi|^2_{\text{max } \xi, \text{ given } \eta} = 1 - \sqrt{\eta}.$$

Therefore, we have

$$(|\rho||\phi|)_{\text{max } \xi, \text{ given } \eta} = 1 - \sqrt{\eta}.$$

For given $\pi_1/\pi_2$, the domain in the $\eta$ and $\xi$ plane over which $\lambda$s and their ratio $\lambda_1/\lambda_2$ are defined is the isosceles-right-triangle-like region bounded by one line and two parabolas:

$$\eta = 0, \text{ and } \eta = (\xi \pm 1)^2.$$

We note the zero slope of each parabola where it meets the straight line and the 90° angle that the two parabolas intersect each other.

We will see later that among the three parameters $(\xi, \eta, \pi_1/\pi_2)$ appearing in the eigenvalues' expressions, $\eta$ is the most important one. In the following, we use figure 3.1 to provide some characterization of the many-to-one mapping from the Cartesian product of the two unit-disks onto the isosceles-like region with respect to $\eta$. We note that for given $\eta$, $\max(|\rho|, |\phi|) = \sqrt{1 - \sqrt{\eta}}$. Therefore, the apex point $(0, 1)$ corresponding to $\eta = 1$ can only come from the two centers of the unit-disks, i.e., $\rho = \phi = 0$. As $\eta$ decreases from 1 to 0, i.e., we move from the apex towards the baseline, we shade the part of the Cartesian product of the two unit-disks which is mapped into the correspondingly shaded area of the isosceles-like region. Therefore, as the shaded area of
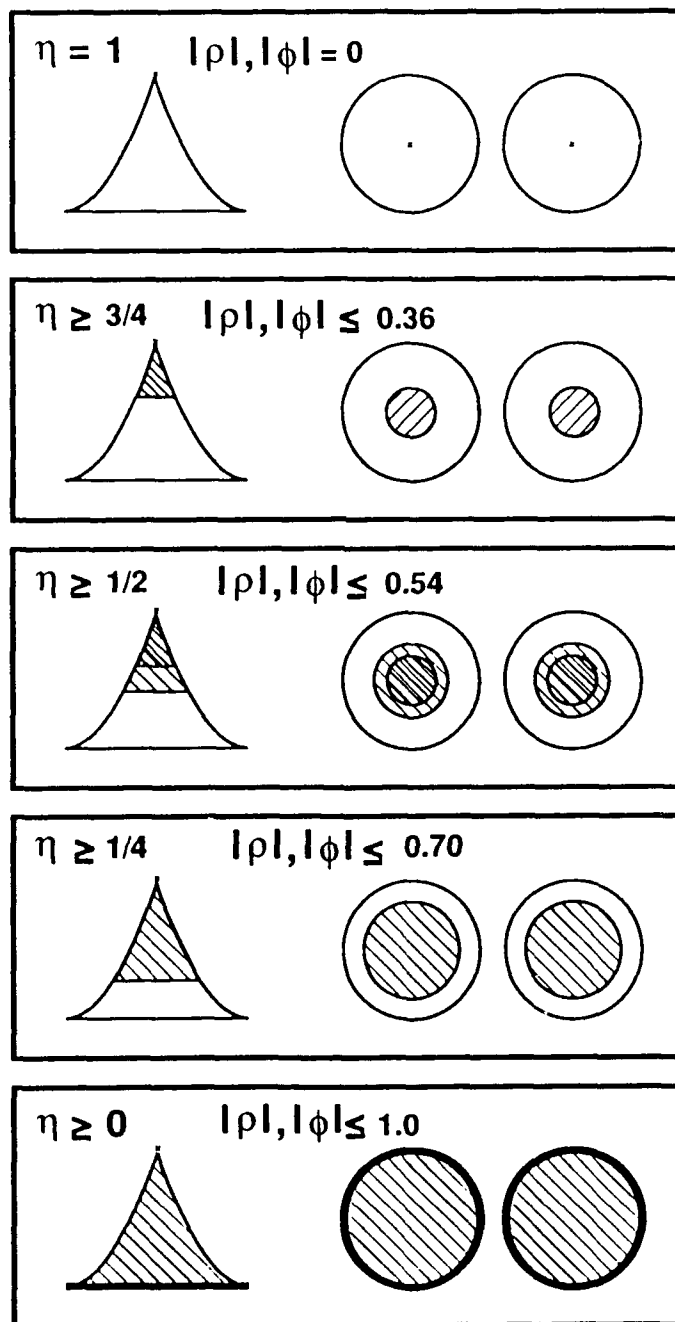
Figure 3.1: The many-to-one mapping.

561-2.76

24

the isosceles-like region expands from the apex towards the baseline, the shaded areas of the two unit-disks expand from the centers toward the unit circumferences.

When we move one-fourth the way toward the baseline, i.e., $\eta \geq 0.75$, we find $\max(|\rho|, |\phi|) = \sqrt{1 - \sqrt{0.75}} \approx 0.36$. Let us shade the corresponding range and domain of this many-to-one mapping using 45° hatching lines for this $\eta \geq 0.75$ region. Similarly, when we have moved halfway toward the baseline in the isosceles-like region $\eta \geq 0.50$, we find $\max(|\rho|, |\phi|) = \sqrt{1 - \sqrt{0.5}} \approx \sqrt{0.3} \approx 0.54$. Let us overlay onto the earlier picture by shading the corresponding range and domain using offset 45° hatching lines for this $\eta \geq 0.50$ value. We note that the previously 45° hatched region are double-hatched now. For any point in the incremental area of the isosceles-like region corresponding to the singly 45° hatched but not double-hatched area, i.e., $0.75 \geq \eta \geq 0.50$, at least one of the originating $\rho$ or $\phi$ must be located in the correspondingly shaded incremental annulus, i.e., $0.36 \leq |\rho|$ or $|\phi| \leq 0.54$.

We also note that $\eta = (1 - |\phi|^2)(1 - |\rho|^2)$ is the height of the unshaded trapezoidal-like region. We can associate $\pi \eta$ as the product of the areas of the two unshaded annulus regions, $\pi(1 - |\phi|^2)$ and $\pi(1 - |\rho|^2)$. As this height reduces from 1 to 0, i.e., the unshaded trapezoid decreases from the original whole isosceles all the way to the zero thickness baseline, the corresponding white annulus shrinks from the original unit-disk to a zero thickness circle.

When the scenario is stressful, $\eta$ is small, the corresponding annuli with unit outer radius are thin. The area of the temporal correlation $\rho$ annulus can be approximated by

$$\pi(1 - |\rho|^2) = \pi(1 + |\rho|)(1 - |\rho|) \approx 2\pi(1 - |\rho|).$$

Suppose the temporal correlation coefficient has a magnitude of 99% and up, then the thickness of the $\rho$ annulus is 0.01, the area of the annulus can be approximated by $2\pi(0.01)$ by letting the mean circumference of the annuls assuming the outer circumference of the unit-disk, $2\pi$. The approximation is 99.5% accurate. If the spatial correlation coefficient has a magnitude of 90% and up, then the thickness of the $\phi$ annulus is 0.1, the area of the annulus can be approximated by $2\pi(0.1)$. The approximation accuracy is 95%. We see that a combination of the high temporal and spatial correlations yield an $\eta$ of approximately $(-20 + 3) + (-10 + 3) = -24$ dB.

For given $\eta$, we are interested in the maxima of $|\rho|$, $|\phi|$, and $|\xi|$. Given $\eta$, $\eta = (1 - |\phi|^2)(1 - |\rho|^2) \leq \min(1 - |\rho|^2, 1 - |\phi|^2)$. That is, $\max(|\rho|^2, |\phi|^2) \leq 1 - \eta$, or $\max(|\rho|, |\phi|) \leq \sqrt{1 - \eta}$. Therefore, $\max(|\rho|) = \sqrt{1 - \eta}$ occurs when $1 - |\phi|^2 = 1$ or $\phi = 0$. Similarly, $\max(|\phi|) = \sqrt{1 - \eta}$ occurs when $\rho = 0$. Both scenario points are at the vertical axis, $\xi = 0$.

Consider $\eta = \frac{1}{4}$, i.e., three-fourth of the way toward the baseline. $|\xi|_{\min}$, given $\eta = 0$ occurs at the vertical axis, with $|\rho|$ or $|\phi| = \sqrt{1 - \eta} = \frac{\sqrt{3}}{2} \approx 0.866$. We already know that, from the derivation of the isosceles region, $|\xi|_{\max}$, given $\eta$ occurs at $|\rho| = |\phi| = \sqrt{1 - \sqrt{\eta}} = \frac{\sqrt{2}}{2} \approx 0.707$, i.e., the two parabolic boundaries. These are summarized in table 3.1.

Figure 3.1 need to be interpreted with cautions. The domain of the many-to-one mapping, a subset of the 4-d Cartesian product of two disks, for a range having the shape of a shaded 2-d subtriangular region cannot be explained briefly. The labels and sizes of the shaded disks in figure 3.1 need be interpreted according to table 3.2.

Next, we use figure 3.2 to characterize some special positions in the isosceles region. Hudson's textbook presented 4 out of the 17 characterizations shown there. These four cases are denoted by the asterisks.
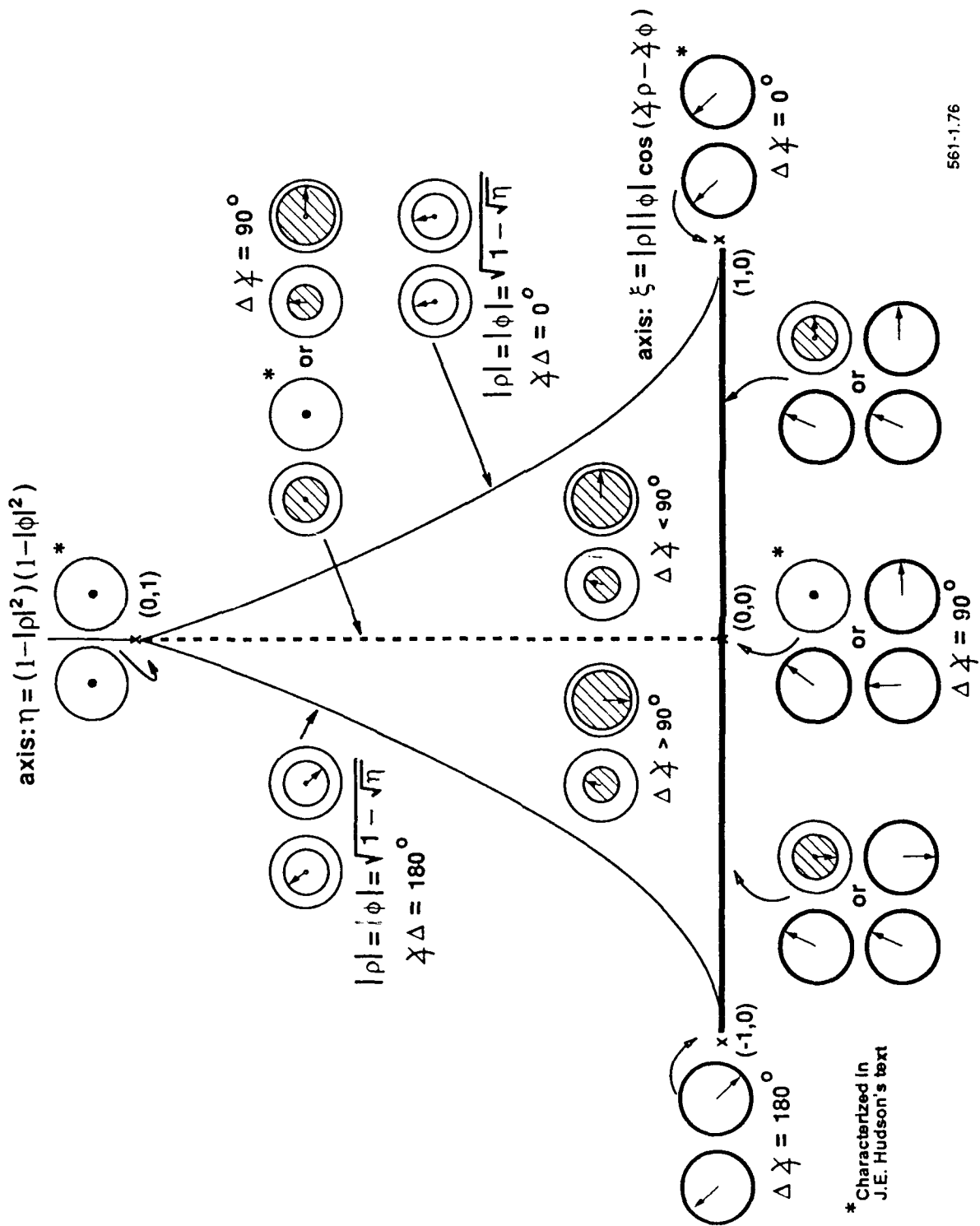
Figure 3.2: Mapping from Cartesian product of two unit-disks to a planar region.

561-1.76

26

Table 3.1: Expressions of $|\xi|$, $|\rho|$, and $|\phi|$, given $\eta = \frac{1}{4}$.

| $|\xi|$ | $|\rho|$ | $|\phi|$ |
|---|---|---|
| min $= 0$ (vertical axis) | 0 (center of disk) | max$= \sqrt{1-\eta} = \frac{\sqrt{3}}{2} \approx 0.866$ |
| | max $= \sqrt{1-\eta} = \frac{\sqrt{3}}{2} \approx 0.866$ | 0 (center of disk) |
| max $= 1 - \sqrt{\eta} = \frac{1}{2} = 0.500$ (parabolic boundary) | $\sqrt{1 - \sqrt{\eta}} = \frac{\sqrt{2}}{2} \approx 0.707$ | $\sqrt{1 - \sqrt{\eta}} = \frac{\sqrt{2}}{2} \approx 0.707$ |

Table 3.2: Interpretations of the $\phi$ unit-disk for two uncorrelated plane wave arrivals impinging onto a uniform linear array.

| $\eta$ | $\max|\phi|^2 = 1 - \eta$ | $\max|\phi| = \sqrt{1-\eta}$ | Separation Between Arrivals |
|---|---|---|---|
| 1 | 0 | 0 | nulls, i.e., 1,2,$\cdots$,-BW |
| $\frac{3}{4}$ | $\frac{1}{4}$ | $\frac{1}{2} = 0.500$ | $> \frac{1}{2}$-BW |
| $\frac{1}{2}$ | $\frac{1}{2}$ | $\frac{\sqrt{2}}{2} \approx 0.707$ | $\frac{1}{2}$-BW |
| $\frac{1}{4}$ | $\frac{3}{4}$ | $\frac{\sqrt{3}}{2} \approx 0.866$ | $< \frac{1}{2}$-BW |
| 0 | 1 | 1 | coincident mainlobes or grating lobes |

## 3.3 Special Cases at the Apex, the Baseline, and the Vertical Axis

We now characterize some special cases of interest. They are

1. at the apex, i.e., $(\xi, \eta) = (0, 1)$,

2. at the baseline, i.e., $\eta = 0$,

3. at the vertical axis, i.e., $\xi = 0$.

### 3.3.1 Special Case at the Apex, i.e., $(\xi, \eta) = (0, 1)$

Here we have the two arrivals 0% correlated and the two steering vectors orthogonal to each other simultaneously. Note

$$\lambda_1 = \frac{\pi_1}{\pi_2}, \text{ and } \lambda_2 = 1 \text{ or } 10 \log_{10}(\lambda_2) = 0 \text{ dB}.$$

This is the most benign scenario for a direction-finding system where the two arrivals behave essentially independently of each other.

### 3.3.2 Special Case at the Baseline, i.e., $\eta = 0$

This is the case where the source amplitudes of the two arrivals are 100% correlated or/and the two corresponding signal vectors are complex scalar multiples of each other or both.

We have the following results:

$$\lambda_2 = 0, \text{ or } 10 \log_{10}(\lambda_2) = -\infty \text{ dB},$$

$$\lambda_1 = \frac{\pi_1}{\pi_2} + 1 + \sqrt{\frac{\pi_1}{\pi_2}} \, 2\xi.$$

We note that when $\xi$ changes from -1 to 0 to +1, $\lambda_1$ varies linearly in $\xi$ with the slope equal to $2\sqrt{\frac{\pi_1}{\pi_2}}$ from

$$(\sqrt{\frac{\pi_1}{\pi_2}} - 1)^2 \text{ to } (\frac{\pi_1}{\pi_2} + 1) \text{ to } (\sqrt{\frac{\pi_1}{\pi_2}} + 1)^2.$$

Therefore, the two vertices corresponding to

$$(\xi, \eta) = (-1, 0) \text{ and } (1, 0)$$

are associated with totally destructive and constructive interferences respectively. Here the two arrivals are colocated with respect to the steering vectors, e.g., along the same direction of arrival, and the source amplitudes are exactly opposite in sign or equal to each other. At the mid-point, $(\xi, \eta) = (0, 0)$, we have

$$\lambda_1 = \frac{\pi_1}{\pi_2} + 1.$$

When the two 100% correlated arrivals are "quadraturely related," this is the place where it occurs. (In direction-finding, any two arrivals are called coherent as long as their source amplitudes are 100% correlated, even if their phase difference is 90°.)

### 3.3.3 Special Case at the Vertical Axis, i.e., $\zeta = 0$

We have any of the following three possibilities:

1. $\rho = 0$, i.e., the source amplitudes of the two arrivals are 0% correlated,

2. $\phi = 0$, i.e., the two steering vectors are orthogonal to each other, e.g., a delay and sum beam for the case of ULA in the direction of the first arrival will produce a null in the direction of the second,

3. $\cos(\arg \rho - \arg \phi) = 0$, i.e., the 2 phasors on the two unit-disks are perpendicular to each other.

We have

$$\lambda = \frac{1}{2}(\frac{\pi_1}{\pi_2} + 1)\left[1 \pm \sqrt{1 - \frac{4(\frac{\pi_1}{\pi_2})\eta}{(\frac{\pi_1}{\pi_2} + 1)^2}}\right].$$

This can be rewritten in a more revealing form of a parabola in $\lambda$ and $\eta$

$$\left[\lambda - \frac{1}{2}(\frac{\pi_1}{\pi_2} + 1)\right]^2 = \left[\frac{1}{2}(\frac{\pi_1}{\pi_2} + 1)\right]^2 - \frac{\pi_1}{\pi_2}\eta = -\frac{\pi_1}{\pi_2}\left[\eta - \frac{(\frac{\pi_1}{\pi_2} + 1)^2}{4\frac{\pi_1}{\pi_2}}\right].$$

This equation describes that the two curves of $\lambda_1$ and $\lambda_2$ as functions of $\eta$ for $\xi = 0$ pertain to two parts of the same truncated parabola in $\lambda$ and $\eta$. Because the arithmetic mean of $\frac{\pi_1}{\pi_2}$ and 1 is never smaller than the geometric mean, the vertex of this single parabola lies outside the domain of interest except when $\frac{\pi_1}{\pi_2} = 1$. In the exceptional case, there is no truncation of the parabola in $\lambda$ and $\eta$ and the two curves meet at unit height. As $\eta$ decreases from 1 to 0, the concave downward curve of $\lambda_1$ increases from $\frac{\pi_1}{\pi_2}$ to $\frac{\pi_1}{\pi_2} + 1$, whereas the concave upward curve of $\lambda_2$ decreases from 1 to 0.

Taking partial derivatives of the last equation of the two curves with respect to $\eta$ and rearranging, we have for $i = 1, 2$

$$\frac{\partial}{\partial \eta}\lambda_i(0, \eta) = \frac{-\frac{\pi_1}{\pi_2}}{2\left[\lambda_i - \frac{1}{2}(\frac{\pi_1}{\pi_2} + 1)\right]}.$$

At the baseline where $\eta = 0$, $\lambda_1 = \frac{\pi_1}{\pi_2} + 1$, and $\lambda_2 = 0$, we have

$$\frac{\partial}{\partial \eta}\lambda_1(0, 0) = -\frac{\partial}{\partial \eta}\lambda_2(0, 0) = -\frac{\frac{\pi_1}{\pi_2}}{(\frac{\pi_1}{\pi_2} + 1)} = -1 + \frac{1}{(\frac{\pi_1}{\pi_2} + 1)}.$$

At the apex where $\eta = 1$, $\lambda_1 = \frac{\pi_1}{\pi_2}$, and $\lambda_2 = 1$, we have

$$\frac{\partial}{\partial \eta}\lambda_1(0, 1) = -\frac{\partial}{\partial \eta}\lambda_2(0, 1) = -\frac{\frac{\pi_1}{\pi_2}}{(\frac{\pi_1}{\pi_2} - 1)} = -1 - \frac{1}{(\frac{\pi_1}{\pi_2} + 1)}.$$

For large $\frac{\pi_1}{\pi_2}$ and as $\eta$ ranges from 1 to 0, the theoretical decrease in magnitude of the slope of the slightly concave downward curve of $\lambda_1$ is hardly noticeable. For all practical purposes, the $\lambda_2$ curve is a straight line with slope 1 and values between 1 and 0, and that of $\lambda_1$ is a straight line with slope -1 between 1 and 2. When scaling is used, the $\lambda_1$ and $\lambda_2$ curves plotted together will be fairly flat for large $\frac{\pi_1}{\pi_2}$ values.

When $\frac{\pi_1}{\pi_2} = 1$ and as $\eta$ ranges from 1 to 0, the slope of the concave downward curve of $\lambda_1$ increases from $-\infty$ to $-1/2$, whereas the slope of the concave upward curve of $\lambda_2$ decreases from $+\infty$ to $1/2$. The $\pm\infty$ values of the slopes of the $\lambda_2$ and $\lambda_1$ curves with respect to $\eta$ at $\eta = 1$ indicate the rapid rate of the increase in "stress" to the direction-finder for the case of $\frac{\pi_1}{\pi_2} = 1$. However, we also note that the "stress" at this combination of $(\xi, \eta, \frac{\pi_1}{\pi_2}) = (0, 1, 1)$ is the least of all possible ones. Unless special care is given, commonly used plots will not reflect the infinite-slope case well.

As we try to use the eigenvalue ratio $\frac{\lambda_1}{\lambda_2}$ as a stress indicator, the rest of this subsection concerns the ratio $\frac{\lambda_1}{\lambda_2}$ as a function of $\frac{\pi_1}{\pi_2}$ and $\eta$. We separately discuss the two cases of $\frac{\pi_1}{\pi_2} \gg 1$ and $\frac{\pi_1}{\pi_2} \approx 1$.

When $\frac{\pi_1}{\pi_2} \gg 1$, we first approximate the radical expression as

$$\sqrt{1 - \frac{4(\frac{\pi_1}{\pi_2})\eta}{(\frac{\pi_1}{\pi_2} + 1)^2}} \approx \sqrt{1 - \frac{4\eta}{\frac{\pi_1}{\pi_2}}} \approx 1 - \frac{2\eta}{\frac{\pi_1}{\pi_2}}.$$

Then the ratio $\frac{\lambda_1}{\lambda_2}$ is given approximately by

$$\frac{\lambda_1}{\lambda_2} = \frac{1 + \sqrt{\phantom{x}}}{1 - \sqrt{\phantom{x}}} \approx \frac{2 - \frac{2\eta}{\frac{\pi_1}{\pi_2}}}{\frac{2\eta}{\frac{\pi_1}{\pi_2}}} = \frac{\frac{\pi_1}{\pi_2}}{\eta} - 1 \approx \frac{\pi_1}{\pi_2}/\eta.$$

That means the stress from $\eta$ and $\frac{\pi_1}{\pi_2}$ is multiplicative (divisive) in the direct scale. In dB scale, this is additive, i.e.,

$$\frac{\lambda_1}{\lambda_2}(\text{in dB}) \approx (\frac{\pi_1}{\pi_2})(\text{in dB}) - \eta(\text{in dB}).$$

When $\frac{\pi_1}{\pi_2} \approx 1$, we have

$$\frac{\lambda_1}{\lambda_2} = \frac{1 + \sqrt{1 - \eta}}{1 - \sqrt{1 - \eta}} = \frac{(1 + \sqrt{1 - \eta})^2}{1 - (1 - \eta)} = \frac{2 - \eta + 2\sqrt{1 - \eta}}{\eta} \approx \frac{4}{\eta}.$$

We used $\eta \ll 1$ in the last step. Translated into dB scale, this is

$$\frac{\lambda_1}{\lambda_2}(\text{in dB}) \approx -\eta(\text{in dB}) + 6.$$

This extra 6 dB accounts for the presence of the infinite slope of $\lambda$ with respect to $\eta$ at the apex for the equal-power arrival case.

These analytical results will be verified in figure 5.29 and discussed in subsection 5.4.1.

## 3.4  Special Case: Equal Strength Arrivals, i.e., $\pi_1/\pi_2 = 1$

The normalized eigenvalues assume the following expressions

$$\lambda_i = (1+\xi)\left[1 \pm \sqrt{1 - \frac{\eta}{(1+\xi)^2}}\right] = (1+\xi) \pm \sqrt{(1+\xi)^2 - \eta}.$$

We note that

$$\lambda_1(0,1) = \lambda_2(0,1) = 1, \text{ and } \lambda_1(-1,0) = \lambda_2(\xi,0) = 0.$$

The first equation states that the two surfaces $\lambda_1(\xi,\eta)$ and $\lambda_2(\xi,\eta)$ coincide at the apex of the isosceles-right-triangle-like region, as they should. The second equation states that both eigenvalues coincide again and vanish at the left vertex of the baseline corresponding to destructive interference.

The two eigenvalues are equal (not necessarily zero) only if what is inside the radical vanishes. For the case $\pi_1/\pi_2 = 1$, the resulting equation coincides with that of the left parabola in the $\xi$ and $\eta$ plane bounding the region over which the $\lambda$s are defined. The common value they share is

$$\lambda_i(\xi,(1+\xi)^2) = (1+\xi) = \sqrt{\eta}.$$

However, we caution that unless special effort is made in plotting results, the two displayed surfaces or curves may not always meet at the supposed places. This is because the boundary curves defining parabolas in the $\xi$ and $\eta$ plane, in general, do not pass through the grid points used in the $\xi$ and $\eta$ plane.

At the baseline $\eta = 0$, we have $\lambda_2 = 2(1+\xi)$. This means that when $\xi$ changes from $-1$ to $0$ to $+1$, $\lambda_1$ varies linearly in $\xi$ with unit slope from 0 to 2 to 4. At the vertical axis $\xi = 0$, we have the following parabola forms

$$\lambda_i = 1 \pm \sqrt{1 - \eta}.$$

### 3.4.1  Straight Line Contours for Constant Eigenvalue $\lambda$s

We now investigate the contour plots of these two surfaces by using the following rearranged equations

$$\lambda_i - (1+\xi) = \pm\sqrt{(1+\xi)^2 - \eta},$$

or

$$\eta + \lambda_i^2 = 2\lambda_i(1+\xi).$$

These contours are straight lines in the $\xi$ and $\eta$ plane with positive slopes $2\lambda_i$ and intercept the vertical line passing through the left vertex $(-1,0)$ of $-\lambda_i^2$. The mesh and contour plots of $\lambda_1$ and $\lambda_2$ are shown in figures 3.3 and 3.4 respectively.

As the contour values of $\lambda_1$ increase from 0 to 2 to 4, the slope increases linearly from 0 to 4 to 8, and the intercept decreases quadratically from 0 to $-4$ to $-16$. These contours intersect the baseline in equal intervals as we noted early.

As the contour value of $\lambda_2$ increases from 0 to 1, the slope increases linearly from 0 to 2, and the intercept decreases quadratically from 0 to $-1$. Note the 0 contour coincides with the baseline.

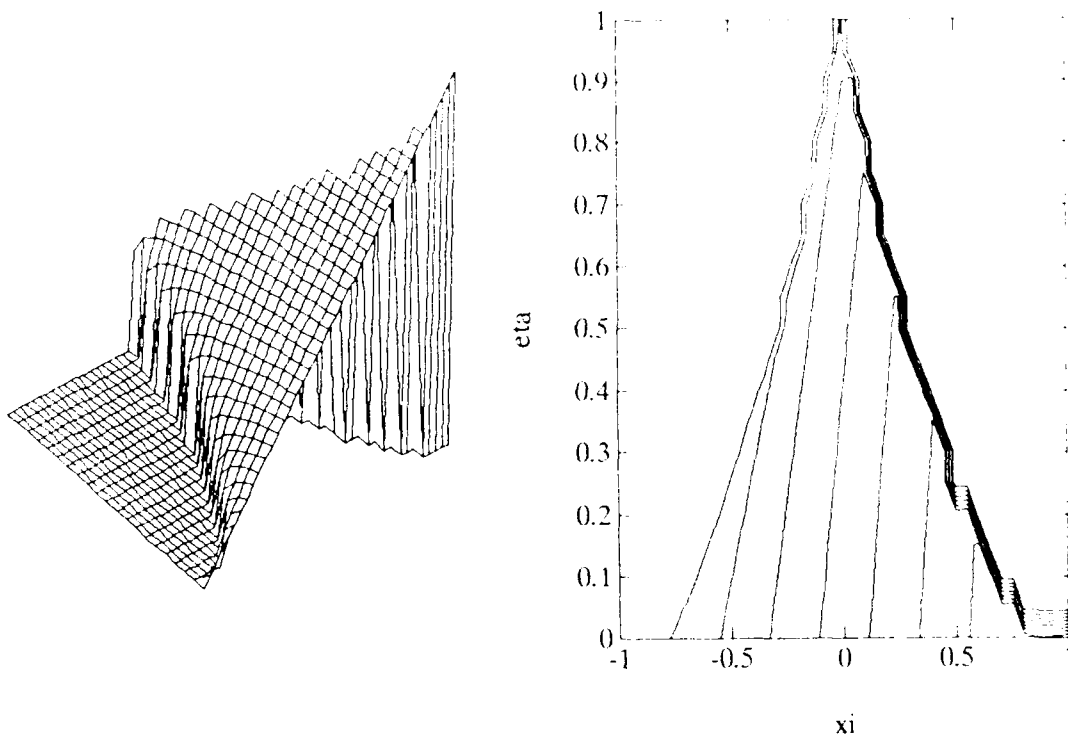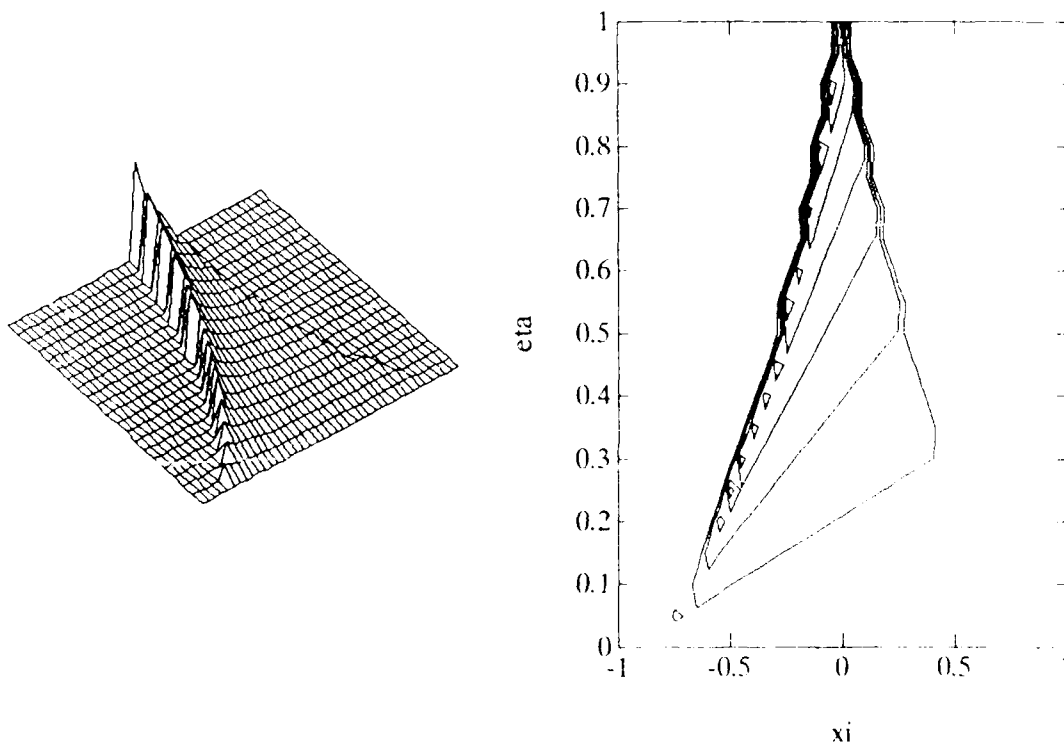Figure 3.3: Straight line contours of $\lambda_1$ for $\frac{r_1}{r_2} = 0$ dB.



Figure 3.4: Straight line contours of $\lambda_2$ for $\frac{r_1}{r_2} = 0$ dB.

### 3.4.2 Parabolic Slices for Constant Phase-Dependent Variable $\xi$s

For constant $\xi$ slices, the characteristic equation can be rearranged to that of a parabola in $\lambda$ and $\eta$ as

$$[\lambda - (1 + \xi)]^2 = -\left[\eta - (1 + \xi)^2\right].$$

Figures 3.5 plots for $\lambda_1$ And $\lambda_2$ vs $\eta$ At $\xi$=-0.50,-0.25, 0, +0.25,+0.50 For $\frac{\pi_1}{\pi_2} = 0$ dB.

For constant $\xi \leq 0$ slices, the vertexes of the vertical parabolas in $\lambda$ and $\eta$ will be exactly over the parabola $\eta = (\xi + 1)^2$ in the horizontal $\xi$ and $\eta$ plane defining the left boundary of the isosceles-right-triangle-like region, with heights of $\pm(1 + \xi) = \pm\sqrt{\eta}$ as described earlier from a slightly different perspective. The $\pm\infty$ values of the slopes of the $\lambda_2$ and $\lambda_1$ curves with respect to $\eta$ at the vertexes of these parabolas indicate the rapid rate of the increase in "stress" to the direction-finder for the case of $\frac{\pi_1}{\pi_2} = 1$. For constant $\xi > 0$ slices, the vertical parabolas in $\lambda$ and $\eta$ will have their vertexes located over the continuation of the just mentioned left boundary parabola in the horizontal $\xi$ and $\eta$ plane. Therefore, the apexes are outside the isosceles-right-triangle-like region, and furthermore, beyond $\eta > 1$. The curvature of the parabola is 1 at the vertex and is independent of the $\xi$ value; i.e., all the parabolas are translational copies of each other.

Taking partial derivatives of the parabolic equation with respect to $\eta$ and rearranging, we have

$$\frac{\partial}{\partial \eta}\lambda = \frac{-1}{2[\lambda - (\xi + 1)]} = \frac{\pm 1}{\sqrt{(1 + \xi)^2 - \eta}}.$$

At the $\eta = 0$ baseline, we have

$$\frac{\partial}{\partial \eta}\lambda(\xi, 0) = \frac{\pm 1}{2(1 + \xi)}.$$

For the following three special points, they are

$$\frac{\partial}{\partial \eta}\lambda(-1, 0) = \pm\infty, \quad \frac{\partial}{\partial \eta}\lambda(-1, 0) = \pm\frac{1}{2}, \quad \frac{\partial}{\partial \eta}\lambda(-1, 0) = \pm\frac{1}{4}.$$

We note that the $\pm\infty$ values are not very useful mathematical expressions, as only a single point is defined in the $\eta$ direction at the left vertex as the domain of interest is concerned. Similar remarks hold for the right vertex. These values suggest the neighborhood behavior about the vertexes, however.

For given $\xi$ and $\frac{\pi_1}{\pi_2} = 1$, as for all other values, the stress of a direction-finding scenario is highest when the baseline $\eta$ is approached. We are interested in the local behavior at the stressful region about $\eta = 0$. In this region, the large eigenvalue $\lambda_1$ will not change much in terms of its order of magnitude. This is not the case for the small eigenvalue $\lambda_2$, as it is the difference of two nearly equal numbers. The local first-order approximations to $\lambda_1$ and $\lambda_2$ near $\eta = 0$ are therefore

$$\lambda_1(\xi, \eta) \approx \lambda_1(\xi, 0) = 2(1 + \xi),$$

$$\lambda_2(\xi, \eta) \approx \frac{\eta}{2(1 + \xi)}.$$

Near $\eta = 0$ and at the three particular $\xi$ values of -1, 0, and 1, we have

$$\lambda_2(-1, \eta) \approx \infty\eta, \quad \lambda_2(0, \eta) \approx \frac{\eta}{2}, \quad \lambda_2(1, \eta) \approx \frac{\eta}{4}.$$

We can confirm these analytical findings by reviewing figure 3.5. These discussions about the local behavior of the eigenvalues near the baseline also serve as a preview of the next figure 3.6 in the next subsection.
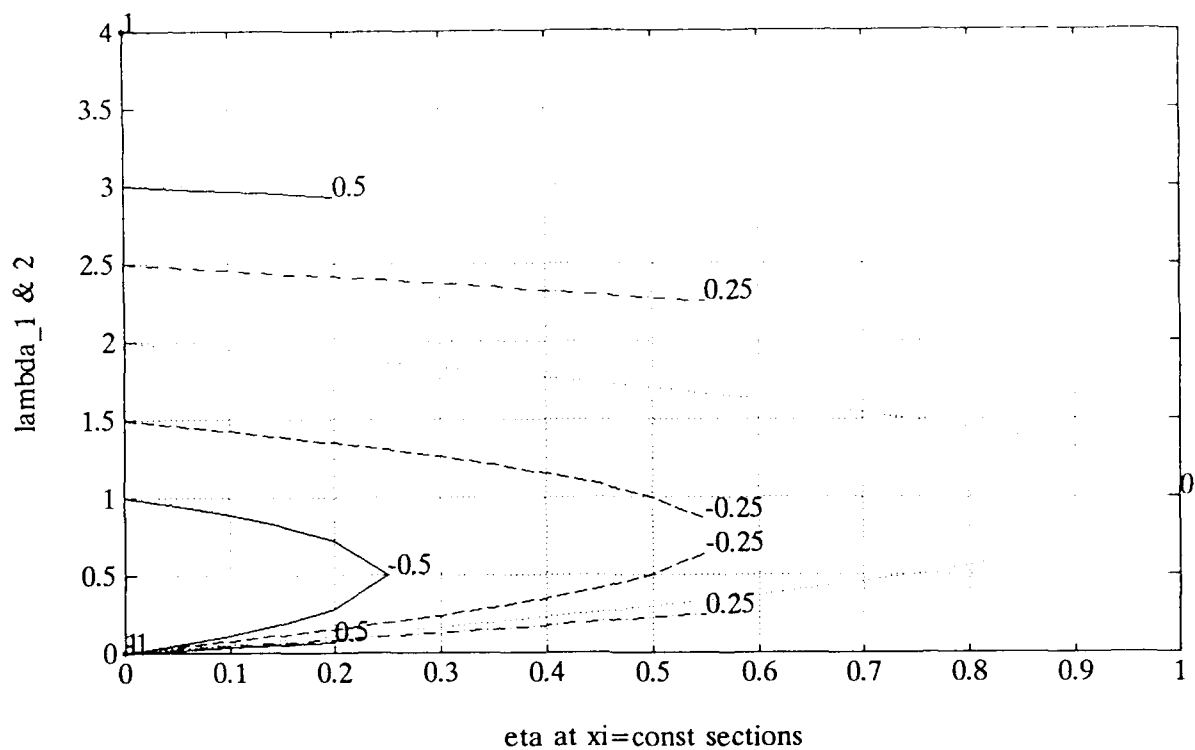
Figure 3.5: Parabolic slices:$\lambda_1$ and $\lambda_2$ vs $\eta$ at $\xi$=-0.50,-0.25, 0, +0.25,+0.50 for $\frac{\pi_1}{\pi_2} = 0$ dB.
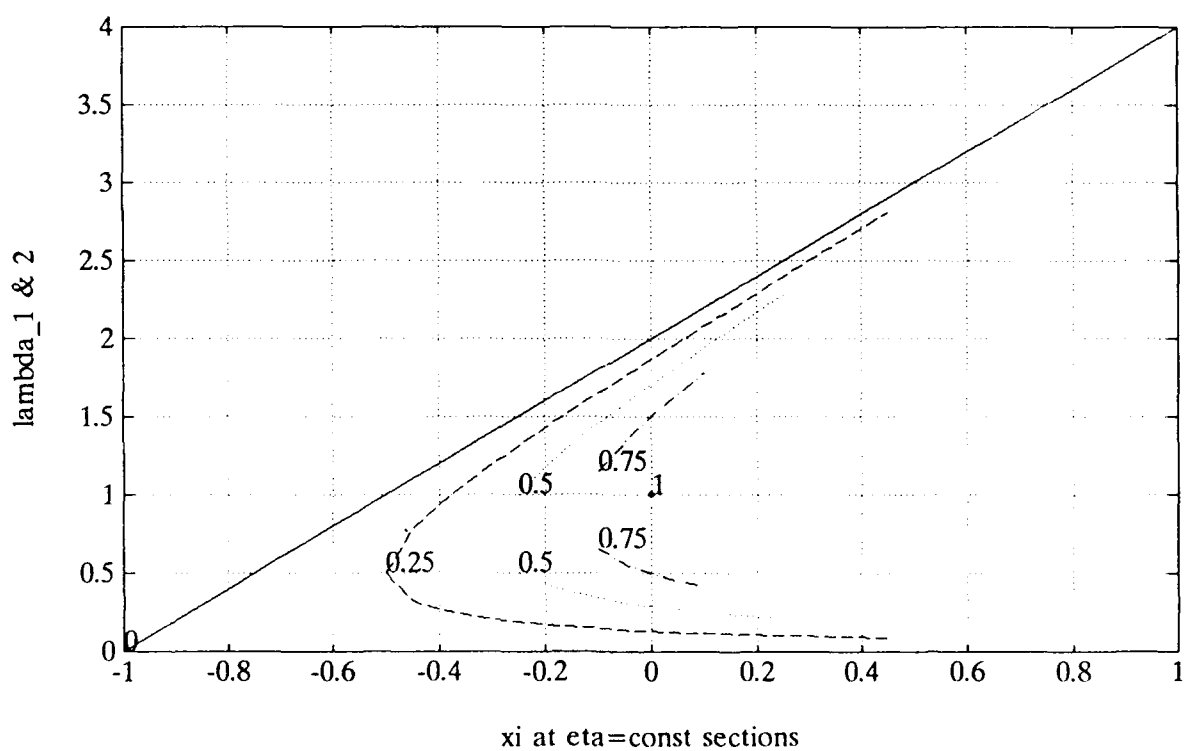


Figure 3.6: Hyperbolic slices:$\lambda_1$ and $\lambda_2$ vs $\xi$ at $\eta = 0.0, 0.25, 0.50, 0.75, 1.00$ for $\frac{\pi_1}{\pi_2} = 0$ dB.

### 3.4.3 Hyperbolic Slices for Constant Phase-Independent Variable $\eta$s

For constant $\eta$ slices, the characteristic equation can be rearranged to that of a hyperbola in $\lambda$ and $\xi$ as

$$\lambda^2 - 2\xi\lambda - 2\lambda + \eta = 0.$$

Figures 3.6 plots for $\lambda_1$ and $\lambda_2$ vs $\eta$ at $\eta = 0.0, 0.25, 0.50, 0.75, 1.00$ for $\frac{\pi_1}{\pi_2} = 0$ dB.

We defer the derivation and characterization of these hyperbolas to appendix A and the next section for the general case. We mention a few results here.

The two straight lines represented by $\lambda_1$ and $\lambda_2$ over the baseline $\eta = 0$ are those of a degenerate hyperbola from a one-parameter $\eta$ family of hyperbolas in $\lambda$ and $\xi$ sharing common asymptotes when the parameter $\eta$ is 0. The common asymptotes are the two straight lines.

Having defined the common asymptotes of this family of hyperbolas, the next important property is how the vertex varies when $\eta$ increases from 0 to 1. Define $\Xi_V$ as the distance from the vertex to the intersection of the common asymptotes. We note that $\Xi_V$ is proportional to $\sqrt{\eta}$, i.e., $\Xi_V$ at $\eta = \frac{1}{4}$ is half of $\Xi_V$ at $\eta = 1$.

### 3.4.4 Contours for Eigenvalue Ratio $\frac{\lambda_1}{\lambda_2}$

Consider the one-parameter family of parabolas $\frac{\eta}{2(\xi+1)^2} = p$ parameterized by $p$ from 0 to 1. The parabolas have their vertices colocated at $(\xi, \eta) = (-1, 0)$, i.e., at the lower left corner of the isosceles-like triangle and their common tangent the baseline $\eta = 0$. When p=0, the parabola is the baseline $\eta = 0$. When p=1, the parabola is the left boundary of the isosceles-like triangle $\eta = (\xi + 1)^2$. Therefore, this one-parameter family of parabolas will cover the whole isosceles-like triangle when the parameter $p$ is varied from 0 to 1.

We need to find the shape of the contours of the eigenvalue ratio $\frac{\lambda_1}{\lambda_2} = l$, i.e.,

$$\frac{\lambda_1}{\lambda_2} = \frac{(1+\xi) + \sqrt{(1+\xi)^2 - \eta}}{(1+\xi) - \sqrt{(1+\xi)^2 - \eta}} = l.$$

Having set up the problem in this way, it is easy to see that the contours of the eigenvalue ratio $\frac{\lambda_1}{\lambda_2} = l$ are the same one-parameter family of parabolas introduced above with the conversion between the parabola parameter $\frac{\eta}{2(\xi+1)^2} = p$ and eigenvalue ratio $\frac{\lambda_1}{\lambda_2} = l$ as

$$p = \frac{4l}{(l+1)^2} \text{ or } l = \frac{2 - p + \sqrt{4 - 4p}}{p}.$$

We can reacquaint ourselves with the previously found result that the eigenvalue ratio $\frac{\lambda_1}{\lambda_2} = l$ is 1 on the left boundary of the isosceles-like triangle $\eta = (\xi+1)^2$ and 0 on the baseline $\eta = 0$. The dB-scale contour plot for this equal strength arrival case is presented in fig. 5.10 in section 5.2. Because the contours of $\frac{\lambda_1}{\lambda_2} = l$ pass through the lower left corner of the isosceles-like triangle, this corner is a point of discontinuity for the eigenvalue ratio $\frac{\lambda_1}{\lambda_2}$ for the special case of equal strength $\frac{\pi_1}{\pi_2} = 0$ dB.

35

## 3.5 General Case

The quadratic equation from the characteristic polynomial has the form

$$\lambda^2 - (1 + \frac{\pi_1}{\pi_2} + \sqrt{\frac{\pi_1}{\pi_2}}2\xi)\lambda + \frac{\pi_1}{\pi_2}\eta = 0.$$

### 3.5.1 Straight Line Contours for Constant Eigenvalue $\lambda$s

From the quadratic equation, we can see that the constant $\lambda$s' contours remain straight lines in the $\xi$ and $\eta$ plane as in the special case $\frac{\pi_1}{\pi_2} = 1$ as

$$\eta + (\frac{\pi_1}{\pi_2})^{-1}\lambda^2 = 2(\frac{\pi_1}{\pi_2})^{-\frac{1}{2}}\lambda\left[\xi + \frac{1}{2}(\frac{\pi_1}{\pi_2})^{-\frac{1}{2}} + (\frac{\pi_1}{\pi_2})^{-1})\right].$$

The mesh and contour plots of $\lambda_1$ are shown in figures 3.7, 3.9, and 3.11 for $\frac{\pi_1}{\pi_2} = 10, 20, 30$ dB respectively. The corresponding plots of $\lambda_2$ are shown in figures 3.8, 3.10, and 3.12. These straight lines have positive slopes $2\lambda_i(\frac{\pi_1}{\pi_2})^{-\frac{1}{2}}$ and intercept of $-(\frac{\pi_1}{\pi_2})^{-1}\lambda_i^2$ with the vertical line passing through the left vertex

$$(-\frac{1}{2}\left[(\frac{\pi_1}{\pi_2})^{-\frac{1}{2}} + (\frac{\pi_1}{\pi_2})^{-1}\right], 0).$$

As $\frac{\pi_1}{\pi_2}$ increases from unity, the slope of the contours of $\lambda_2$ are smaller as the range of $\lambda_2$ is still between 0 and 1. The slope of the contours of $\lambda_1$ are larger as the range of $\lambda_1$ is of the order of $\frac{\pi_1}{\pi_2}$ rather than that of $\sqrt{\frac{\pi_1}{\pi_2}}$. In other words, the variation of the large eigenvalue $\lambda_1$ is essentially along the direction of the horizontal phase-dependent variable $\xi$, and the variation of the small eigenvalue $\lambda_2$ is essentially along the direction of the vertical phase-independent variable $\eta$.

### 3.5.2 Parabolic Slices for Constant Phase-Dependent Variable $\xi$s

For constant $\xi$ slices, the characteristic equation can be rearranged to that of a parabola in $\lambda$ and $\eta$ as

$$\left[\lambda - \frac{1}{2}(1 + \frac{\pi_1}{\pi_2} + \sqrt{\frac{\pi_1}{\pi_2}}2\xi)\right]^2 = -\frac{\pi_1}{\pi_2}\left[\eta - \frac{(1 + \frac{\pi_1}{\pi_2} + \sqrt{\frac{\pi_1}{\pi_2}}2\xi)^2}{4\frac{\pi_1}{\pi_2}}\right].$$

Figures 3.13, 3.15, and 3.17 plot for $\lambda_1$ And $\lambda_2$ vs $\eta$ At $\xi$=-0.50,-0.25, 0, +0.25,+0.50 For $\frac{\pi_1}{\pi_2} = 10, 20, 30$ dB.

We note that for given $\xi$, both coordinates of the vertex of the parabola increase with respect to $\frac{\pi_1}{\pi_2}$, as their derivatives with respect to $\frac{\pi_1}{\pi_2}$ have the following forms

$$\frac{\partial}{\partial\frac{\pi_1}{\pi_2}}\left[\frac{1}{2}(1 + \frac{\pi_1}{\pi_2} + \sqrt{\frac{\pi_1}{\pi_2}}2\xi)\right] = \frac{1}{2}\left[1 + \frac{1}{2}(\frac{\pi_1}{\pi_2})^{-\frac{1}{2}}2\xi\right] \geq 0,$$

$$\frac{\partial}{\partial\frac{\pi_1}{\pi_2}}\left[\frac{(1 + \frac{\pi_1}{\pi_2} + \sqrt{\frac{\pi_1}{\pi_2}}2\xi)^2}{4\frac{\pi_1}{\pi_2}}\right]$$

36

Figure 3.7: Straight line contours of $\lambda_1$ for $\frac{\pi_1}{\pi_2} = 10$ dB.
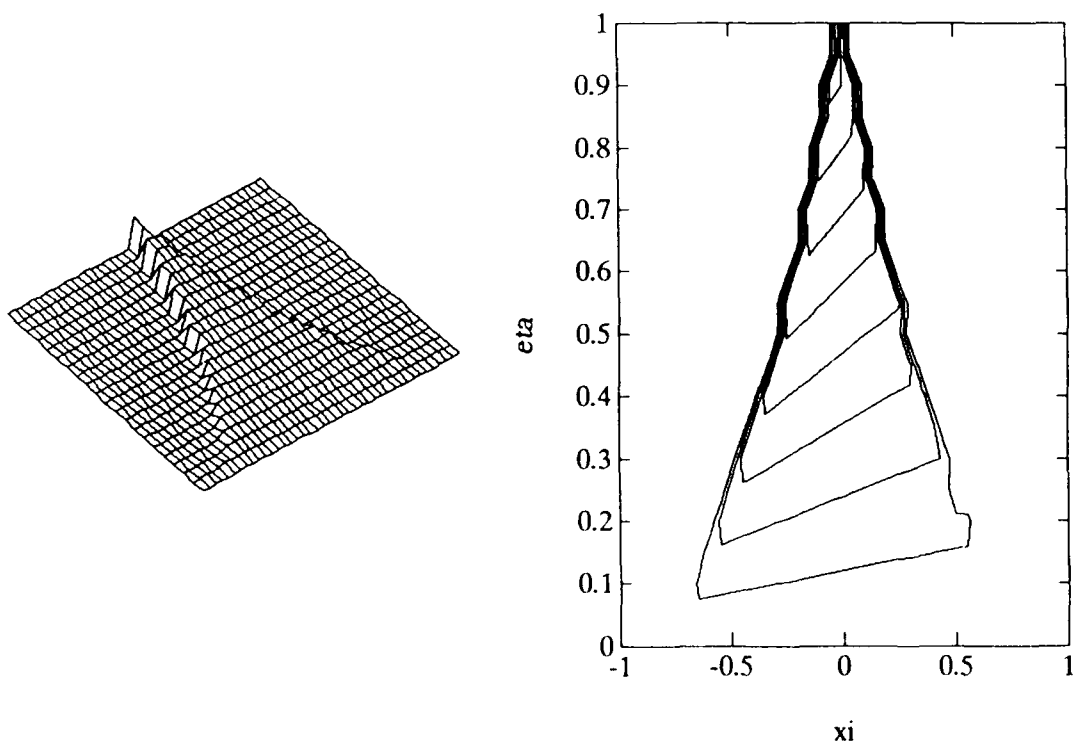


Figure 3.8: Straight line contours of $\lambda_2$ for $\frac{\pi_1}{\pi_2} = 10$ dB.

37
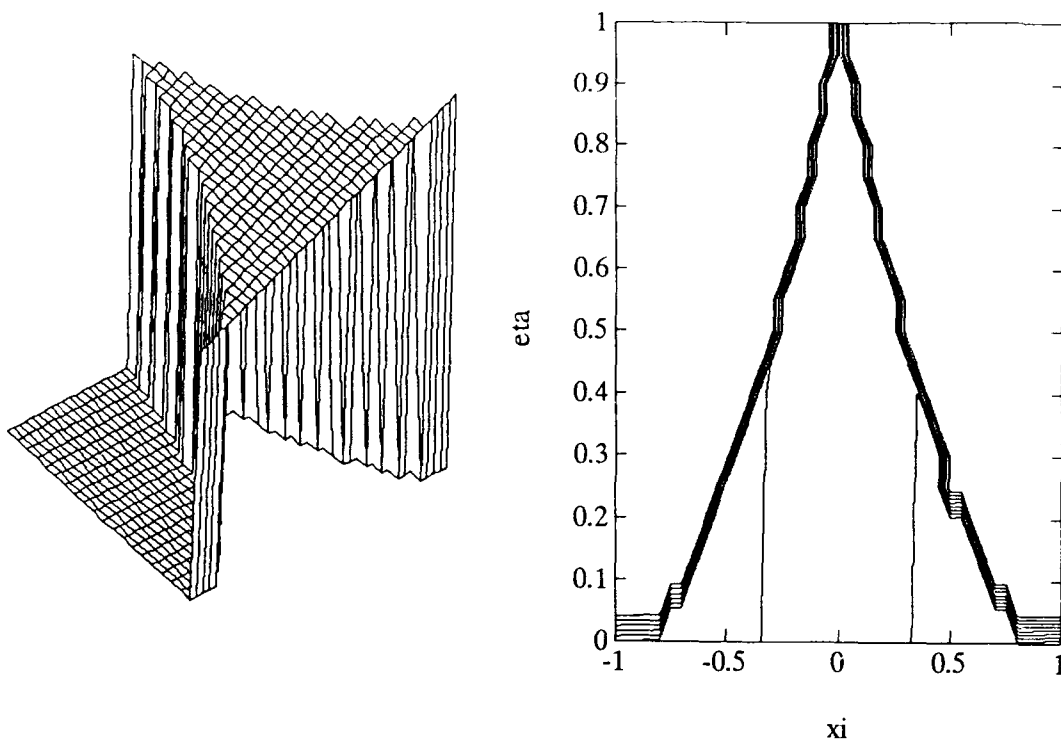
Figure 3.9: Straight line contours of $\lambda_1$ for $\frac{\pi_1}{\pi_2} = 20$ dB.
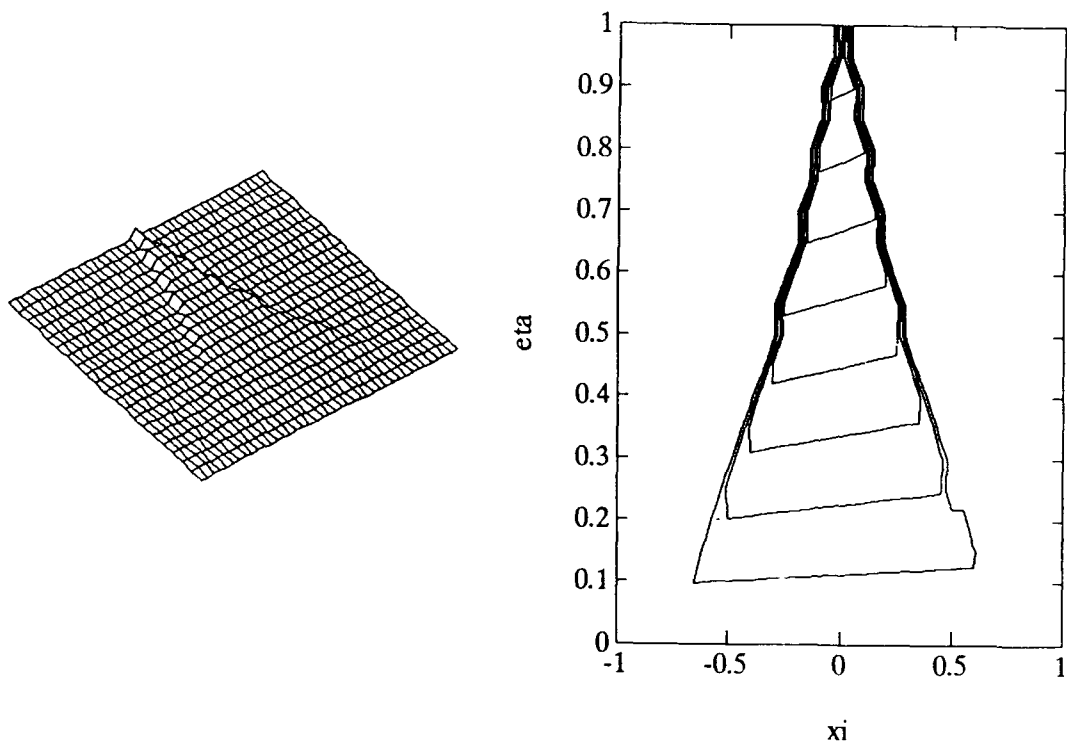


Figure 3.10: Straight line contours of $\lambda_2$ for $\frac{\pi_1}{\pi_2} = 20$ dB.
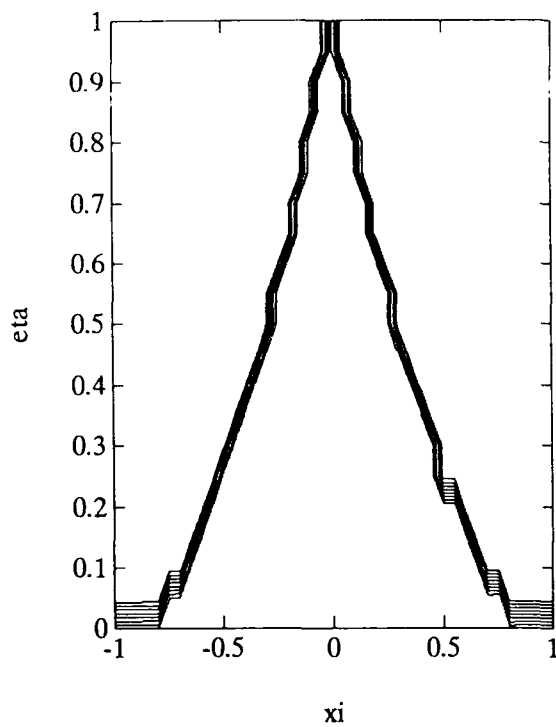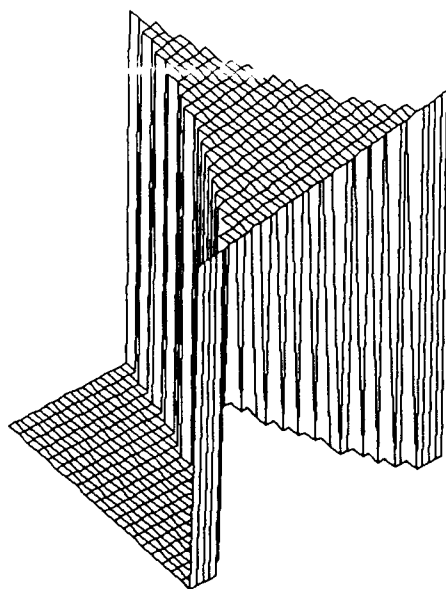
Figure 3.11: Straight line contours of $\lambda_1$ for $\frac{\pi_1}{\pi_2} = 30$ dB.
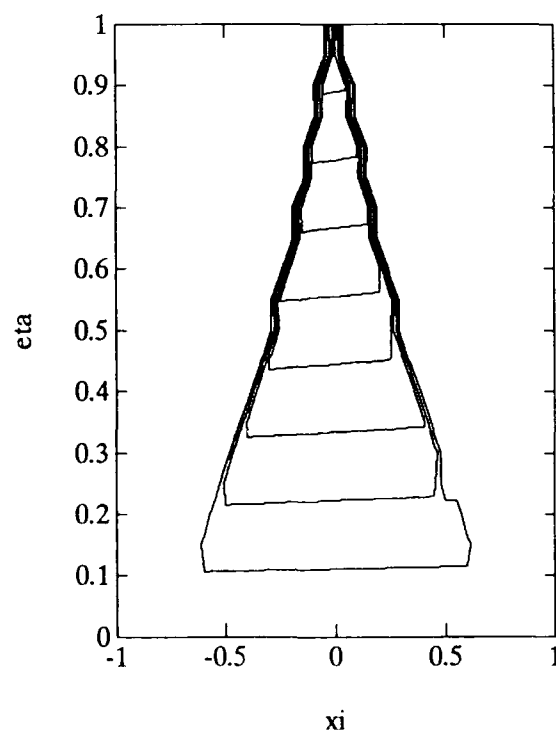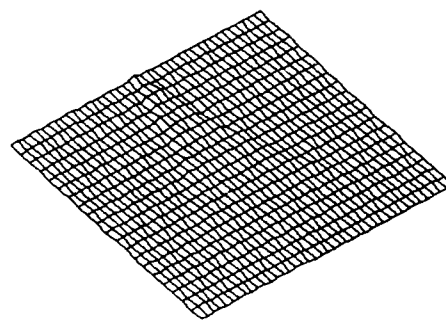


Figure 3.12: Straight line contours of $\lambda_2$ for $\frac{\pi_1}{\pi_2} = 30$ dB.
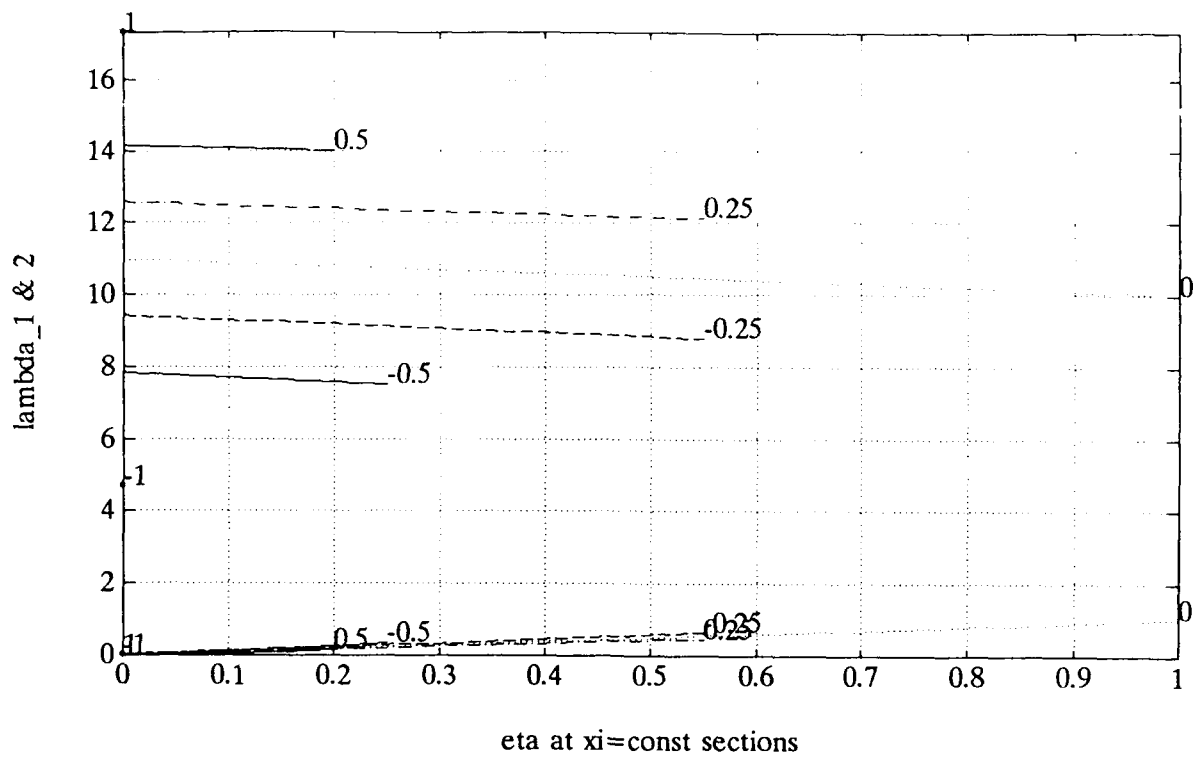
Figure 3.13: Parabolic slices:$\lambda_1$ and $\lambda_2$ vs $\eta$ at $\xi$=−0.50,−0.25, 0, +0.25,+0.50 for $\frac{\pi_1}{\pi_2} = 10$ dB.
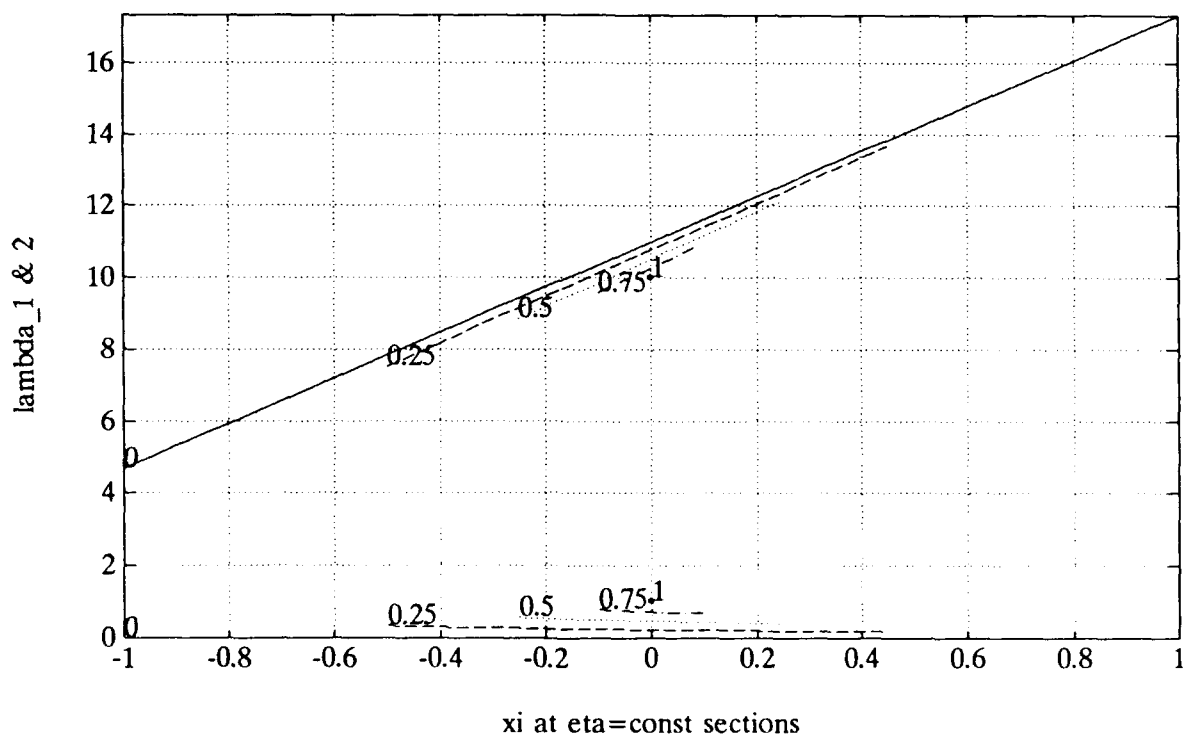


Figure 3.14: Hyperbolic slices:$\lambda_1$ and $\lambda_2$ vs $\xi$ at $\eta = 0.0, 0.25, 0.50, 0.75, 1.00$ for $\frac{\pi_1}{\pi_2} = 10$ dB.
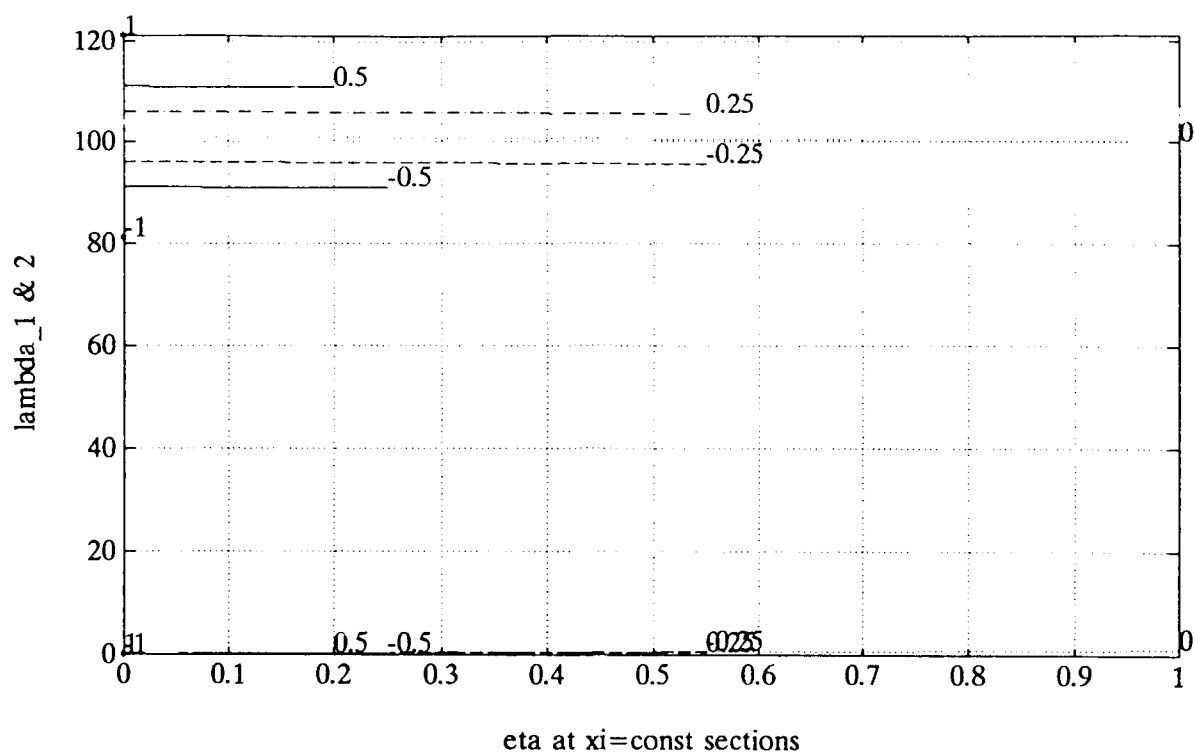
Figure 3.15: Parabolic slices:$\lambda_1$ and $\lambda_2$ vs $\eta$ at $\xi=-0.50,-0.25, 0, +0.25,+0.50$ for $\frac{\pi_1}{\pi_2} = 20$ dB.
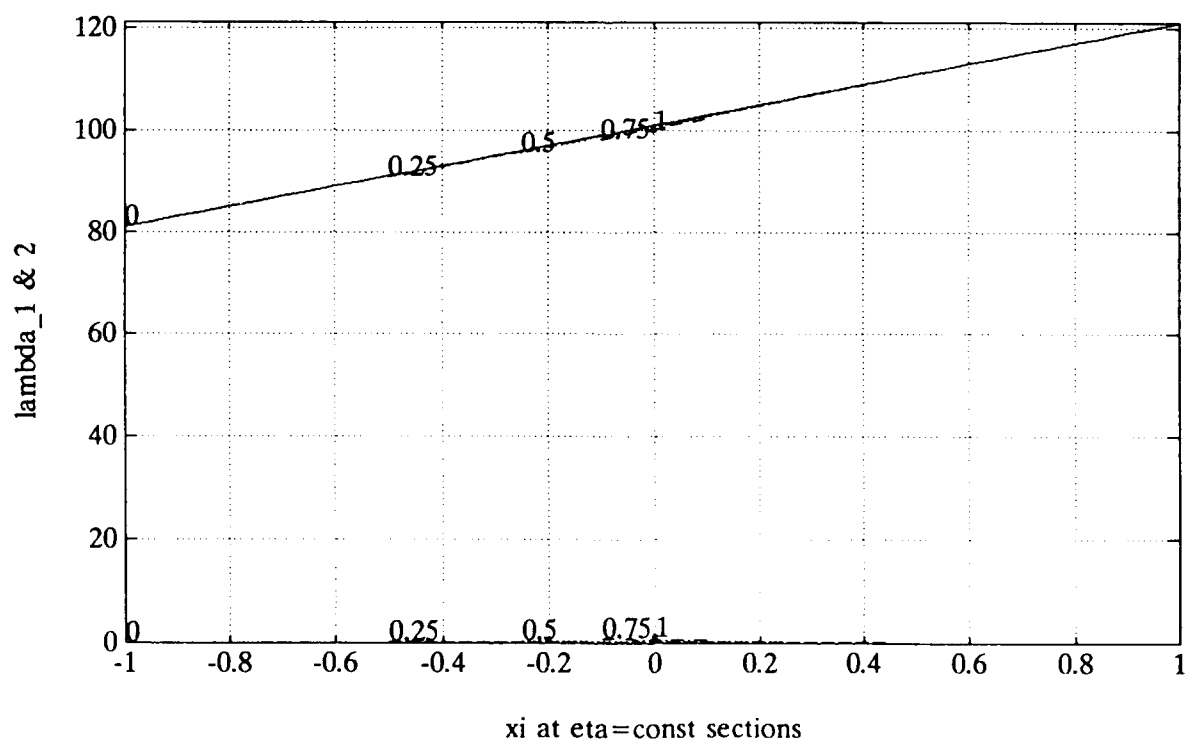


Figure 3.16: Hyperbolic slices:$\lambda_1$ and $\lambda_2$ vs $\xi$ at $\eta = 0.0, 0.25, 0.50, 0.75, 1.00$ for $\frac{\pi_1}{\pi_2} = 20$ dB.
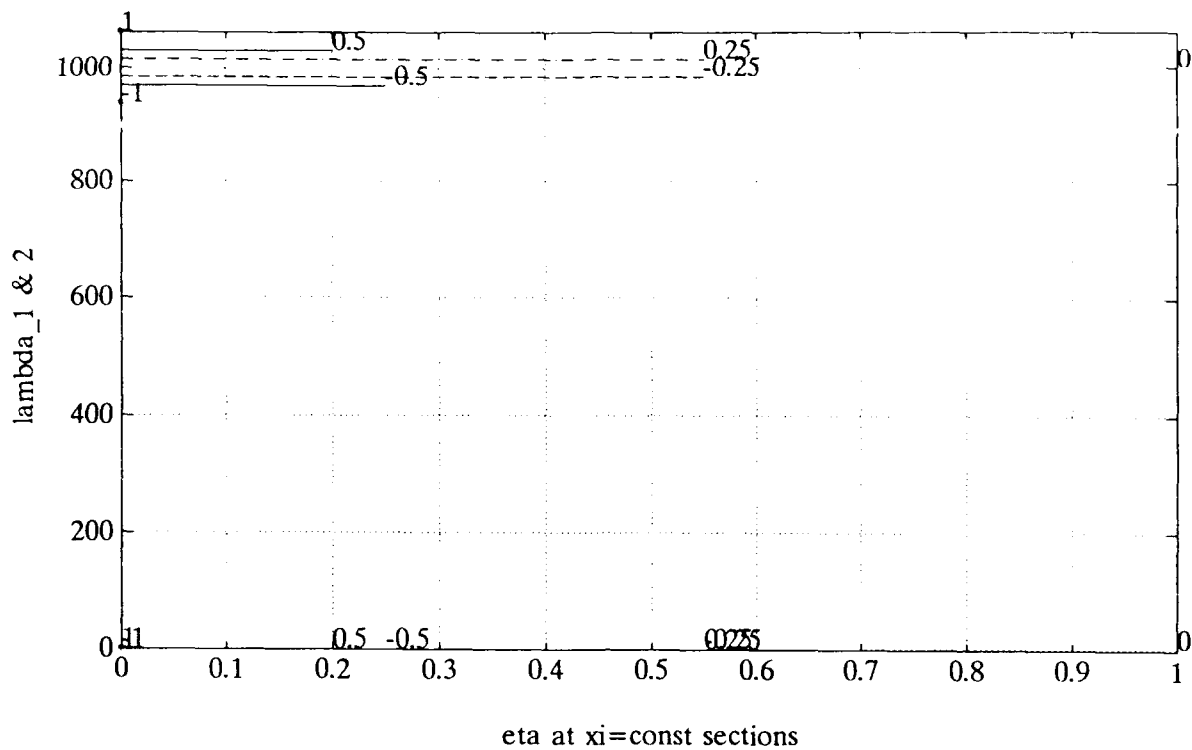
Figure 3.17: Parabolic slices:$\lambda_1$ and $\lambda_2$ vs $\eta$ at $\xi$=-0.50,-0.25, 0, +0.25,+0.50 for $\frac{\pi_1}{\pi_2} = 30$ dB.
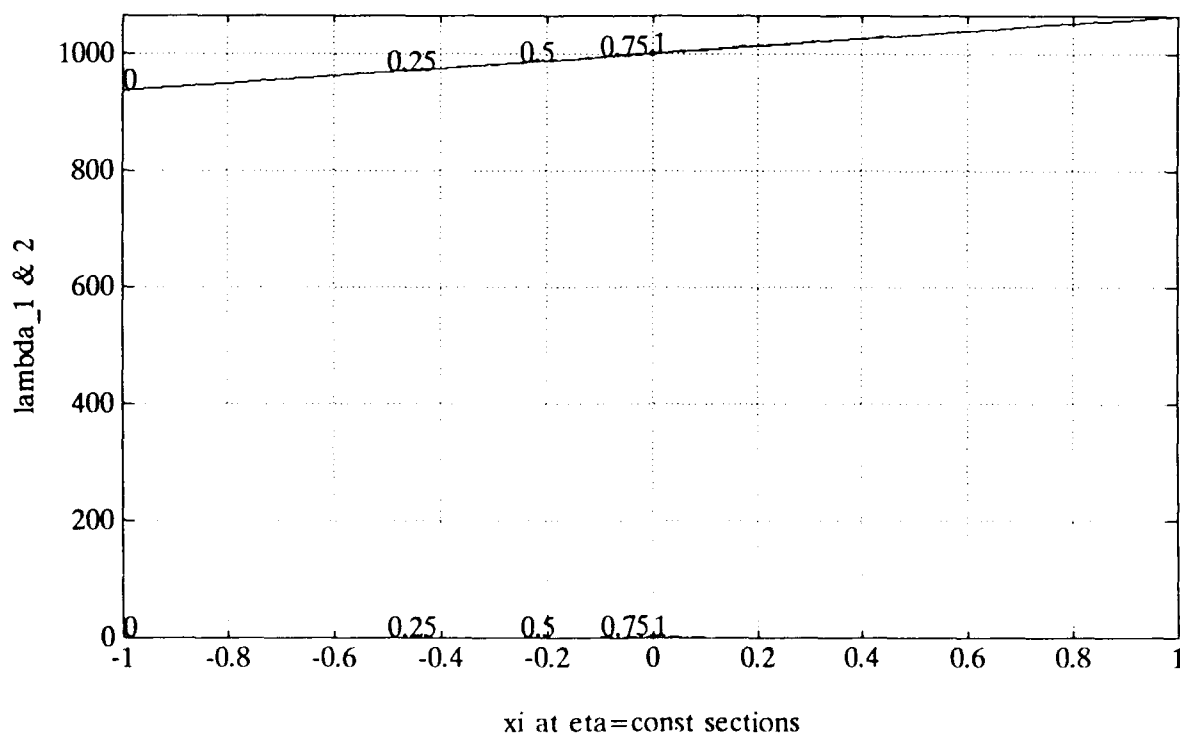


Figure 3.18: Hyperbolic slices:$\lambda_1$ and $\lambda_2$ vs $\xi$ at $\eta = 0.0, 0.25, 0.50, 0.75, 1.00$ for $\frac{\pi_1}{\pi_2} = 30$ dB.

42

$$= \frac{(1 + \frac{\pi_1}{\pi_2} + \sqrt{\frac{\pi_1}{\pi_2}} 2\xi)}{4\frac{\pi_1}{\pi_2}} \left[ 2 + (\frac{\pi_1}{\pi_2})^{-\frac{1}{2}} 2\xi - \frac{(1 + \frac{\pi_1}{\pi_2} + \sqrt{\frac{\pi_1}{\pi_2}} 2\xi)}{\frac{\pi_1}{\pi_2}} \right]$$

$$= \left[ \frac{(1 + \sqrt{\frac{\pi_1}{\pi_2}} \xi)^2 + (1 - \xi^2)\frac{\pi_1}{\pi_2}}{4\frac{\pi_1}{\pi_2}} \right] (1 - \frac{1}{\frac{\pi_1}{\pi_2}}) \geq 0.$$

Therefore, as $\frac{\pi_1}{\pi_2}$ increases from 1, those parabolas originally connected in $\lambda$ and $\eta$ on the left-half of the domain of interest in the $\xi$ and $\eta$ plane, i.e., $\xi \leq 0$, start to depart from each other. Those parabolas on the right-half of the domain of interest, i.e., at $\xi > 0$ and already separated when $\frac{\pi_1}{\pi_2} = 1$, separate even farther as $\frac{\pi_1}{\pi_2}$ increases.

The curvature of each parabola is $2(\frac{\pi_1}{\pi_2})^{-1}$ at the vertex which is outside of the domain of interest as mentioned earlier. For given $\frac{\pi_1}{\pi_2}$, the curvature is independent of the $\xi$ value and all the parabolas are exact translational copies of each other.

Taking partial derivatives of the parabolic equation with respect to $\eta$ and rearranging, we have

$$\frac{\partial}{\partial \eta} \lambda = \frac{-\frac{\pi_1}{\pi_2}}{2 \left[ \lambda - \frac{1}{2}(1 + \frac{\pi_1}{\pi_2} + \sqrt{\frac{\pi_1}{\pi_2}} 2\xi) \right]} = \frac{\pm\sqrt{\frac{\pi_1}{\pi_2}}}{2\sqrt{\frac{(1 + \frac{\pi_1}{\pi_2} + \sqrt{\frac{\pi_1}{\pi_2}} 2\xi)^2}{4\frac{\pi_1}{\pi_2}} - \eta}}.$$
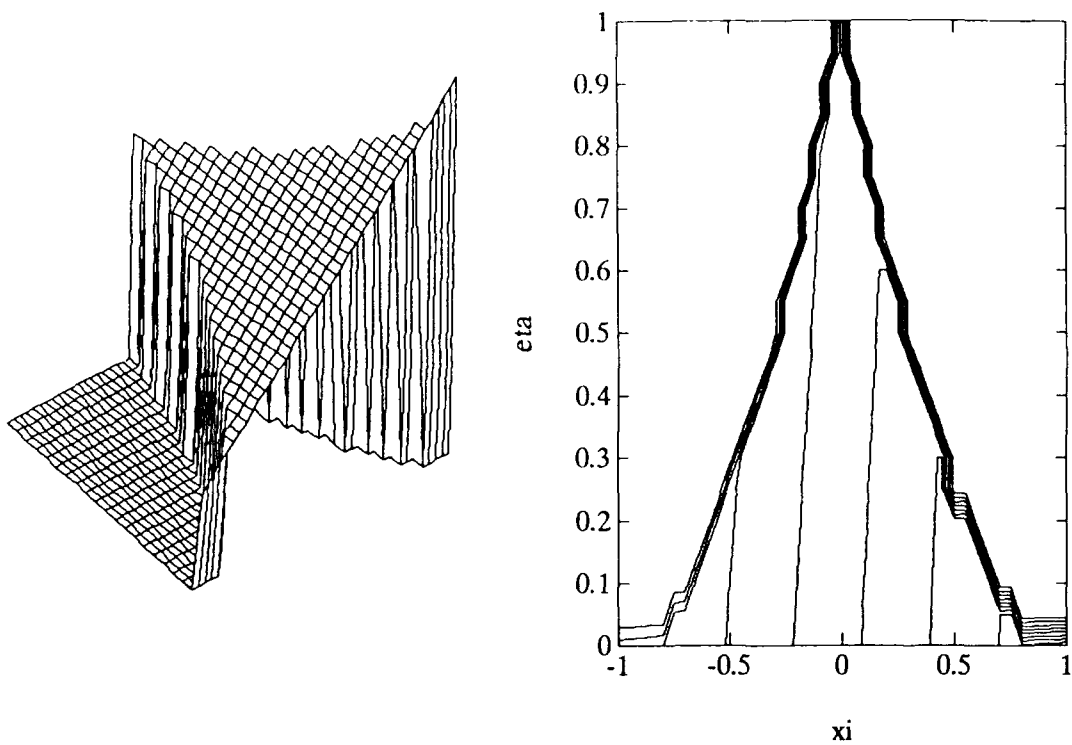
At $\eta = 0$, we have

$$\frac{\partial}{\partial \eta} \lambda(\xi, 0) = \frac{\pm\frac{\pi_1}{\pi_2}}{1 + \frac{\pi_1}{\pi_2} + \sqrt{\frac{\pi_1}{\pi_2}} 2\xi}.$$

For large $\frac{\pi_1}{\pi_2}$, we have the following approximation

$$\frac{\partial}{\partial \eta} \lambda(\xi, 0) \approx \pm 1.$$

The local first-order approximations to $\lambda$s near $\eta = 0$ are therefore

$$\lambda_1(\xi, \eta) \approx \lambda_1(\xi, 0) = \frac{\pi_1}{\pi_2} + 1 + \sqrt{\frac{\pi_1}{\pi_2}} 2\xi,$$

$$\lambda_2(\xi, \eta) \approx \eta.$$

We note the important observation that the smaller eigenvalue is essentially independent of both $\xi$ and $\frac{\pi_1}{\pi_2}$ near the baseline for large $\frac{\pi_1}{\pi_2}$. The ratio $\frac{\pi_1}{\pi_2}$ essentially only affects the large eigenvalue. The large eigenvalue is not sensitive to whether the scenario's $(\xi, \eta)$ coordinate is close to the baseline, i.e., whether the arrivals are highly temporally correlated and/or spatially close to each other.

### 3.5.3 Hyperbolic Slices for Constant Phase-Independent Variable $\eta$s

For constant $\eta$ slices, the characteristic equation can be rearranged to that of a hyperbola in $\lambda$ and $\xi$ as

$$\lambda^2 - \sqrt{\frac{\pi_1}{\pi_2}} 2\xi\lambda - (1 + \frac{\pi_1}{\pi_2})\lambda + \frac{\pi_1}{\pi_2}\eta = 0.$$

In fact, for each $\frac{\pi_1}{\pi_2}$ value, this describes a one parameter $\eta$ family of hyperbolas in $\lambda$ and $\xi$ that share common asymptotes. We defer the derivation and some of the characterization of

43

these hyperbolas to the appendix. Figures 3.14, 3.16, and 3.18 plot for $\lambda_1$ and $\lambda_2$ vs $\xi$ at $\eta = 0.0, 0.25, 0.50, 0.75, 1.00$ for $\frac{\pi_1}{\pi_2} = 10, 20, 30$ dB respectively.

For a given $\eta$, the constant $\eta$ slices of $\lambda_1$ and $\lambda_2$ curves as functions of $\xi$ are the truncated parts of the same hyperbola in $\lambda$ and $\xi$. Because of this characterization, $(\lambda_1)_{max}$ and $(\lambda_2)_{min}$ occur at the same place, $\xi_{max}$. This is convenient, as we are not yet sure whether we can consolidate the two possible "stress" measures, $\lambda_2$ and $\frac{\lambda_1}{\lambda_2}$, into one. Therefore, the worst point is always at the right vertex of the baseline, corresponding to constructive interference.

The higher $\frac{\pi_1}{\pi_2}$ values, as contrasted to the special case of $\frac{\pi_1}{\pi_2} = 1$, have wider separation of the $\lambda_1$ and $\lambda_2$ surfaces. The truncated parts of each hyperbola in $\lambda$ and $\xi$ above the isosceles-right-triangle-like region get closer to the asymptotes, as the intersection of the two asymptotes $(-\frac{1}{2}(1+\frac{\pi_1}{\pi_2})/\sqrt{\frac{\pi_1}{\pi_2}}, 0)$ moves to the left from $(-1, 0)$. Above the baseline, i.e., at $\eta = 0$, the maximum change of $\lambda_1$ with respect to its mid-point value for $\frac{\pi_1}{\pi_2} \gg 1$ is

$$\frac{4\sqrt{\frac{\pi_1}{\pi_2}}}{1 + \frac{\pi_1}{\pi_2}} = O(\frac{1}{\sqrt{\frac{\pi_1}{\pi_2}}}).$$

That is, the dependence of $\lambda$s on $\xi$ becomes more insignificant as $\frac{\pi_1}{\pi_2}$ gets large.

### 3.5.4 Contours for Eigenvalue Ratio $\frac{\lambda_1}{\lambda_2}$

We need to know the shape of the contours of the eigenvalue ratio $\frac{\lambda_1}{\lambda_2} = l$, i.e.,

$$\frac{\lambda_1}{\lambda_2} = \frac{1 + \sqrt{\phantom{x}}}{1 - \sqrt{\phantom{x}}} = l,$$

where $\sqrt{\phantom{x}}$ assumes the expression from section 3.1

$$\sqrt{1 - \frac{4(\frac{\pi_1}{\pi_2})\eta}{\left[\frac{\pi_1}{\pi_2} + 1 + (\frac{\pi_1}{\pi_2})^{\frac{1}{2}}2\xi\right]^2}}.$$

This is equivalent to

$$1 - \frac{4(\frac{\pi_1}{\pi_2})\eta}{\left[\frac{\pi_1}{\pi_2} + 1 + (\frac{\pi_1}{\pi_2})^{\frac{1}{2}}2\xi\right]^2} = (\frac{l-1}{l+1})^2,$$

or

$$\frac{4(\frac{\pi_1}{\pi_2})\eta}{\left[\frac{\pi_1}{\pi_2} + 1 + (\frac{\pi_1}{\pi_2})^{\frac{1}{2}}2\xi\right]^2} = \frac{4l}{(l+1)^2}.$$

The contours of the eigenvalue ratio $\frac{\lambda_1}{\lambda_2} = l$ for fixed $\frac{\pi_1}{\pi_2}$ form a one-parameter family of parabolas having their vertices colocated at $(\xi, \eta) = (-\frac{1}{2}(1 + \frac{\pi_1}{\pi_2})/\sqrt{\frac{\pi_1}{\pi_2}}, 0)$, i.e., the intersection of the two asymptotes described in the last subsection, and their common tangent the baseline $\eta = 0$. Compared to the equipower arrival case, we note that this common vertex has moved to the left from $(-1, 0)$ and is now outside of the isosceles-like region. As a parabola has its largest curvature at its apex, the contours over the isosceles-like region should have less curvature as the $\frac{\pi_1}{\pi_2}$ increases. This can be seen from the dB-scale contour plots presented in section 5.2 in figures 5.12, 5.14, and 5.16 for power ratio $\frac{\pi_1}{\pi_2} = 10, 20, 30$ dB respectively.

We can also characterize the contours of the eigenvalue ratio $\frac{\lambda_1}{\lambda_2} = l$ for $\xi = 0$ from

$$\log_{10} \eta = 2 \log_{10}(\frac{\pi_1}{\pi_2} + 1) - \log_{10}(\frac{\pi_1}{\pi_2}) + \log_{10}(\frac{4l}{(l+1)^2}) \approx \log_{10}(\frac{\pi_1}{\pi_2}) + \log_{10}(\frac{4l}{(l+1)^2}).$$

Therefore, for large $\frac{\pi_1}{\pi_2}$, the contours of the eigenvalue ratio $\frac{\lambda_1}{\lambda_2} = l$ for $\xi = 0$ as functions of $\frac{\pi_1}{\pi_2}$ and $\eta$ are 45° parallel lines with all three variables $\frac{\lambda_1}{\lambda_2} = l$, $\frac{\pi_1}{\pi_2}$, and $\eta$ in dB scale. This can be seen from the dB-scale contour plot presented in section 5.2 in figure 5.32.

## 3.6 Specializing Speiser's Eigenvalue Bounds to Two Sources

As we have the exact expressions of the eigenvalues for the two-source scenario, we can examine quantitatively some general multisource results by specializing them to this case. For example, we consider the singular value bounds derived by Speiser and Arnold[51] for the product of two square matrices. Specialized to the two-source scenario and in terms of eigenvalues in our context, his expression can be written as

$$\sigma_2^2(P)\sigma_2^2(\Psi) \leq \lambda_2 \leq \min\left[\sigma_2^2(P)\sigma_1^2(\Psi), \sigma_1^2(P)\sigma_2^2(\Psi)\right],$$

where

$$P = \begin{bmatrix} \frac{\pi_1}{\pi_2} & \sqrt{\frac{\pi_1}{\pi_2}}\rho \\ \sqrt{\frac{\pi_1}{\pi_2}}\rho^* & 1 \end{bmatrix},$$

$$\Psi = \begin{bmatrix} 1 & \phi \\ \phi^* & 1 \end{bmatrix},$$

and $\sigma_i^2(\Psi)$ is the i-th largest eigenvalue of the Hermitian matrix $\Psi$, and from section 3.1

$$\lambda_i = \sigma_i^2(P\Psi).$$

It is easy to see that

$$\sigma_i^2(\Psi) = 1 \pm |\phi|.$$

This corresponds to $\lambda_i$ for the special case $\xi = 0$, i.e., at the vertical axis, with $P$ being identity, the temporally uncorrelated equal-powered arrival case. We also have

$$\sigma_i^2(P) = \frac{1}{2}(\frac{\pi_1}{\pi_2} + 1)\left[1 \pm \sqrt{1 - \frac{4(\frac{\pi_1}{\pi_2})(1 - |\rho|^2)}{(\frac{\pi_1}{\pi_2} + 1)^2}}\right].$$

This corresponds to $\lambda_i$ for the special case $\xi = 0$, i.e., at the vertical axis, with $\Psi$ being identity, the spatially orthogonal arrival case.

Given these algebraic expressions, we now interpret their physical significance. In chapter , we discussed the three main sources for the signal eigenvalue spread or causes for small signal eigenvalues. They are the high spatial correlation $\phi$ due to narrow spatial separation between two arrivals, the high temporal correlation $\rho$ because of multipaths, and the high strength contrast $\frac{\pi_1}{\pi_2}$. We note that $\phi$ appears in $\Psi$, $\rho$ and $\frac{\pi_1}{\pi_2}$ in $P$. Speiser's eigenvalue bounds for the product of two matrices tell us that if we know the eigenvalues of $\Psi$ and $P$, then we can bound the eigenvalues, $\lambda_2 = \sigma_2^2(P\Psi)$, of the product matrix. Stated loosely, if we know the partial stress from spatial correlation alone and that from temporal correlation together with the power contrast, we can bound the joint stress from all of the above combined sources. From the above expressions, we know that the partial stresses $\sigma_2^2(\Psi)$ and $\sigma_2^2(P)$ depend on $\phi$ and $\rho$ constrained on the two unit-disks only through their magnitudes, i.e., radii, but not the angular positions. Yet the combined stresses $\lambda_2 = \sigma_2^2(P\Psi)$ depend also on the relative phasor positions. As we have used the natural many-to-one mapping from $(\rho, \phi)$ to $(\xi, \eta)$ which appeared in the eigenvalue formulas in section 3.1, we note that the relative phasor positions appeared only in the phase-dependent variable $\xi$.

For given $|\rho|$ and $|\phi|$, we have $\eta = (1 - |\phi|^2)(1 - |\rho|^2)$ and $|\xi|_{\max} = |\rho||\phi|$. It is of interest to see whether Speiser's upper and lower bounds for $\lambda_2$ coincide with $\lambda_2(-|\rho||\phi|, (1 - |\phi|^2)(1 - |\rho|^2))$ and $\lambda_2(|\rho||\phi|, (1 - |\phi|^2)(1 - |\rho|^2))$. We also like to know whether these bounds are tight or loose as the scenario points range over the isosceles region for the equipowered arrival $\frac{\pi_1}{\pi_2} = 1$ case and the large power-ratio case.

### 3.6.1 For the Special Equipower Case $\frac{\pi_1}{\pi_2} = 1$

For $\frac{\pi_1}{\pi_2} = 1$, Speiser's expression states that

$$(1 - |\rho|)(1 - |\phi|) \leq \lambda_2 \leq \min\left[(1 + |\phi|)(1 - |\rho|), (1 - |\phi|)(1 + |\rho|)\right]$$
$$= (1 - |\rho||\phi|) - |\,|\rho| - |\phi|\,|.$$

These bounds have exactly the same expressions for $\lambda_2$ at the end points of the permissible $\xi$-interval between $(-|\rho||\phi|, (1 - |\phi|^2)(1 - |\rho|^2))$ and $(|\rho||\phi|, (1 - |\phi|^2)(1 - |\rho|^2))$ when $\frac{\pi_1}{\pi_2} = 1$ as shown in the following.

For a given $\eta$ value and $\frac{\pi_1}{\pi_2} = 1$, as $\xi$ varies from the left edge of the permissible $\xi$-interval to the midpoint and then to the right edge, $\lambda_2$ decreases from

$$\lambda_2(-|\rho||\phi|, (1 - |\phi|^2)(1 - |\rho|^2))$$
$$= (1 - |\rho||\phi|) - \sqrt{(1 - |\rho||\phi|)^2 - (1 - |\phi|^2)(1 - |\rho|^2)}$$
$$= (1 - |\rho||\phi|) - ||\rho| - |\phi||,$$

to

$$\lambda_2(0, (1 - |\phi|^2)(1 - |\rho|^2)) = 1 - \sqrt{1 - (1 - |\phi|^2)(1 - |\rho|^2)},$$

to

$$\lambda_2(|\rho||\phi|, (1 - |\phi|^2)(1 - |\rho|^2))$$
$$= (1 + |\rho||\phi|) - \sqrt{(1 + |\rho||\phi|)^2 - (1 - |\phi|^2)(1 - |\rho|^2)}$$
$$= (1 + |\rho||\phi|) - (|\rho| + |\phi|) = (1 - |\phi|)(1 - |\rho|).$$

So for $\frac{\pi_1}{\pi_2} = 1$, Speiser's two bounds for the equipower case can be identified as the eigenvalue values at the two extreme ends of the permissible phase-dependent variable $\xi$-interval. This $\xi$-interval is on the constant phase-independent $\eta$ horizontal line of the isosceles region with all expressions calculated from the magnitudes of $\rho$ and $\phi$ only. For given $\eta$, the permissible $\xi$-interval attains its maximum width when the $\xi$-interval extends from the left- to the right-boundary parabola. The length of such maximum $\xi$-interval increases with decreasing $\eta$, i.e., when the baseline is approached. The bounds for the small eigenvalue may be loose when there is considerable variation of the order of magnitude of the small eigenvalue along the maximum $\xi$-interval.

### 3.6.2 For the General Power Ratio $\frac{\pi_1}{\pi_2}$ Case

For the general $\frac{\pi_1}{\pi_2}$ case, Speiser's expression can be similarly arranged as

$$(1 - |\phi|)\frac{1}{2}(\frac{\pi_1}{\pi_2} + 1)\left[1 - \sqrt{1 - \frac{4(\frac{\pi_1}{\pi_2})(1 - |\rho|^2)}{(\frac{\pi_1}{\pi_2} + 1)^2}}\right] \leq \lambda_2$$

$$\leq \frac{1}{2}(\frac{\pi_1}{\pi_2} + 1)\left\{1 - |\phi|\sqrt{1 - \frac{4(\frac{\pi_1}{\pi_2})(1 - |\rho|^2)}{(\frac{\pi_1}{\pi_2} + 1)^2}} - \left|\,|\phi| - \sqrt{1 - \frac{4(\frac{\pi_1}{\pi_2})(1 - |\rho|^2)}{(\frac{\pi_1}{\pi_2} + 1)^2}}\,\right|\right\}$$

Note these bound expressions involve only the absolute magnitude of the two phasors on the two unit-disks, i.e., only the radius but not the argument of the phasors. They are not explicitly dependent on the other parameter

$$\xi = \text{Re}(\rho\phi^*) = |\rho||\phi|\cos(\arg\rho - \arg\phi),$$

47

which is the inner product of these two phasors and consequently contains relative phase information between the two. But as before, for given $|\rho|$ and $|\phi|$, we have $\eta = (1 - |\phi|^2)(1 - |\rho|^2)$ and $|\xi|_{\text{max}} = |\rho||\phi|$. Therefore, as in the preceding subsection for the equipower case $\frac{\pi_1}{\pi_2} = 1$, we can draw the conclusion a priori that these bound expressions at best bound the lower part of the truncated hyperbola in $\xi$ and $\lambda$ over the permissible phase-dependent variable $\xi$-interval corresponding to the given value of

$$\eta = (1 - |\phi|^2)(1 - |\rho|^2).$$

For given value of $\frac{\pi_1}{\pi_2}$, the exact eigenvalues depend on the two complex phasors on the unit-disks, $\rho$ and $\phi$, through the two derived bounded real numbers $\xi$ and $\eta$. In contrast, the two bounds' expressions involve the magnitude of the two phasors, i.e., two different real numbers. Therefore, it is much simpler to browse the hyperbolic slice plots to visualize the best non-explicitly $\xi$-dependent bounds one can possibly have than to analyze the particular bounds derived by Speiser. From our early characterization of the $\lambda$ surfaces, we know that the dependence of $\lambda$s on $\xi$ becomes more insignificant as $\frac{\pi_1}{\pi_2}$ gets large. We expect that such $\xi$-independent bounds perform better in this region. Naturally we must bear in mind that the original form of these bounds are applicable to the general multisource arrival scenario and they may serve some useful purpose there.

We have used plots to give some indication of the $\xi$-dependent nature of the eigenvalues. We can also give some analytical indication of the same phenomenon for the most important area. As the $\eta = 0$ baseline is where $\lambda_2 = 0$, we have more quantitative information about the $\xi$-dependent or $\xi$-independent nature of $\lambda_2$ in this neighborhood for given values of $\frac{\pi_1}{\pi_2}$ because of the following analytical characterization. Near $\eta = 0$ and at the three particular $\xi$ values, we have for $\frac{\pi_1}{\pi_2} = 1$

$$\lambda_2(-1,\eta) \approx \infty\eta, \quad \lambda_2(0,\eta) \approx \frac{\eta}{2}, \quad \lambda_2(1,\eta) \approx \frac{\eta}{4}.$$

This indicate the significant $\xi$-dependence of $\lambda_2$. Near $\eta = 0$ and for large $\frac{\pi_1}{\pi_2}$, we have instead

$$\lambda_2(\xi,\eta) \approx \eta,$$

i.e., essentially $\xi$-independent.

# Chapter 4

# Fractional Beamwidth Separation Between Two Plane Waves Impinging on a Uniform Line Array (ULA)

Even though we only assess those algorithms applicable to general sensor array configurations, we still need to understand the results for plane waves impinging on a ULA, especially those simulation results that could be expensive to duplicate for general arrays. After all, more than half of the theoretical and numerical development on ABF and high-resolution DF are specialized, occasionally unnecessarily, to ULA. Many ULA specific results can shed light on the general array as well.

Frequently in the direction-finding literature, the stress to a direction-finding scenario in the context of close arrivals is expressed in terms of the fractional beamwidth separating the two arrivals, with or without the number of elements of the ULA prominently specified. There seems to be the implicit assumption that the stress depends mainly on the fractional beamwidth which has already folded into it the information about the number of sensors, $N$, used in the array. In other words, the figures plotted against fractional beamwidth for a ULA using some specific number of half-wavelength-spaced elements are indicative of the behavior for another ULA using different number of elements. Therefore, it is useful to assess the validity of this assumption for the uncorrelated special case for ULA, as it is the easiest one analyzed. Here, we express the stress in terms of the smallest eigenvalue $\lambda_2 \propto \eta = 1 - |\phi|^2$, which is good for close arrivals and all $\frac{\pi_1}{\pi_2}$ values near the $\eta = 0$ baseline region, where $\phi$ is derived in the usual fashion.

## 4.1 Fractional Beamwidth Measurement for Arrival Separation $\theta_{frac\_bw}$

Let the elements' location of the ULA have the following coordinates,

$$[(x_n, y_n), n = 1, \cdots, N] \text{ with } x_n = (n-1)d, \ y_n = 0,$$

where $d$ is the uniform interelement spacing. Define as in [23, page 38] or [52, page 48] the reduced angular variable

$$\theta = \sin\alpha - \sin\alpha_0 = 2\cos\frac{1}{2}(\alpha + \alpha_0)\sin\frac{1}{2}(\alpha - \alpha_0),$$

where $\alpha$ and $\alpha_0$ represent the directions of two arrivals relative to broadside. Let $k$ be $2\pi/\text{wavelength}$, i.e., the wave number. The normalized inner product of the two steering vectors corresponding to the two directions of plane wave arrivals $\alpha$ and $\alpha_0$ is

$$
\begin{aligned}
\phi &= \frac{1}{N}(1 + e^{jkd\theta} + \cdots + e^{j(N-1)kd\theta}) = \frac{1}{N}\frac{e^{jNkd\theta} - 1}{e^{jkd\theta} - 1} \\
&= \frac{1}{N} e^{j\frac{1}{2}(N-1)kd\theta} \frac{\sin(\frac{1}{2}Nkd\theta)}{\sin(\frac{1}{2}kd\theta)}.
\end{aligned}
$$

In section 3.1, we listed the known property that the inner product of two steering vectors for plane waves impinging onto pairwise symmetric arrays is real. The above spatial correlation equation indicates that the phase term will disappear with the change of the coordinate origin from one end to the center of the ULA.

For a continuous line array, the standard beamwidth definitions are inferred from the first null of the radiation pattern in units of the reciprocal of the array aperture. From the above displayed equation, it is clear that for the discrete ULA, the length of the array aperture should be interpreted as $Nd$, not $(N-1)d$. For ULA, the *4_dB_down_bw_in_θ* beamwidth coincides with the standard beamwidth, see [22, eqns. 4.5,4.34,4.35] for example. However, the 4-dB down beamwidth definition can be readily extended to general arrays whereas that of the standard beamwidth cannot. For example, the log-periodic array does not have nulls in its radiation pattern. This is based on the equivalent Logarithmic Period Modulated (LPM) or Hyperbolic Frequency Modulated (HFM) waveform result [11] where the sidelobe magnitude square has a positive term in additional to the familiar sinc-square term. We will also relate the separation between two close arrivals in terms of the fractional beamwidth for the mechanical directions of arrivals $\alpha$ and $\alpha_0$ to that in terms of the electrical phase angle $\theta$.

The 4-dB down beamwidth in the electrical phase angle, $kd\theta$, from element to element along the
ULA (*4_dB_down_bw_in_θ*) is defined as the reciprocal of the array aperture by [5, eqns. 6-34,11-12,11-14]

$$4\_dB\_down\_bw\_in\_\theta = \left[\frac{Nd}{\text{wavelength}}\right]^{-1} = \frac{2\pi}{Nkd},$$

where $k = 2\pi/\text{wavelength}$. The corresponding 4-dB down beamwidth relative to the two directions of arrivals $\alpha$ and $\alpha_0$ (*4_dB_down_bw_rel_to_($\alpha + \alpha_0$)/2*) is defined as the reciprocal of the effective array aperture by

$$
\begin{aligned}
4\_dB\_down\_bw\_rel\_to\_(\alpha + \alpha_0)/2 &= \left[\frac{Nd\cos\frac{1}{2}(\alpha + \alpha_0)}{\text{wavelength}}\right]^{-1} \\
&= \frac{2\pi}{Nkd\cos\frac{1}{2}(\alpha + \alpha_0)}.
\end{aligned}
$$

The separation between two arrivals can be expressed as $\theta_{frac\_bw}$ in terms of fractional beamwidth by

$$\theta_{frac\_bw} = \frac{\theta}{4\_dB\_down\_bw\_in\_\theta} = \frac{Nkd\theta}{2\pi} = \frac{Nd\theta}{\text{wavelength}},$$

50

or equivalently

$$kd\theta = \frac{2\pi}{N}\,\theta_{frac\_bw}.$$

The terminology makes sense as for close arrivals

$$\frac{\alpha - \alpha_0}{4\_dB\_down\_bw\_rel\_to\_(\alpha + \alpha_0)/2} \approx \frac{2\sin\frac{1}{2}(\alpha - \alpha_0)}{\left[\frac{Nd\cos\frac{1}{2}(\alpha+\alpha_0)}{\text{wavelength}}\right]^{-1}}$$

$$= 2\sin\frac{1}{2}(\alpha - \alpha_0)\cos\frac{1}{2}(\alpha + \alpha_0)\left[\frac{Nd}{\text{wavelength}}\right]$$

$$= (\sin\alpha - \sin\alpha_0)\left[\frac{Nd}{\text{wavelength}}\right]$$

$$= \theta \times \text{aperture\_in\_units\_of\_wavelength} = \theta_{frac\_bw}.$$

The above development is similar to that reported by Evans, Johnson, and Sun [15].

The normalized inner product of the two steering vectors corresponding to the two directions of arrivals $\alpha$ and $\alpha_0$ is

$$\phi = \frac{1}{N}\,e^{j\pi\frac{N-1}{N}\theta_{frac\_bw}}\frac{\sin(\pi\theta_{frac\_bw})}{\sin(\frac{1}{N}\pi\theta_{frac\_bw})}.$$

Therefore, we have

$$|\phi| = \frac{1}{N}\left|\frac{\sin(\pi\theta_{frac\_bw})}{\sin(\frac{1}{N}\pi\theta_{frac\_bw})}\right|.$$

For closely spaced arrivals, the above equation can be approximated by

$$|\phi| \approx \frac{1 - \frac{1}{6}\left[\pi\theta_{frac\_bw}\right]^2 + \cdots}{1 - \frac{1}{6}\left[\frac{1}{N}\pi\theta_{frac\_bw}\right]^2 + \cdots} \approx 1 - \frac{1}{6}(1 - \frac{1}{N^2})(\pi\theta_{frac\_bw})^2.$$

For very close arrivals, $\phi \approx 1$, i.e., i' location on the unit-disk is on the circumference. The horizontal axis has the following inter, etation now: $\xi \approx \text{Re}(\rho) = |\rho|\cos(\arg\rho)$.

## 4.2 The Smaller Eigenvalue $\lambda_2$'s Negligible Dependence on the Number of Elements N after Using $\theta_{frac\_bw}$ for the Equipower Uncorrelated Case

For uncorrelated and equal strength arrivals, the only stress to the direction-finding scenario is the angular separation between the arrivals, therefore

$$\lambda_2 = 1 - |\phi| = 1 - \frac{1}{N}\left|\frac{\sin(\pi\theta_{frac\_bw})}{\sin(\frac{1}{N}\pi\theta_{frac\_bw})}\right|.$$

For this case, a discussion of the smaller eigenvalue $\lambda_2$ directly results from that for the magnitude $|\phi|$ of the generalized cosine of the steering vectors of the two arrivals. An approximation for $\lambda_2$ for closely spaced arrivals can also be obtained via

$$\lambda_2 \approx \frac{\eta}{2} = \frac{1 - |\phi|^2}{2} = \frac{1}{2} - \frac{1}{2}\left[\frac{1}{N}\frac{\sin(\pi\theta_{frac\_bw})}{\sin(\frac{1}{N}\pi\theta_{frac\_bw})}\right]^2 \approx \frac{1}{6}(1 - \frac{1}{N^2})(\pi\theta_{frac\_bw})^2.$$

51

All these expressions for $\phi$ and $\eta$ depend on both $\theta_{frac\_bw}$ and $N$.

For small $\theta_{frac\_bw}$ associated with the stressing scenario of close arrivals, say $\theta_{frac\_bw} \leq 0.1$, the last equation shows that $\lambda_2$ increases quadratically with $\theta_{frac\_bw}$ and increases with increasing $N$. See figure 4.1. The dependence on N is noticeable only for small $N$ but becomes rapidly negligible for large $N$. See figure 4.2. The last equation indicates that the variation of $\theta_{frac\_bw}$ for $N \geq 10$ is only 1%. The $\lambda_2$ value at $N = 3$ is 90% of that at $N = \infty$. Therefore, one can safely ignore the $\lambda_2$'s additional dependence on N.

As $\theta_{frac\_bw}$ increases, say $0.1 \leq \theta_{frac\_bw} \leq 1.0$, the unbounded parabola approximation is obviously less valid as the $(1 - sinc^2)$-like function is bounded above by 1. We note that the stress in terms of $\lambda_2$ is among the lowest possible near $\theta_{frac\_bw} = 1.0$. When the two arrivals are separated by exact multiples of the Raleigh beamwidth, the inner product between the two steering vectors is zero, i.e., the two steering vectors are orthogonal. The $\lambda_2$'s additional dependence on N after using $\theta_{frac\_bw}$ is even smaller than the previous $\theta_{frac\_bw} \leq 0.1$ case. See figures 4.3 and 4.4. We note that in both figures, $\lambda_2 = 1$ at $\theta_{frac\_bw} = 1.0$ regardless of the values of $N$, as it should.

If we continue the plot beyond $\theta_{frac\_bw} = 1.0$, the ripple phenomena of the $\lambda_2$ versus $\theta_{frac\_bw}$ will show up prominently as indicated in figures 4.5 and 4.6. This is associated with the sidelobes of ULA, which depends on both $\theta_{frac\_bw}$ and $N$. That is, the $(\xi, \eta)$ will stay near $(0, 1)$, the apex of the isosceles-right-triangle-like region. The stress to such a direction-finding scenario in terms of $\lambda_2$ can only come from the two arrivals' strength ratio $\pi_1/\pi_2$ which will show up in the $\lambda_1/\lambda_2$ ratio and/or source amplitude correlation $\rho$ such as from multipath. Overlooking the ripples, the $(1 - sinc^2)$-like function gets closer to 1 as $\theta_{frac\_bw}$ increases. Therefore, the dependence on $N$ is not significant either. We also notice the grating lobe phenomena such as at $(\theta_{frac\_bw}, N) = (3,3), (6,3), (9,3), (6,6), (9,9)$ in figures 4.7 and 4.8. See [52] for explanations. In figure 4.8, we have chosen to plot the $\lambda_2 = 1 - |\phi|$ slices vs N at $\theta_{frac\_bw} = 0.5 : 1 : 9.5$, which correspond to the sidelobes of the CBF.

However, because of the ripple effect, the smaller eigenvalue may even decrease when more sensors are used while everything else is the same. This will cause some undesirable phenomena when noise is brought in and a unit-weighting signal space method is used. For moderate SNRs, the error variance of each eigenvector calculated from the sample data covariance matrix is roughly proportional to that particular eigenvalue. Ottersten, in fact, produced some interesting asymptotic results illustrating the detrimental effect to the DOA parameter standard deviation when plotted as a function of the number of sensor elements for the unity-weighting algorithm for ULA[38, pages 68-69]. As he fixed the mechanical angle separation between the two arrivals, the fractional beamwidth changes as the number of sensor elements varies. The $(\theta_{frac\_bw}, N)$ points trace out a curve in the base plane of the mesh and contour plots in figures 4.5 and 4.6.

In conclusion, the fractional beamwidth notion is a useful concept for assessing the stress to a direction-finding scenario in terms of the normalized smaller eigenvalue $\lambda_2$. It consolidates the effects of arrival separation, sensor element spacing, wavelength, and number of sensor elements into one entity.

Figure 4.1: $\lambda_2 = 1 - |\phi|$ slices vs $\theta_{frac\_bw} \leq 0.1$ at N=3,6,9,12,15,18,21 for ULA.
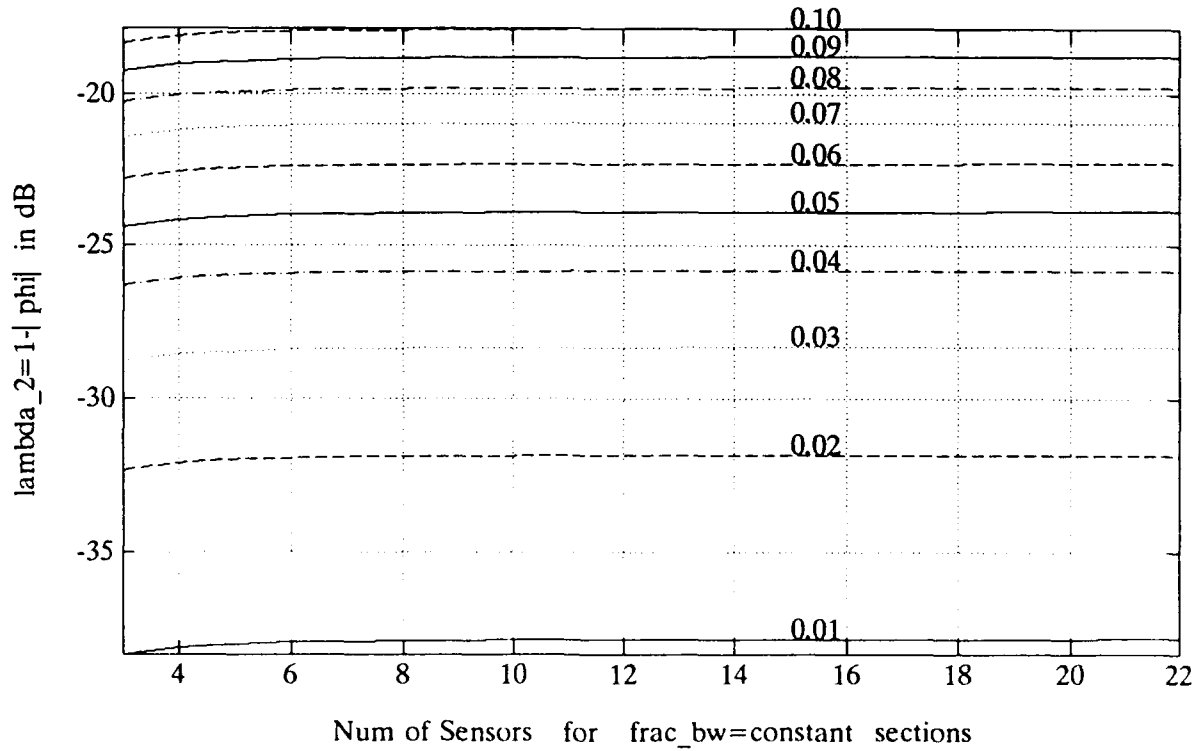


Figure 4.2: $\lambda_2 = 1 - |\phi|$ slices vs N at $\theta_{frac\_bw} = 0.01 : 0.01 : 0.10$ for ULA.

Figure 4.3: $\lambda_2 = 1 - |\phi|$ slices vs $0.1 \leq \theta_{frac\_bw} \leq 1.0$ at N=3,6,9,12,15,18,21 for ULA.



Figure 4.4: $\lambda_2 = 1 - |\phi|$ slices vs N at $\theta_{frac\_bw} = 0.1 : 0.1 : 1.0$ for ULA.

Figure 4.5: Mesh plot of $\lambda_2 = 1 - |\phi|$ over $1 \leq \theta_{frac\_bw} \leq 10$ and N=3:1:22 for ULA.



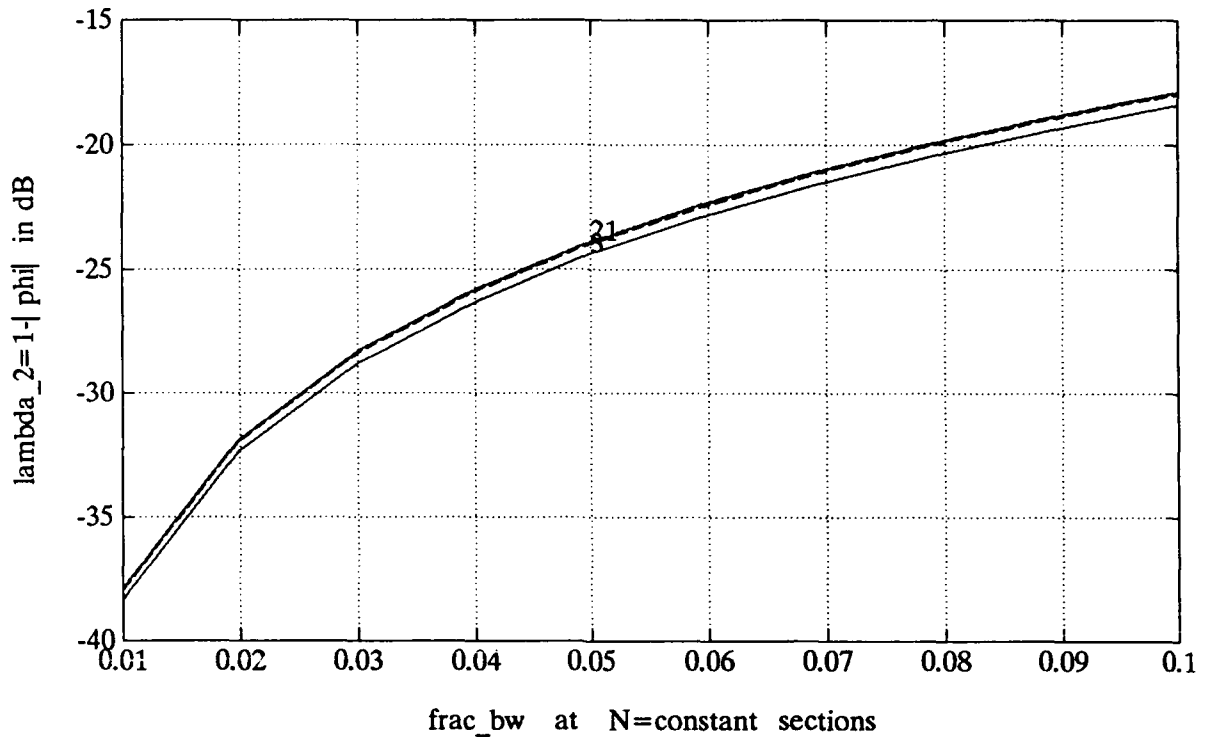Figure 4.6: Contour plot of $\lambda_2 = 1 - |\phi|$ over $1 \leq \theta_{frac\_bw} \leq 10$ and N=3:1:22 for ULA.

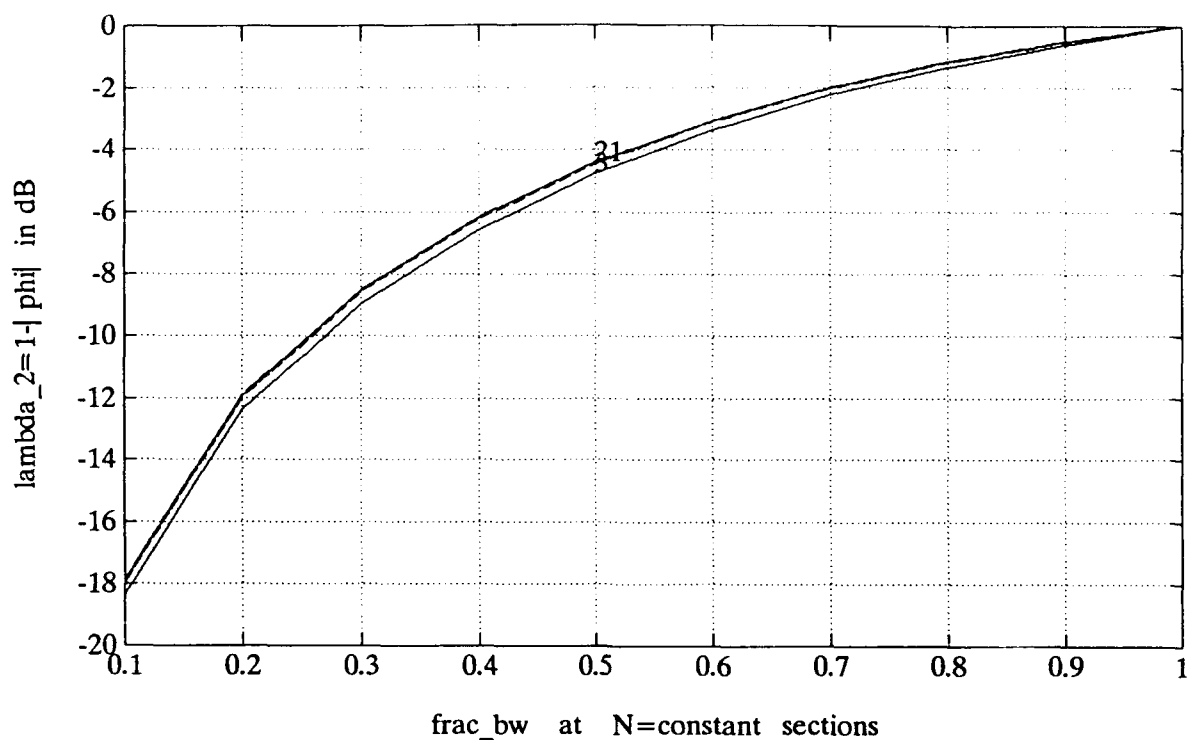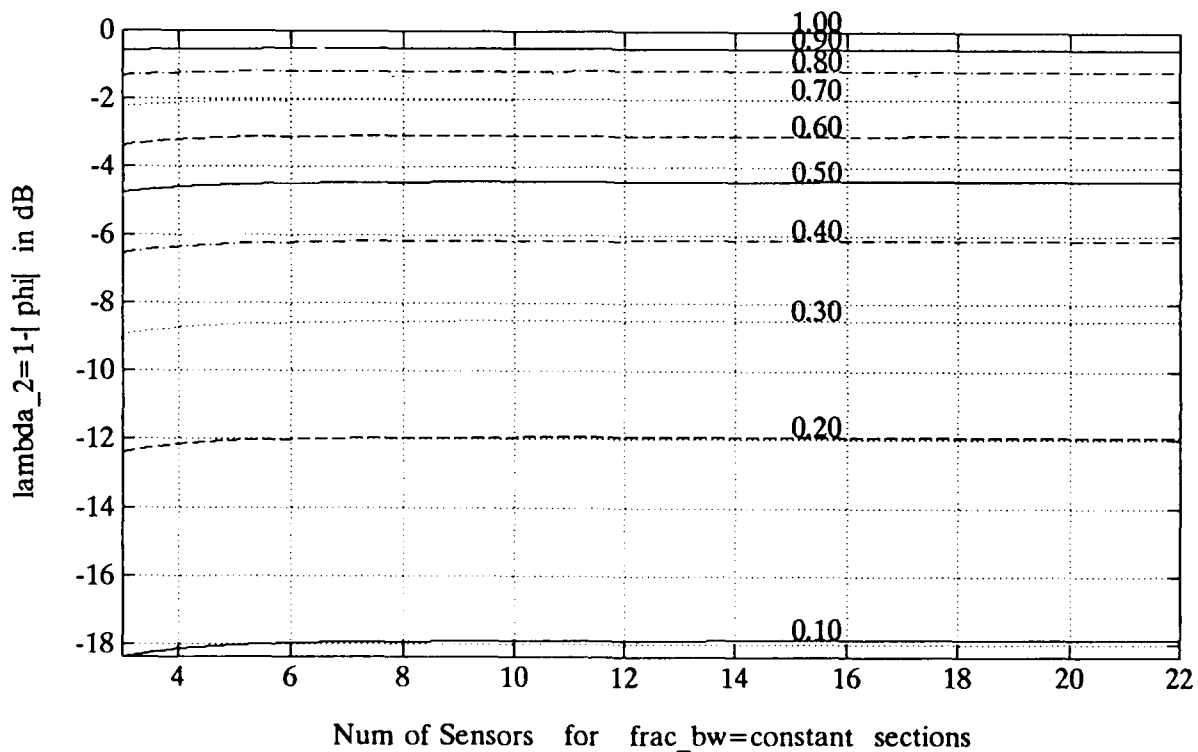Figure 4.7: $\lambda_2 = 1 - |\phi|$ slices vs $1 \leq \theta_{frac\_bw} \leq 10$ at N=3,6,9,12,15,18,21 for ULA.



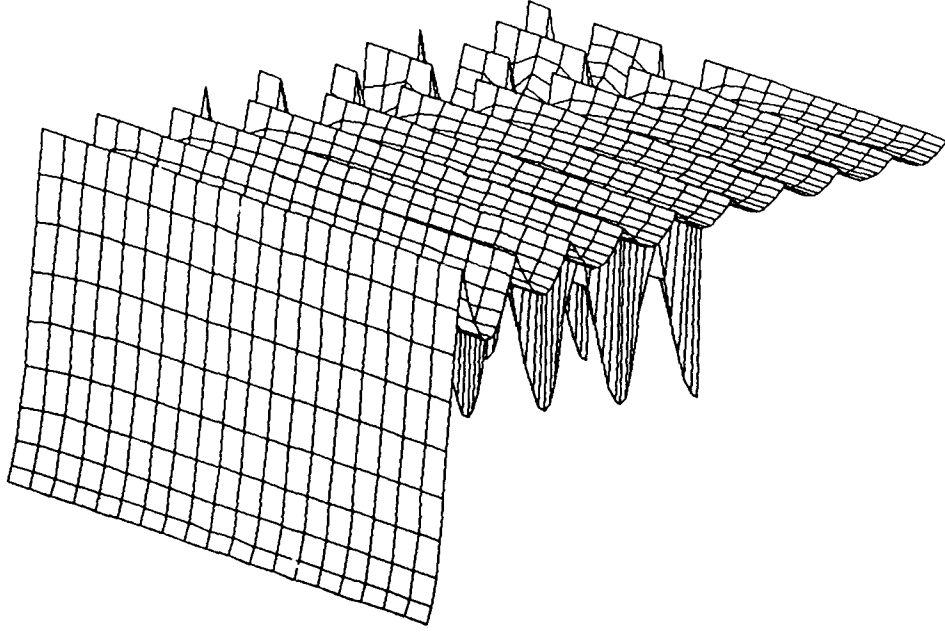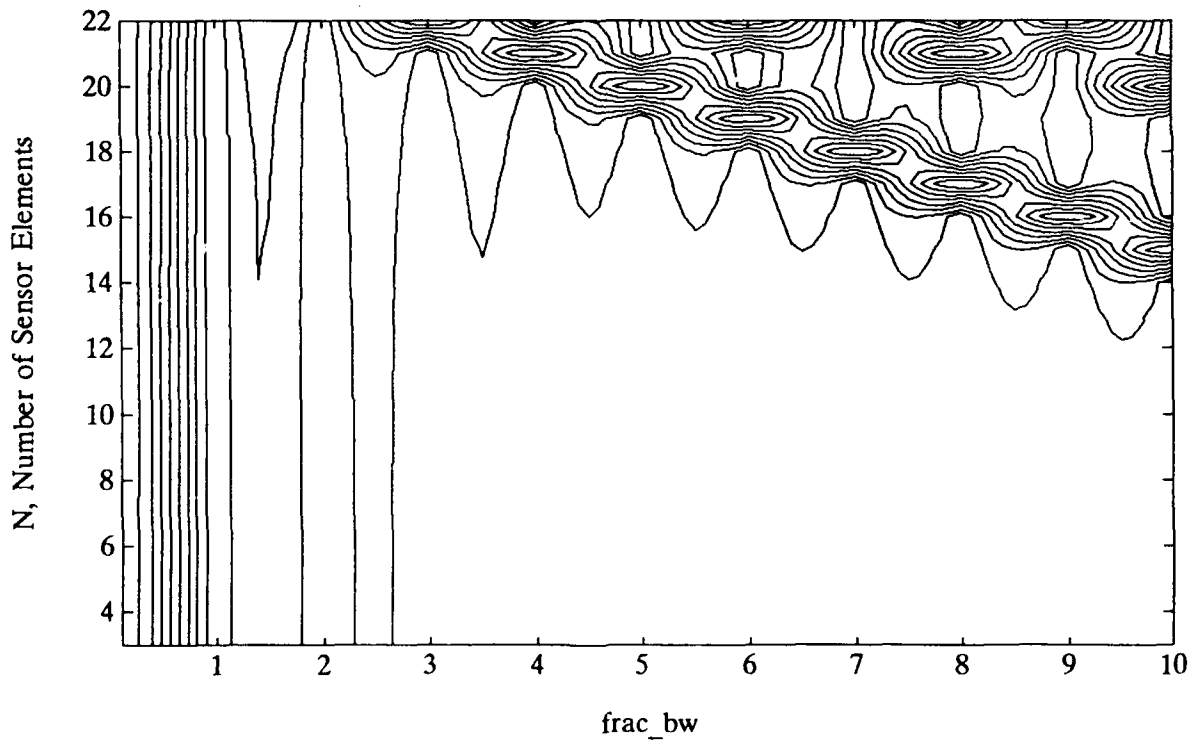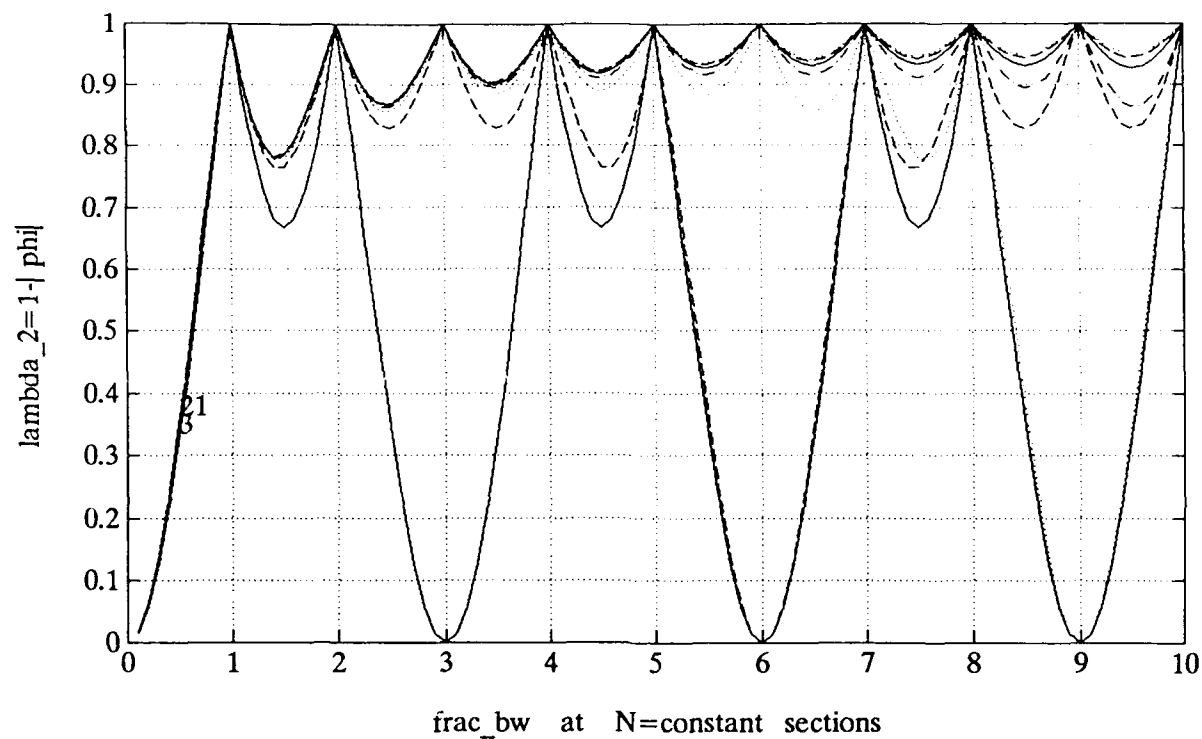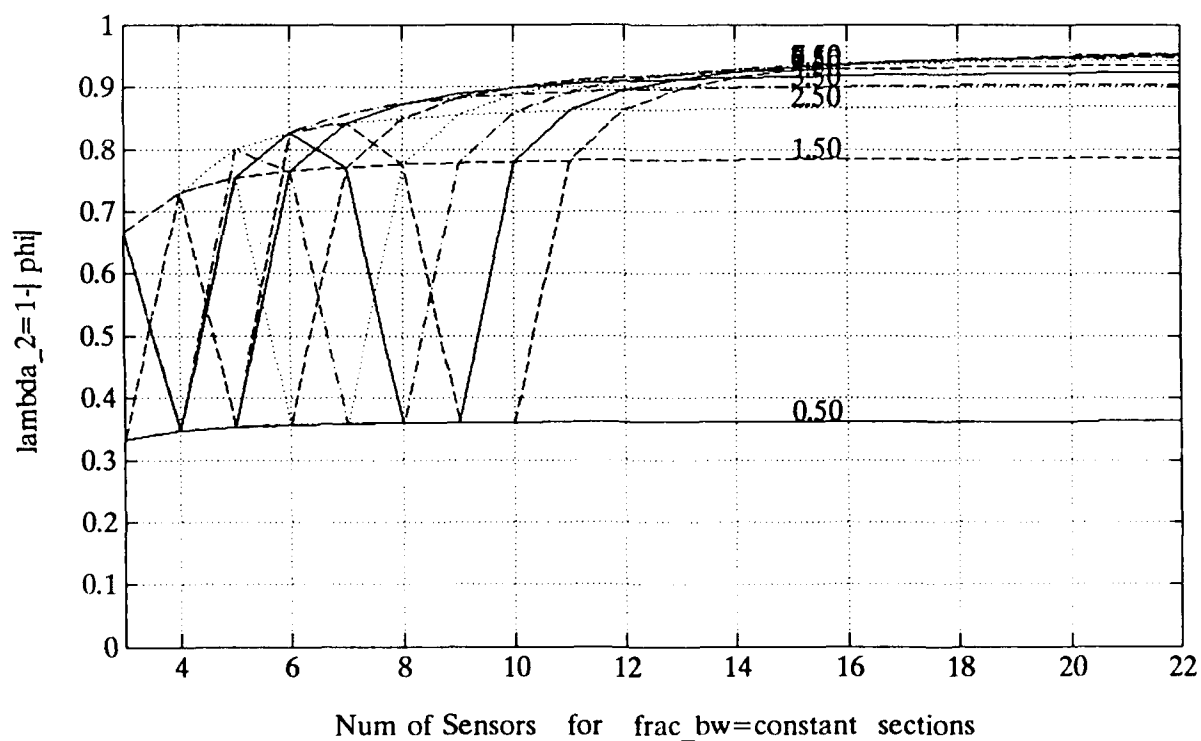Figure 4.8: $\lambda_2 = 1 - |\phi|$ slices vs N at $\theta_{frac\_bw} = 0.5 : 1 : 9.5$ for ULA.

# Chapter 5

# Plots of Signal Eigenvalues and their Ratio in dB Scale

The plots of the same information, or function, using direct scale and dB scale in the vertical axis have their individual merits. The direct-scale versions show the parabolic and hyperbolic sections as well as the straight line contours in their natural coordinates as derived from the analytical studies. Versions using the dB scale better illustrate the multiplicative dependence of the eigenvalues on some of the three independent parameters. In addition, the effect of the smallest dominant eigenvalue is relative to the threshold setting, which is frequently expressed in dB scale; the condition number can be exhibited more compactly in this way.

While the parabola sections are all translation copies of each other for given $\frac{\pi_1}{\pi_2}$ values in the direct-scale coordinates, one cannot recognize such relations from the dB-scale plots. For example, the vertical intervals (0,9) and (1,10) are translation copies of each other and can be recognized as such easily in the direct-scale plot. But their images in the dB scale are qualitatively different because of the nonlinear nature of the logarithmic function, especially near zero, which is so important for our study.

In section 5.1, we first display the slices of the two signal eigenvalues $\lambda_1$ and $\lambda_2$ in dB along constant phase-independent variable $\eta$ and along constant phase-dependent variable $\xi$ for power ratio $\frac{\pi_1}{\pi_2} = 0, 10, 20, 30$ dB. Next, their ratio, which is the difference in dB of the large and small signal eigenvalues, will be examined. In sections 5.2 and 5.3, we will find that the variation of signal eigenvalue ratio $\frac{\lambda_1}{\lambda_2}$ across the phase-dependent variable $\xi$ is not significant. We focus attention to the condition number's behavior over the vertical axis $\xi = 0$ of the isosceles region in section 5.4.

While the parabola and hyperbola characterization described in sections 3.4 and 3.5 pertains only to linear-scale plots, we retain for convenience such terminology even for those functional representation in the semilog coordinates used in this chapter.

As $\eta$ approaches 0, the small eigenvalue $\lambda_2$ and the eigenvalue ratio $\frac{\lambda_1}{\lambda_2}$ tend toward – and + $\infty$ dB respectively. Similarly, as $\eta$ approaches 0 for the equipower case, $\frac{\pi_1}{\pi_2} = 0$ dB, both the upper $\lambda_1$ and lower $\lambda_2$ hyperbolas tend toward their asymptotes intersecting at $-\infty$ dB. Because we cannot display $\pm\infty$ dB, we choose to stop at a small value of $\eta = -13$ dB, which corresponds to spatially orthogonal arrivals with temporal correlation of 97.5%, or temporally uncorrelated arrivals with a $\frac{1}{4}$ fractional beamwidth spacing for a ULA.

## 5.1 Slices of Signal Eigenvalues $\lambda_1$ and $\lambda_2$ in dB along Constant Phase-Independent Variable $\eta$ and along Constant Phase-Dependent Variable $\xi$ for Power Ratio $\frac{\pi_1}{\pi_2} = 0, 10, 20, 30$ dB

We plot the two signal eigenvalues $\lambda_1$ and $\lambda_2$ as functions of the phase-dependent variable $\xi$ and the phase-independent variable $\eta$ for four given power ratio $\frac{\pi_1}{\pi_2}$s.

- $\lambda_1$ And $\lambda_2$ At $\xi = -0.5, -0.25, 0, +0.25, +0.5$ For Four $\frac{\pi_1}{\pi_2}$ in figures 5.1, 5.2, 5.3, and 5.4.

- $\lambda_1$ And $\lambda_2$ At $\eta = 0.05, 0.25, 0.50, 0.75, 1.00$ For Four $\frac{\pi_1}{\pi_2}$ in figures 5.5, 5.6, 5.7, and 5.8.

For $\frac{\pi_1}{\pi_2} = 0$ dB, the upper and lower sheets of hyperbolas and parabolas, the latter with negative $\xi$, are all contiguous. They do not appear so only because of the coarse grid systems we used in making these plots, i.e., the left boundary curve of the isosceles region does not fall on the grid points. We mentioned at the beginning of this chapter that it is not possible to display the asymptotes simultaneously because they intersect at $-\infty$ dB. We note that straight lines in the linear-scale plot become curved in the semilog plot. Over the apex of the isosceles triangle both $\lambda_1$ and $\lambda_2$ show the common 0-dB value as they should, in both hyperbolic and parabolic slice plots.

When $\frac{\pi_1}{\pi_2}$ increases from 0 dB, over the apex of the isosceles triangle $\lambda_1$ and $\lambda_2$ are separated farther and farther duplicating this increase. Because of the normalization convention adopted for the eigenvalues with respect to the sensor level signal power of the weaker source in section 3.1, over the apex of the isosceles triangle $\lambda_2$ is always at 0 dB. The large eigenvalue $\lambda_1$ curves are bundled closer in both directions of the phase-independent variable $\eta$ and the phase-dependent variable $\xi$. The variation of the small eigenvalue $\lambda_2$ appears more and more only in the phase-independent variable $\eta$. As the eigenvalue ratio in dB is the difference between the large and the small eigenvalues in dB, the variation in the ratio will be essentially from that of the small eigenvalue in the phase-independent variable $\eta$, as will be seen from the next three sections.

Figure 5.1: $\lambda_1$ and $\lambda_2$ in dB vs $\eta$ at $\xi = -0.5, -0.25, 0, +0.25, +0.5$ for $\frac{\pi_1}{\pi_2} = 0$ dB.



Figure 5.2: $\lambda_1$ and $\lambda_2$ in dB vs $\eta$ at $\xi = -0.5, -0.25, 0, +0.25, +0.5$ for $\frac{\pi_1}{\pi_2} = 10$ dB.

Figure 5.3: $\lambda_1$ and $\lambda_2$ in dB vs $\eta$ at $\xi = -0.5, -0.25, 0, +0.25, +0.5$ for $\frac{\pi_1}{\pi_2} = 20$ dB.



Figure 5.4: $\lambda_1$ and $\lambda_2$ in dB vs $\eta$ at $\xi = -0.5, -0.25, 0, +0.25, +0.5$ for $\frac{\pi_1}{\pi_2} = 30$ dB.

Figure 5.5: $\lambda_1$ and $\lambda_2$ in dB vs $\xi$ at $\eta = 0.05, 0.25, 0.50, 0.75, 1.00$ for $\frac{\pi_1}{\pi_2} = 0$ dB.


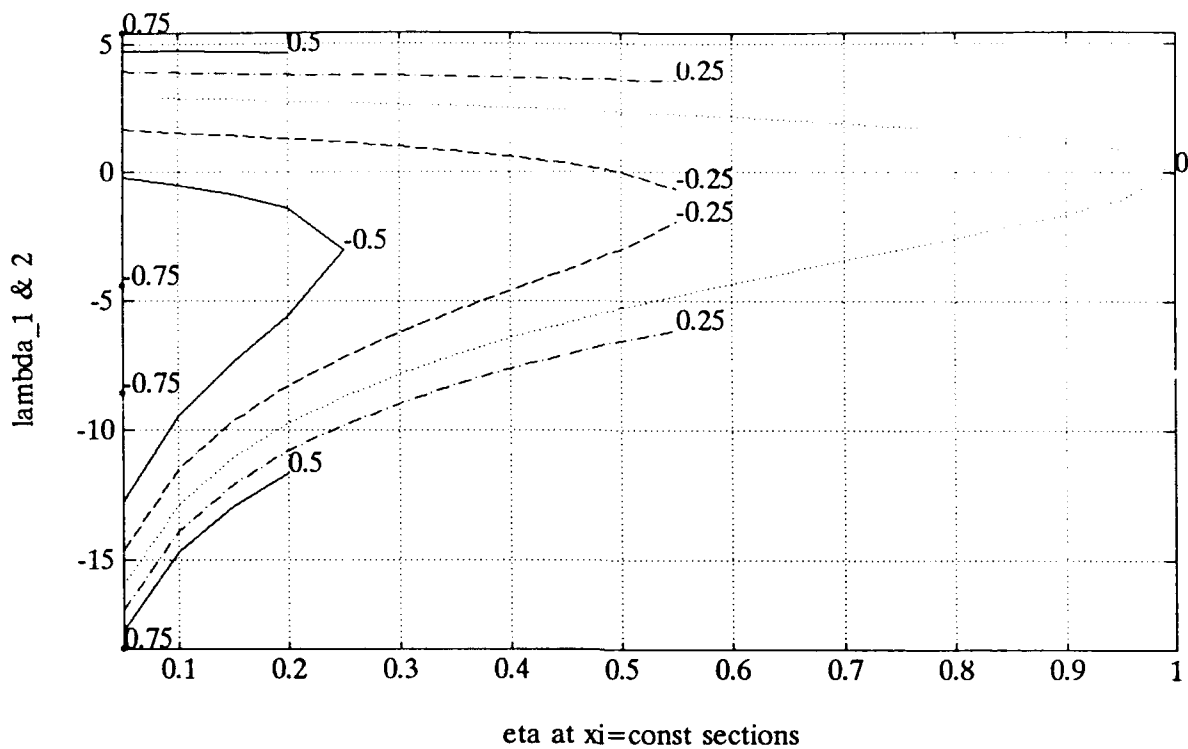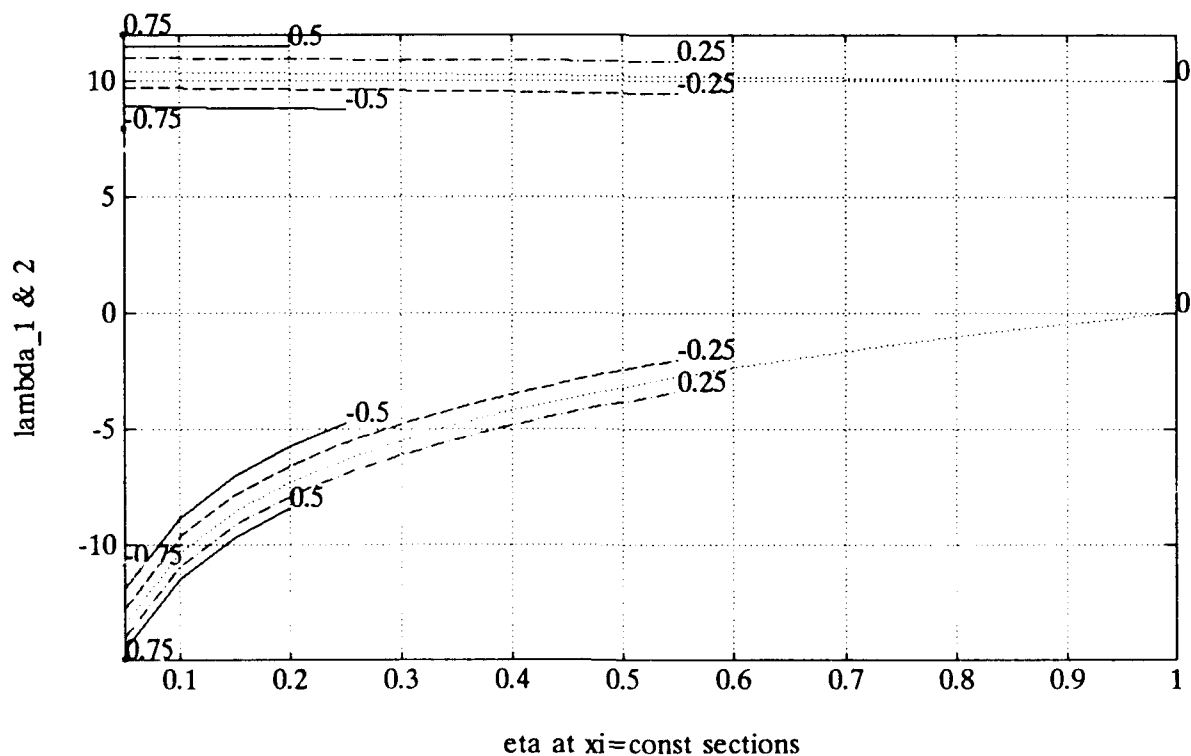
Figure 5.6: $\lambda_1$ and $\lambda_2$ in dB vs $\xi$ at $\eta = 0.05, 0.25, 0.50, 0.75, 1.00$ for $\frac{\pi_1}{\pi_2} = 10$ dB.
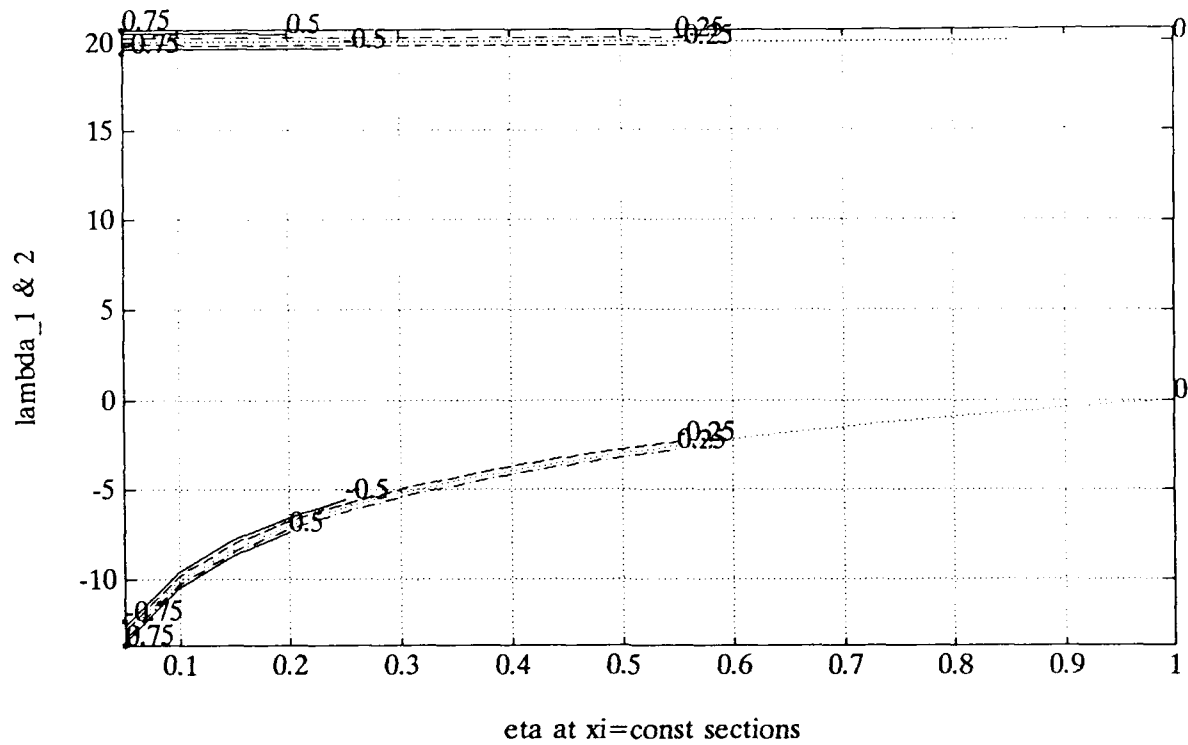
Figure 5.7: $\lambda_1$ and $\lambda_2$ in dB vs $\xi$ at $\eta = 0.05, 0.25, 0.50, 0.75, 1.00$ for $\frac{\pi_1}{\pi_2} = 20$ dB.
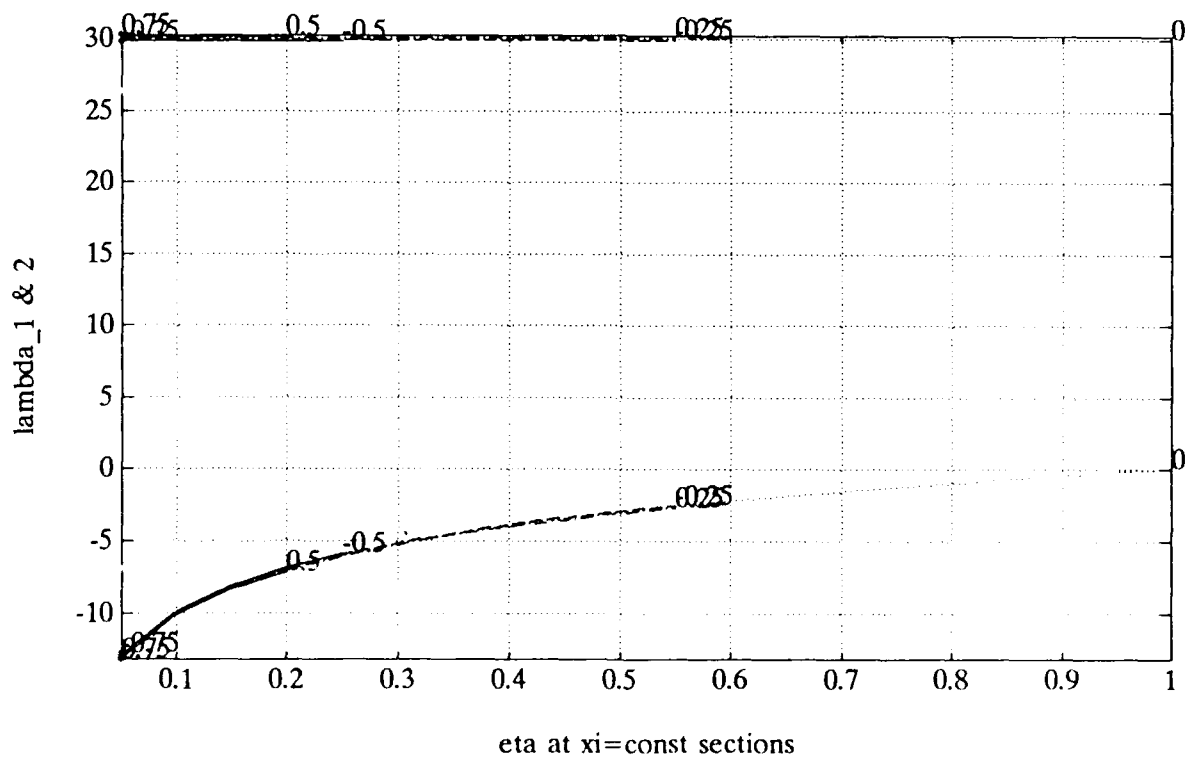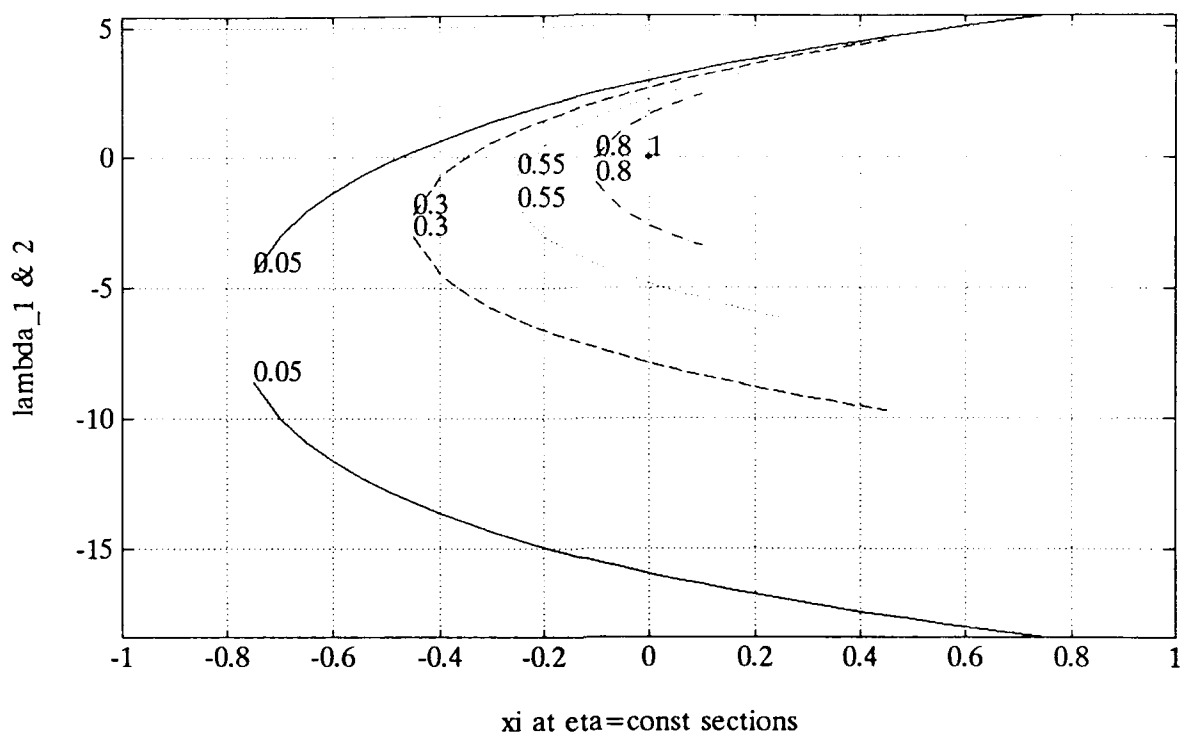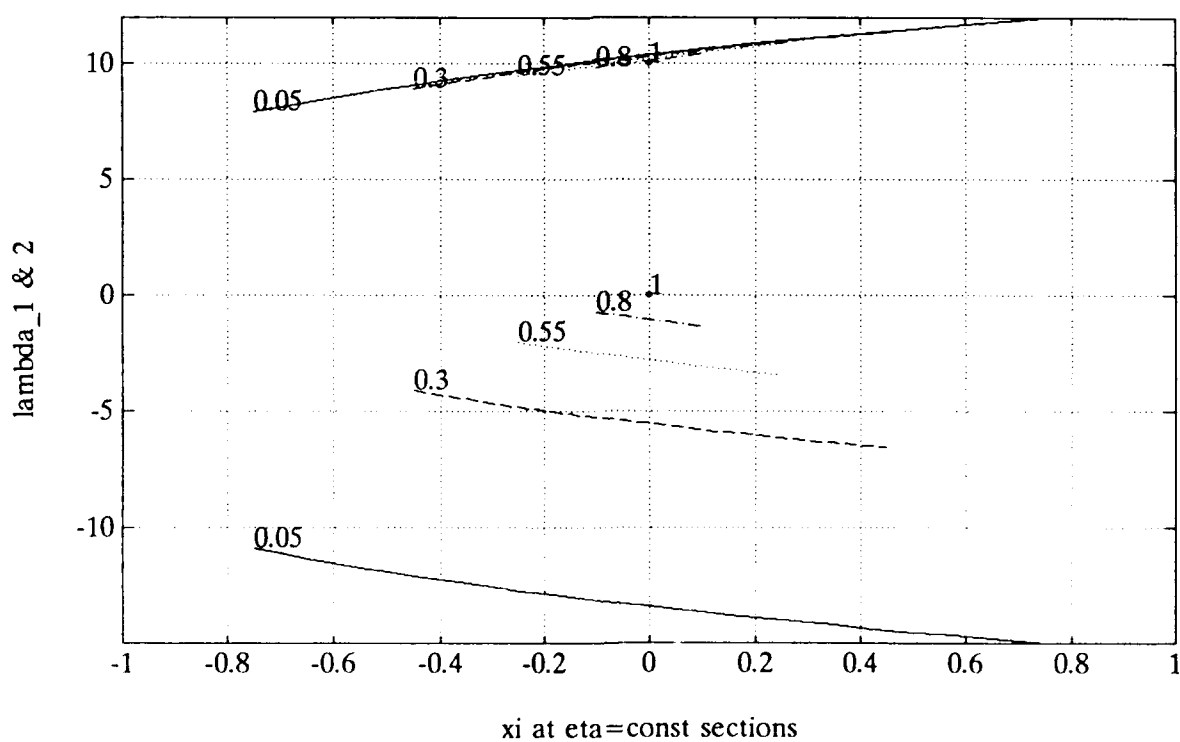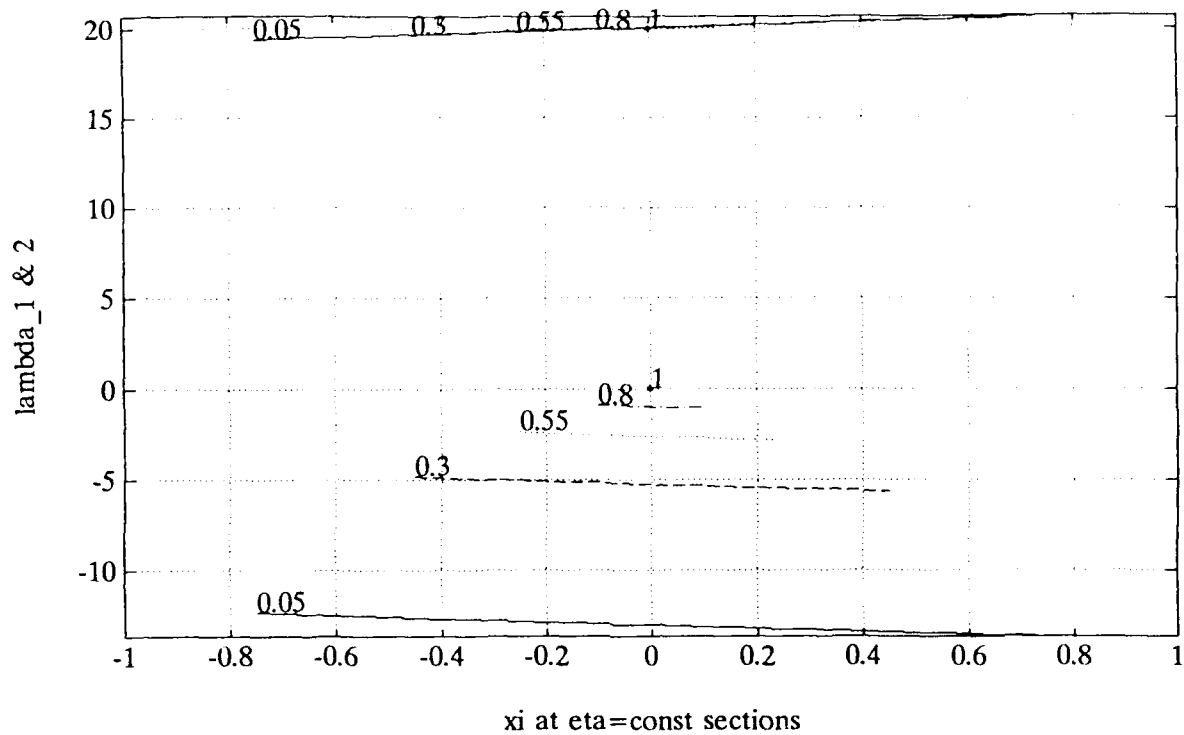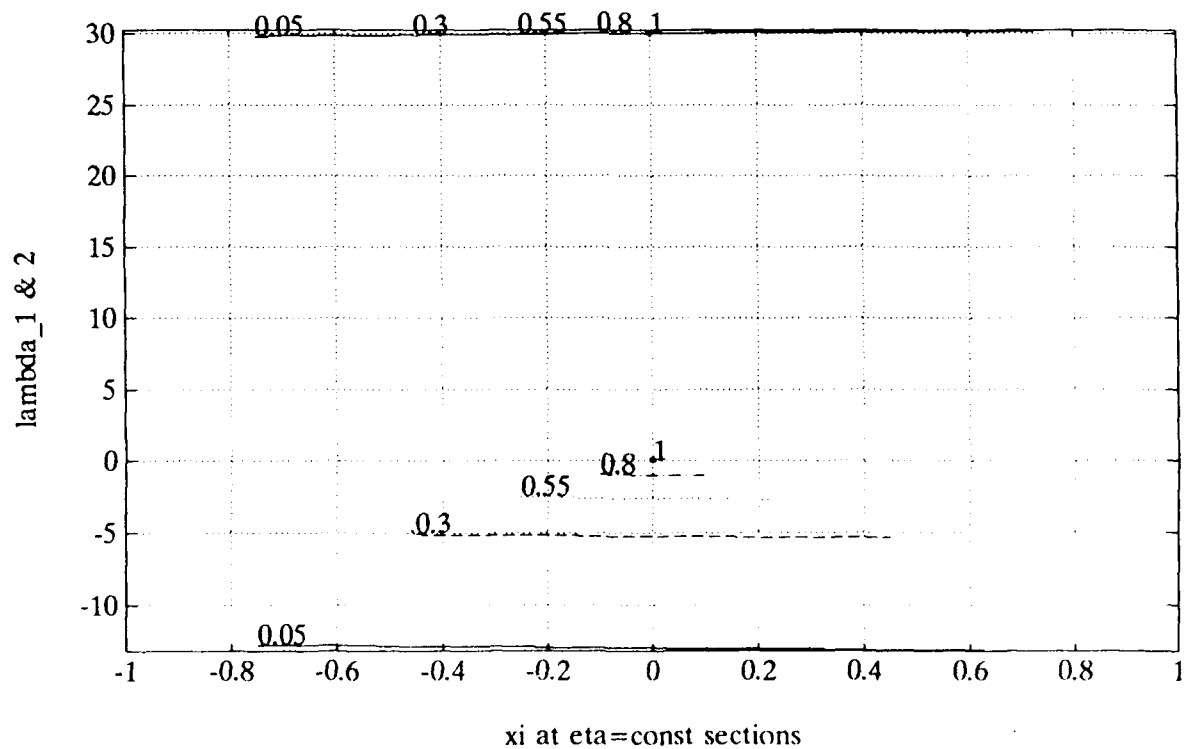


Figure 5.8: $\lambda_1$ and $\lambda_2$ in dB vs $\xi$ at $\eta = 0.05, 0.25, 0.50, 0.75, 1.00$ for $\frac{\pi_1}{\pi_2} = 30$ dB.

## 5.2 Four Sets of Signal Eigenvalue Ratio Plots for Power Ratio $\frac{\pi_1}{\pi_2} = 0, 10, 20, 30$ dB

We provide, for each of the four given power ratio $\frac{\pi_1}{\pi_2}$, mesh and contour plots of signal eigenvalue ratio $\frac{\lambda_1}{\lambda_2}$ as function of the phase-dependent variable $\xi$ and the phase-independent variable $\eta$ over the rectangular grid $[-1:1:0.05] \times [0.05:1:0.05]$, next slice plots along constant phase-dependent variable $\xi$ and then along constant phase-independent variable $\eta$. The vector $[-1:1:0.05]$ contains the numbers from $-1$ to $1$ with $0.05$ as increment in $\xi$. The vector $[0.05:1:0.05]$ contains the numbers from $0.05$ to $1$ with $0.05$ as increment in $\eta$.

- Mesh and contour plots of $\frac{\lambda_1}{\lambda_2}$ in dB as function of $\xi$ and $\eta$ in figures 5.9, 5.11, 5.13, and 5.15, and in figures 5.10, 5.12, 5.14, and 5.16 respectively.

- Slices of $\frac{\lambda_1}{\lambda_2}$ in dB at $\xi = -0.5, -0.25, 0, +0.25, +0.5$ for $\frac{\pi_1}{\pi_2} =$ dB in figures 5.17, 5.19, 5.21, and 5.23.

- Slices of $\frac{\lambda_1}{\lambda_2}$ in dB at $\eta$=0.05,0.25,0.50,0.75,1.00 for $\frac{\pi_1}{\pi_2} =$ dB in figures 5.18, 5.20, 5.22, and 5.24.

For $\frac{\pi_1}{\pi_2} = 0$ dB, the mesh plot of the signal eigenvalue ratio $\frac{\lambda_1}{\lambda_2}$ in figure 5.9 indicates that the ratio over the left boundary curve of the isosceles region is 0 dB, as it should be. We expect the slices of the eigenvalue ratio $\frac{\lambda_1}{\lambda_2}$ surface for negative constant $\xi$, phase-dependent variable, in figure 5.17, and for all constant $\eta$, phase-independent variable, in figure 5.18, to intersect the 0-dB abscissa axis. Again, they do not appear to be so only because of the coarse grid systems used in making these plots, i.e., the left boundary curve of the isosceles region does not fall on the grid points.

We notice from these two slice plots, figures 5.17 and 5.18, that the eigenvalue ratio $\frac{\lambda_1}{\lambda_2}$ tends toward $\infty$ dB as $\eta$ approaches 0. This illustrates the $\infty$ discontinuity of the eigenvalue ratio $\frac{\lambda_1}{\lambda_2}$ at the lower left corner of the isosceles region. The limit approaching from the baseline of the isosceles region is $\infty$, while that approaching from the left boundary curve of the isosceles region is 0. Note at this corner, both signal eigenvalues $\lambda_1$ and $\lambda_2$ are zero ($-\infty$ dB) and their ratio is indeterminate. This may be related to the difficulty mentioned in subsection 2.3.3. We have discussed in subsection 3.4.4 that the contours of the eigenvalue ratio $\frac{\lambda_1}{\lambda_2} = l$, in figure 5.12, are the same one-parameter family of parabolas introduced there with the conversion between the parabola parameter $\frac{\eta}{2(\xi+1)^2} = p$ and eigenvalue ratio $\frac{\lambda_1}{\lambda_2} = l$ as

$$p = \frac{2}{l+1} \text{ or } l = \frac{2 - p + \sqrt{4 - 4p}}{p}.$$

Because of the difficulty of displaying $\infty$ and discontinuity, the apparent absence of these at the left corner in figures 5.9, 5.17, and 5.18 should be interpreted with care.

When $\frac{\pi_1}{\pi_2}$ gets larger, as in figures 5.10, 5.12, 5.14, and 5.16, the contours get more and more horizontal, which means that the dependence of the signal eigenvalue ratio $\frac{\lambda_1}{\lambda_2}$ on the two parameters $\xi$ and $\eta$ will be mainly from the phase-independent variable $\eta$. In subsection 3.4.4, we found that the contours of the eigenvalue ratio $\frac{\lambda_1}{\lambda_2} = l$ form a one-parameter family of parabolas having their vertices colocated at $(\xi, \eta) = (-\frac{1}{2}(1 + \frac{\pi_1}{\pi_2})/\sqrt{\frac{\pi_1}{\pi_2}}, 0)$, see figures 5.10, 5.12, 5.14, and 5.16. Furthermore, in the 3-d $(\xi, \eta, \frac{\lambda_1}{\lambda_2})$ coordinates, these colocated vertices of the parabola

63

contour slices when projected onto the $(\xi, \eta)$ coordinate plane coincide on the shared $\xi$-axis with the intersection of the common asymptotes for the $\eta$ parameter family of hyperbola slices in $\lambda$ and $\xi$ for constant phase-independent variable $\eta$s when projected onto the $(\xi, \lambda)$ coordinate plane. These families of hyperbola slices are displayed in figures 3.6, 3.14, 3.16, and 3.18.

The comments at the end of section 5.1 that the variation in the ratio is essentially from that of the small eigenvalue in the phase-independent variable $\eta$ can be confirmed by comparing the ratio plots in figures 5.18, 5.20, 5.22, and 5.24 with the small eigenvalue plots figures 5.5, 5.6, 5.7, and 5.8.

From figures 5.9, 5.11, 5.13, and 5.15, one observes that the mesh surfaces are lifted away from the 0-dB plane and appear flatter and flatter when $\frac{\pi_1}{\pi_2}$ gets larger. This must be interpreted with care because of the inadequate display coverage with $\eta$ stopped at $-13$ dB and the perspective angle showing the surface at $\frac{\pi_1}{\pi_2} = 30$ dB flatter than it is. While there is much less curvature as compared to the equipower arrival $\frac{\pi_1}{\pi_2} = 0$ dB case, there remains considerable variation of the eigenvalue ratio $\frac{\lambda_1}{\lambda_2}$ along constant phase-independent variable $\eta$. These plots are produced by the PC-MATLAB software which auto-scales the data to fit a plotting area of given size. If a common absolute scale is used for all these mesh plots for power ratio $\frac{\pi_1}{\pi_2} = 0, 10, 20, 30$ dB, the last three mesh surfaces would appear more as translational copies of each other. This can be seen from examining its accompanying slice plots along constant phase-dependent variable $\xi$ and then along constant phase-independent variable $\eta$. There, the vertical scales are more comparable as the 0 dB reference is not included as in the mesh plots. These will be made more clear in section 5.4.

For all slice plots, we note that the apex of the isosceles region always occupies the lower right hand corner for the upper slice plots of constant phase-dependent variable $\xi$, as in figures 5.17, 5.19, 5.21, and 5.23, and the middle of the abscissa axis for the lower slice plots of constant phase-independent variable $\eta$ as in figures 5.18, 5.20, 5.22, and 5.24. At the apex, the signal eigenvalue ratio $\frac{\lambda_1}{\lambda_2}$ always equal to the power ratio $\frac{\pi_1}{\pi_2}$, as it should.

Figure 5.9: Mesh plot of $\frac{\lambda_1}{\lambda_2}$ in dB as function of $\xi$ and $\eta$ for $\frac{\pi_1}{\pi_2} = 0$ dB.
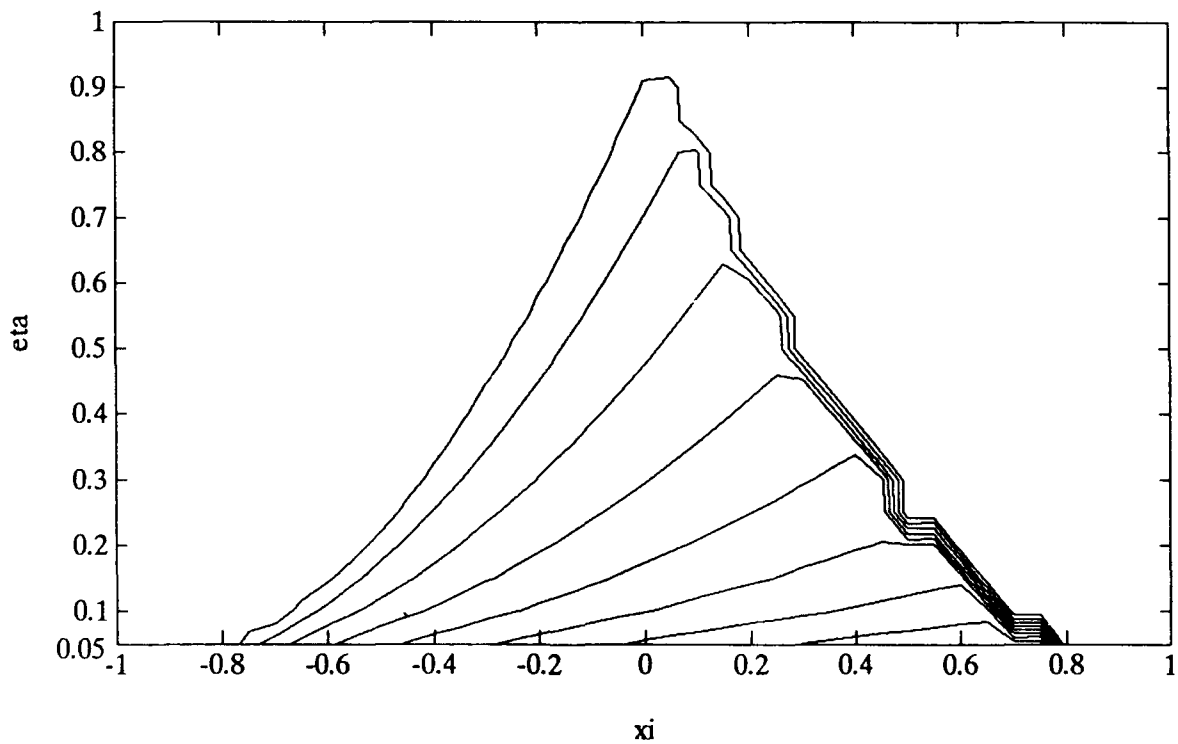


Figure 5.10: Parabolic contour plot of $\frac{\lambda_1}{\lambda_2}$ in dB as function of $\xi$ and $\eta$ for $\frac{\pi_1}{\pi_2} = 0$ dB.

Figure 5.11: Mesh plot of $\frac{\lambda_1}{\lambda_2}$ in dB as function of $\xi$ and $\eta$ for $\frac{\pi_1}{\pi_2} = 10$ dB.
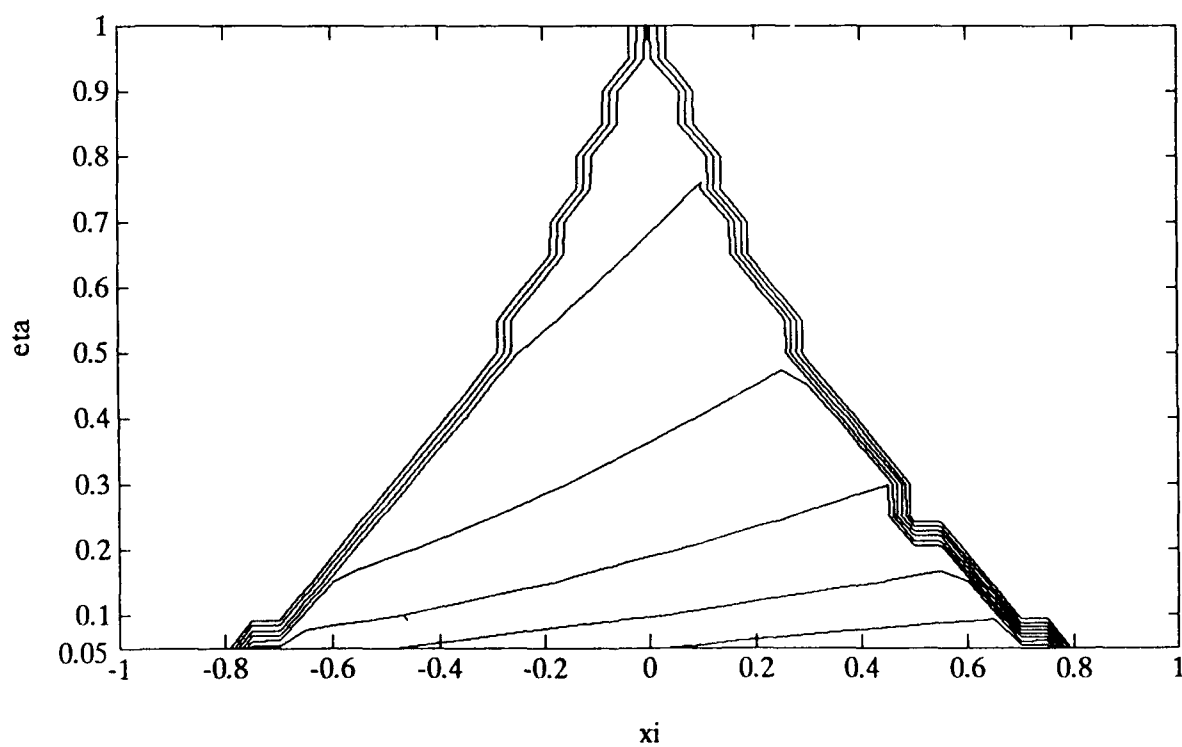


Figure 5.12: Parabolic contour plot of $\frac{\lambda_1}{\lambda_2}$ in dB as function of $\xi$ and $\eta$ for $\frac{\pi_1}{\pi_2} = 10$ dB.
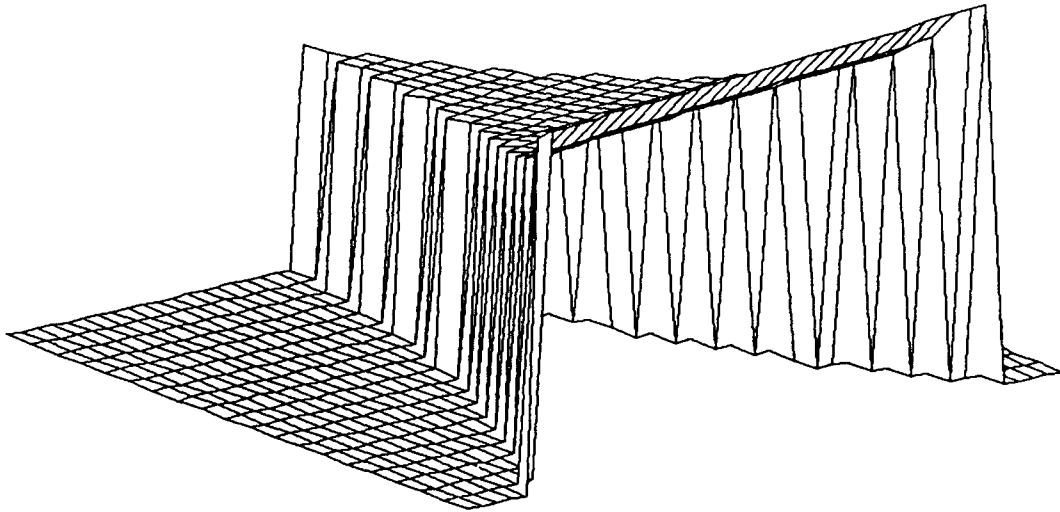
Figure 5.13: Mesh plot of $\frac{\lambda_1}{\lambda_2}$ in dB as function of $\xi$ and $\eta$ for $\frac{\pi_1}{\pi_2} = 20$ dB.
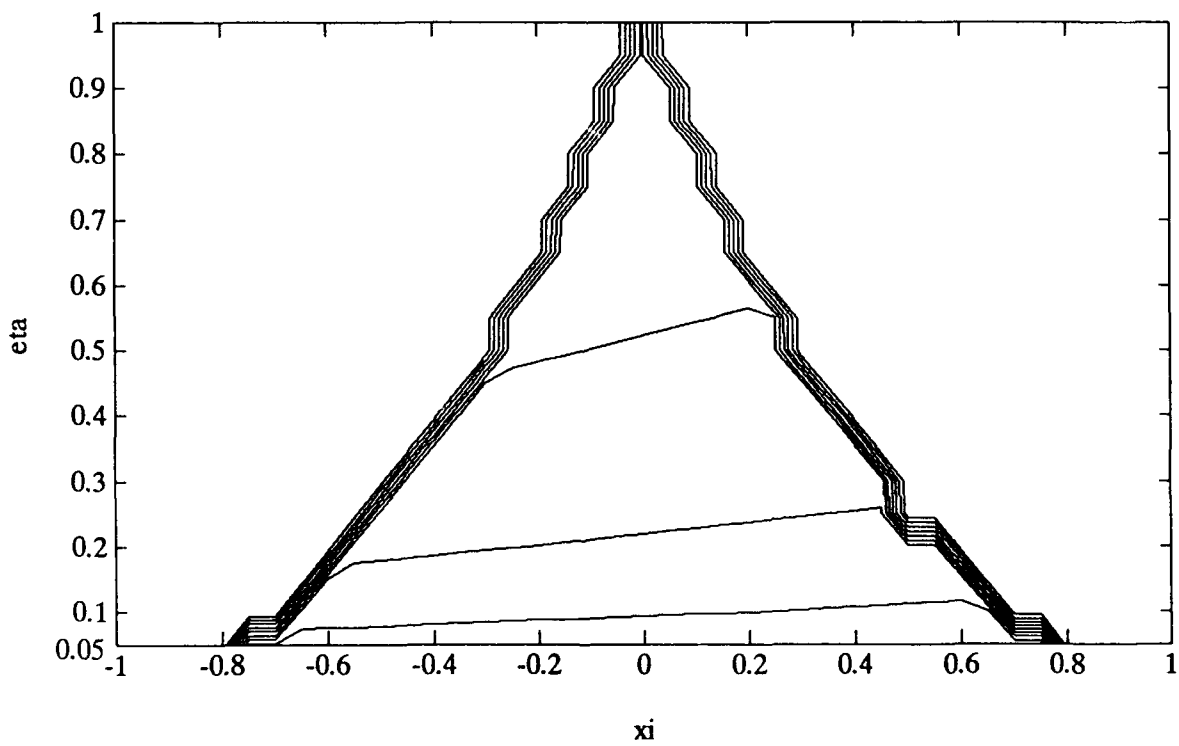


Figure 5.14: Parabolic $\frac{\lambda_1}{\lambda_2}$ in dB as contour plot of function of $\xi$ and $\eta$ for $\frac{\pi_1}{\pi_2} = 20$ dB.
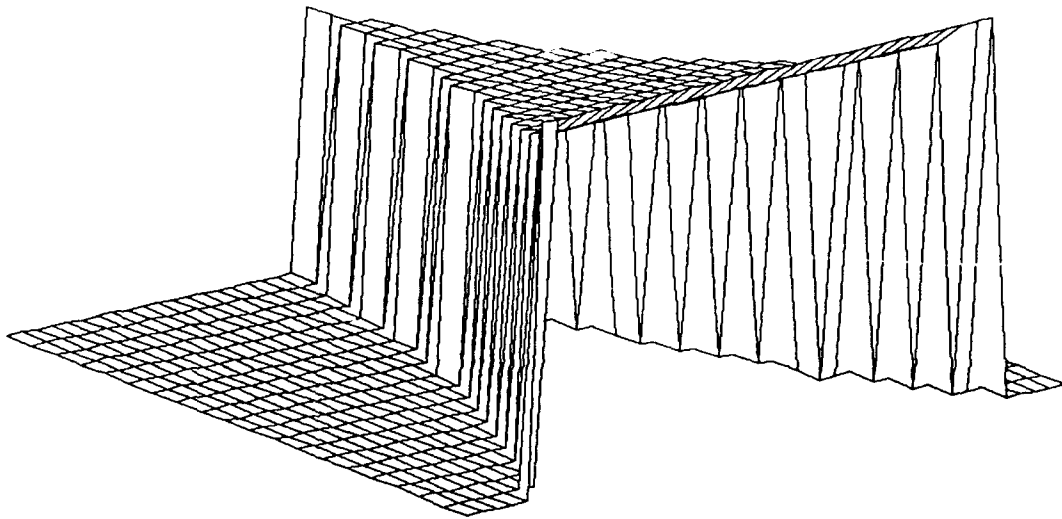
Figure 5.15: Mesh plot of $\frac{\lambda_1}{\lambda_2}$ in dB as function of $\xi$ and $\eta$ for $\frac{\pi_1}{\pi_2} = 30$ dB.
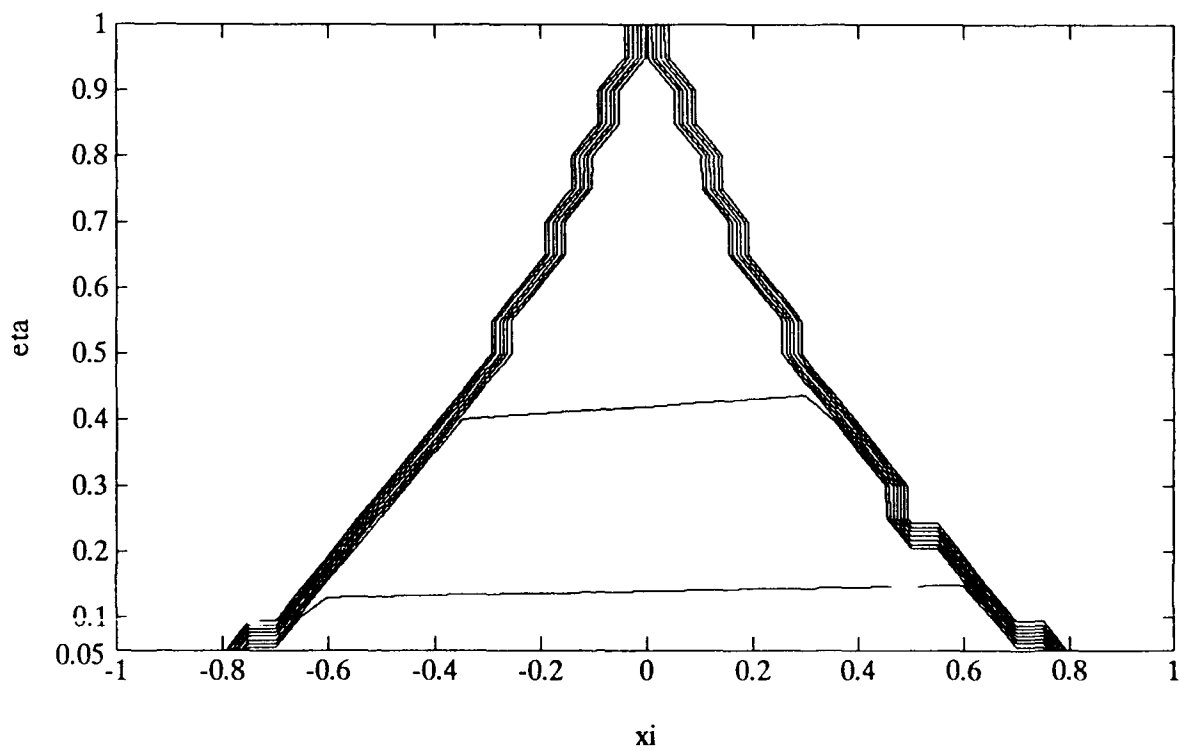


Figure 5.16: Parabolic contour plot of $\frac{\lambda_1}{\lambda_2}$ in dB as function of $\xi$ and $\eta$ for $\frac{\pi_1}{\pi_2} = 30$ dB.
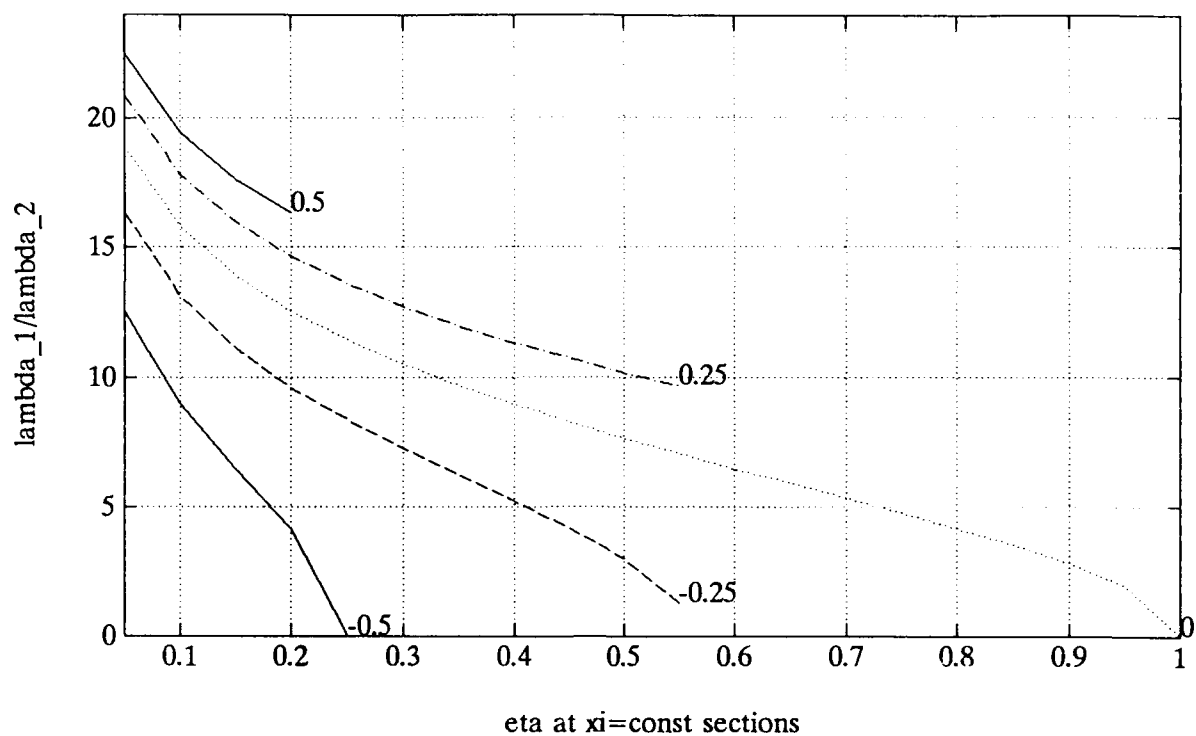
Figure 5.17: Slices of $\frac{\lambda_1}{\lambda_2}$ in dB at $\xi = -0.5, -0.25, 0, +0.25, +0.5$ for $\frac{\pi_1}{\pi_2} = 0$ dB.
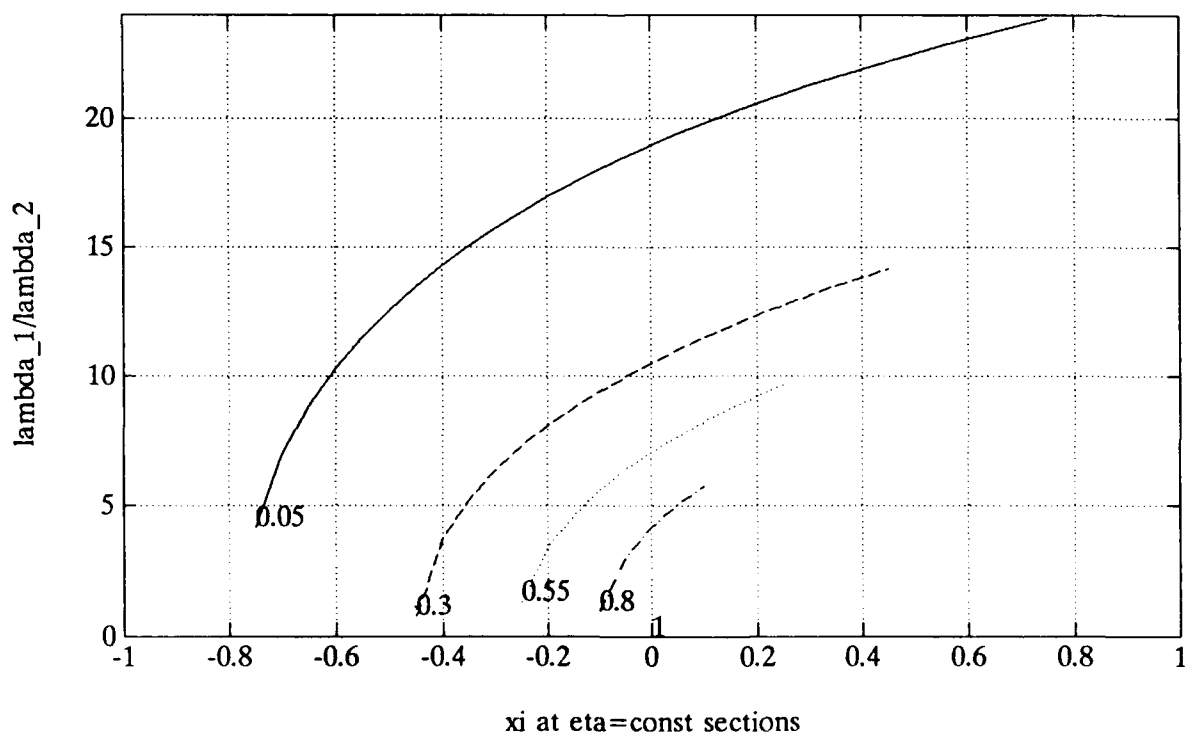


Figure 5.18: Slices of $\frac{\lambda_1}{\lambda_2}$ in dB at $\eta = 0.05, 0.25, 0.50, 0.75, 1.00$ for $\frac{\pi_1}{\pi_2} = 0$ dB.
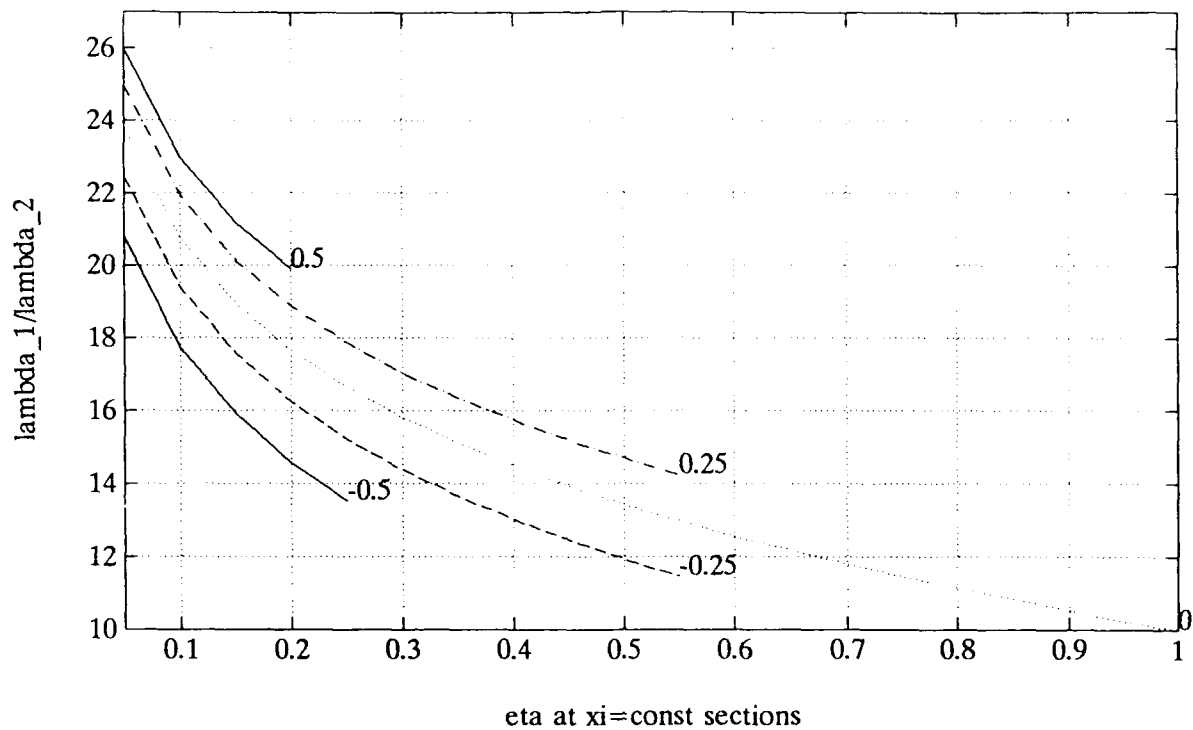
Figure 5.19: Slices of $\frac{\lambda_1}{\lambda_2}$ in dB at $\xi = -0.5, -0.25, 0, +0.25, +0.5$ for $\frac{\pi_1}{\pi_2} = 10$ dB.
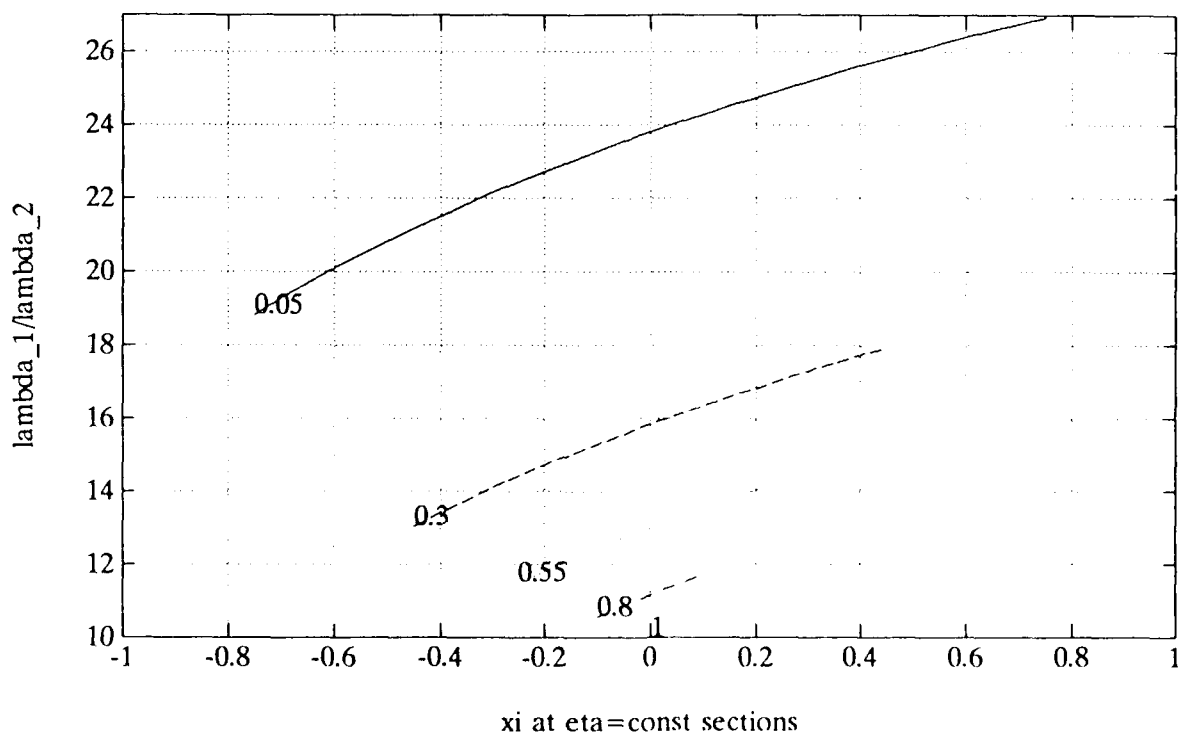


Figure 5.20: Slices of $\frac{\lambda_1}{\lambda_2}$ in dB at $\eta = 0.05, 0.25, 0.50, 0.75, 1.00$ for $\frac{\pi_1}{\pi_2} = 10$ dB.
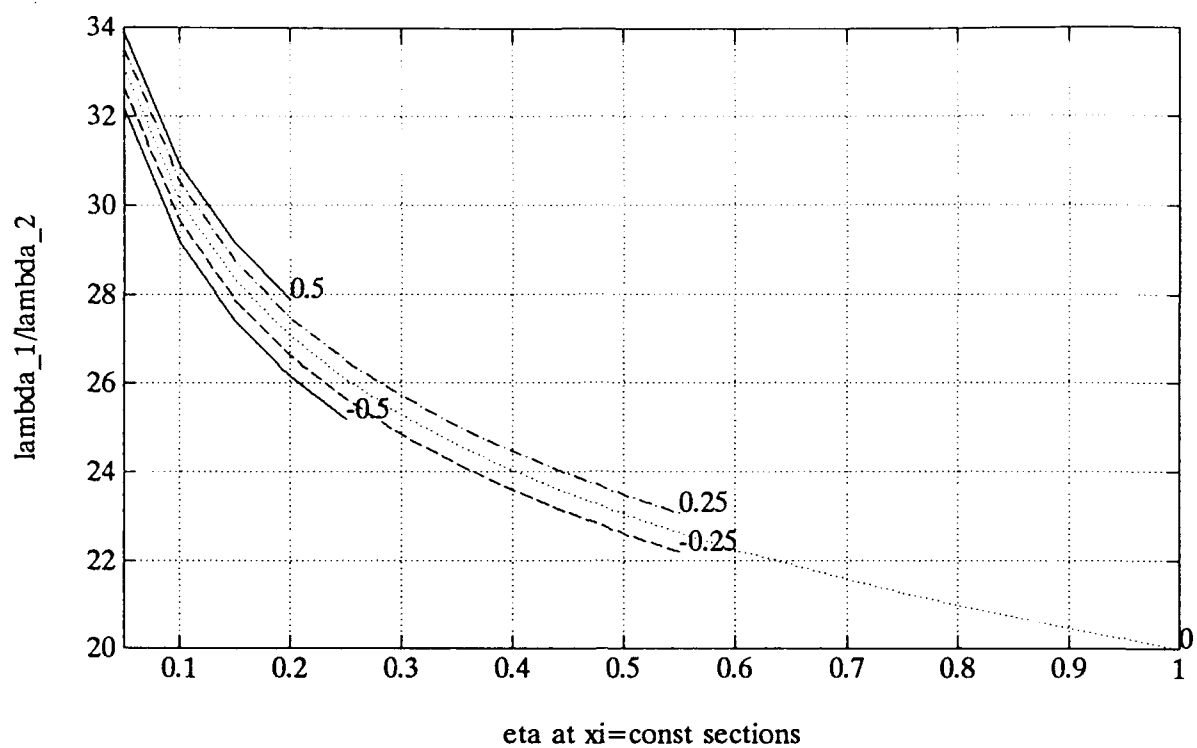
Figure 5.21: Slices of $\frac{\lambda_1}{\lambda_2}$ in dB at $\xi = -0.5, -0.25, 0, +0.25, +0.5$ for $\frac{\pi_1}{\pi_2} = 20$ dB.
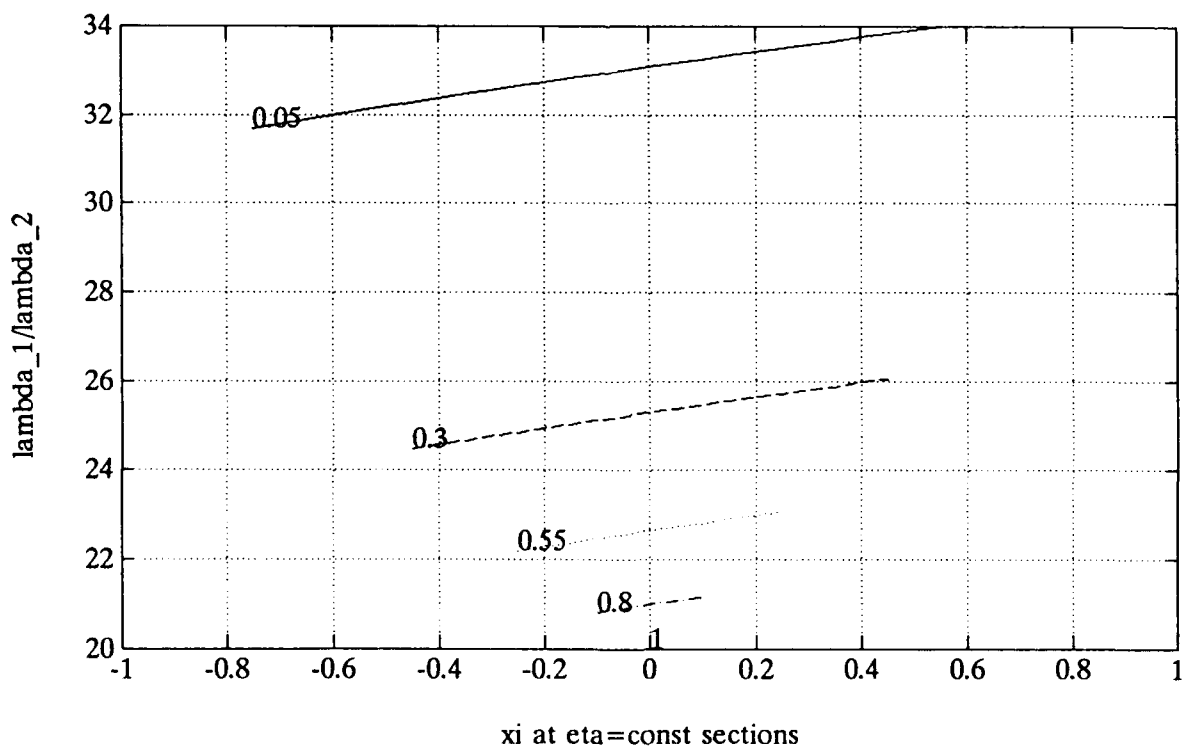


Figure 5.22: Slices of $\frac{\lambda_1}{\lambda_2}$ in dB at $\eta = 0.05, 0.25, 0.50, 0.75, 1.00$ for $\frac{\pi_1}{\pi_2} = 20$ dB.

71
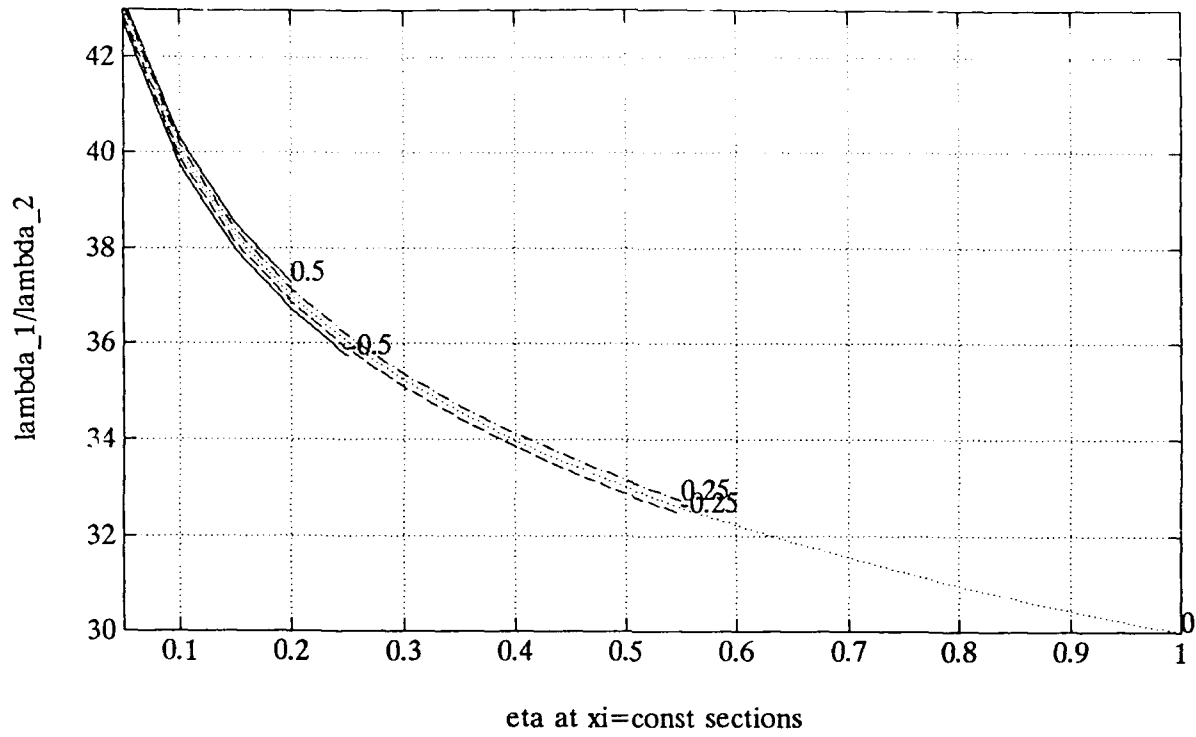
Figure 5.23: Slices of $\frac{\lambda_1}{\lambda_2}$ in dB at $\xi = -0.5, -0.25, 0, +0.25, +0.5$ for $\frac{\pi_1}{\pi_2} = 30$ dB.
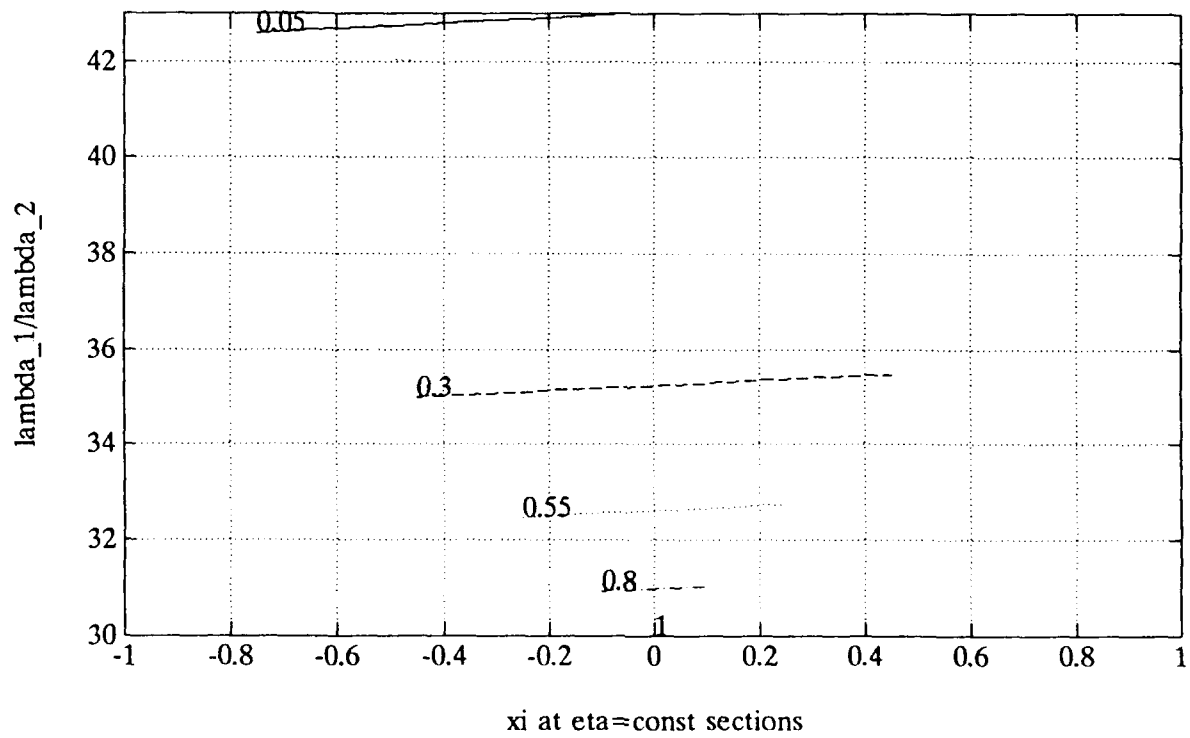


Figure 5.24: Slices of $\frac{\lambda_1}{\lambda_2}$ in dB at $\eta = 0.05, 0.25, 0.50, 0.75, 1.00$ for $\frac{\pi_1}{\pi_2} = 30$ dB.

## 5.3 Plots of Signal Eigenvalue Ratio $\frac{\lambda_1}{\lambda_2}$ Over a Small Phase-Independent Variable $\eta = 0.05$ as Function of Phase-Dependent Variable $\xi$ and Power Ratio $\frac{\pi_1}{\pi_2}$(dB)

We plot, for a small constant $\eta = 0.05$, signal eigenvalue ratio $\frac{\lambda_1}{\lambda_2}$ as function of the phase-dependent variable $\xi$ and power ratio $\frac{\pi_1}{\pi_2}$, then plot slices along constant power ratio $\frac{\pi_1}{\pi_2}$ and then along constant phase-dependent variable $\xi$.

- $\frac{\lambda_1}{\lambda_2}$ at $\frac{\pi_1}{\pi_2}$(dB)=0,5,10,15,20,25,30 for $\eta$=0.05 in figure 5.25.

- $\frac{\lambda_1}{\lambda_2}$ at $\xi = -0.50, -0.25, 0, +0.25, +0.50$ for $\eta$=0.05 in figure 5.26.

- Mesh and contour plots of $\frac{\lambda_1}{\lambda_2}$ in dB for $\eta$=0.05 in figures 5.27, and 5.28.

As we mentioned at the beginning of the chapter, we choose to stop at $\eta = -13$ dB. From the slice plot of the signal eigenvalue ratio $\frac{\lambda_1}{\lambda_2}$ along constant power ratio $\frac{\pi_1}{\pi_2}$ in figure 5.25, we see that the spread in the eigenvalue ratio is smaller at the constructive interference side, $\xi > 0$, than at the destructive interference side, $\xi \leq 0$. The eigenvalue ratio is an increasing function of the phase-dependent variable $\xi$ but this dependence levels off as the power ratio $\frac{\pi_1}{\pi_2}$ increases.

From the slice plot of the signal eigenvalue ratio $\frac{\lambda_1}{\lambda_2}$ along constant phase-dependent variable $\xi$ in figure 5.26, we see that the spread in eigenvalue ratio narrows quickly as the power ratio $\frac{\pi_1}{\pi_2}$ increases. This means that the dependence on the phase-dependent variable $\xi$ becomes negligible. The trend is a 45° line in the log-log plot, which means that the signal eigenvalue ratio $\frac{\lambda_1}{\lambda_2}$ becomes directly proportional to the power ratio $\frac{\pi_1}{\pi_2}$ in the direct scale.

The above observations are reinforced in the contour plot of figure 5.28 showing signal eigenvalue ratio $\frac{\lambda_1}{\lambda_2}$ as a function of the phase-dependent variable $\xi$ and power ratio $\frac{\pi_1}{\pi_2}$. The variation of the contour is mainly in the power ratio $\frac{\pi_1}{\pi_2}$ direction. Its change in the phase-dependent variable $\xi$ direction is pronounced only for $\frac{\pi_1}{\pi_2} < 15$ dB.

Except when a paper focuses on the effect of the temporal phase difference, the phase of the source correlation is frequently implicitly assumed to be zero. Often we have to infer this from the following clues: the source correlation coefficient used in evaluating asymptotic performance is a positive real (without discussion), or identical complex source amplitudes for the two arrivals are used in numerical simulation. The position of a stressful scenario point in the isosceles region can be anywhere on the right-half of the constant $\eta$ line parallel to the close-by baseline. For these highly correlated equipower arrivals, we will show that the effect on the eigenvalue ratio from changing the phase of the source correlation from 90° to 0° can be as high as a 6-dB increase. The following paragraphs explain the possible 6-dB increase of the eigenvalue ratio adjustment.

The large eigenvalue $\lambda_1$ near the baseline corresponding to temporally highly correlated arrivals can be estimated using the asymptotes' behavior, because the cross sections of the $\lambda$s' surfaces for constant $\eta$s are hyperbolic slices, as derived in subsection 3.4.3 and shown in figure 3.6. Depending on the relative location of the scenario point to the right boundary curve of the isosceles region, the effect on the large eigenvalue $\lambda_1$ from changing the phase of the source correlation from 90° to 0° can be as high as a 3-dB increase.

The small eigenvalue $\lambda_2$ can be estimated from the following fact derived in subsection 3.4.2 and shown in figure 3.5. Near $\eta = 0$ and at the three particular $\xi$ values, we have

$$\lambda_2(-1, \eta) \approx \infty \eta, \quad \lambda_2(0, \eta) \approx \frac{\eta}{2}, \quad \lambda_2(1, \eta) \approx \frac{\eta}{4}.$$

73
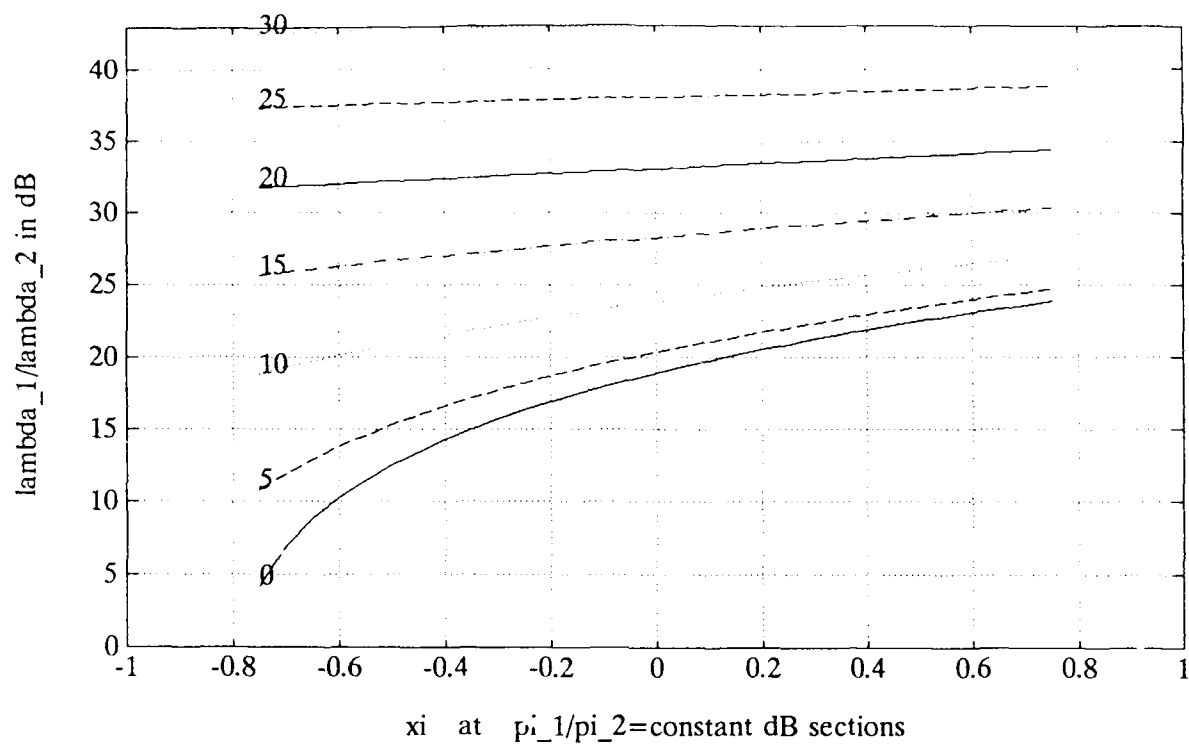
Figure 5.25: $\frac{\lambda_1}{\lambda_2}$ in dB vs $\xi$ at $\frac{\pi_1}{\pi_2}$(dB)=0,5,10,15,20,25,30 for $\eta$=0.05.
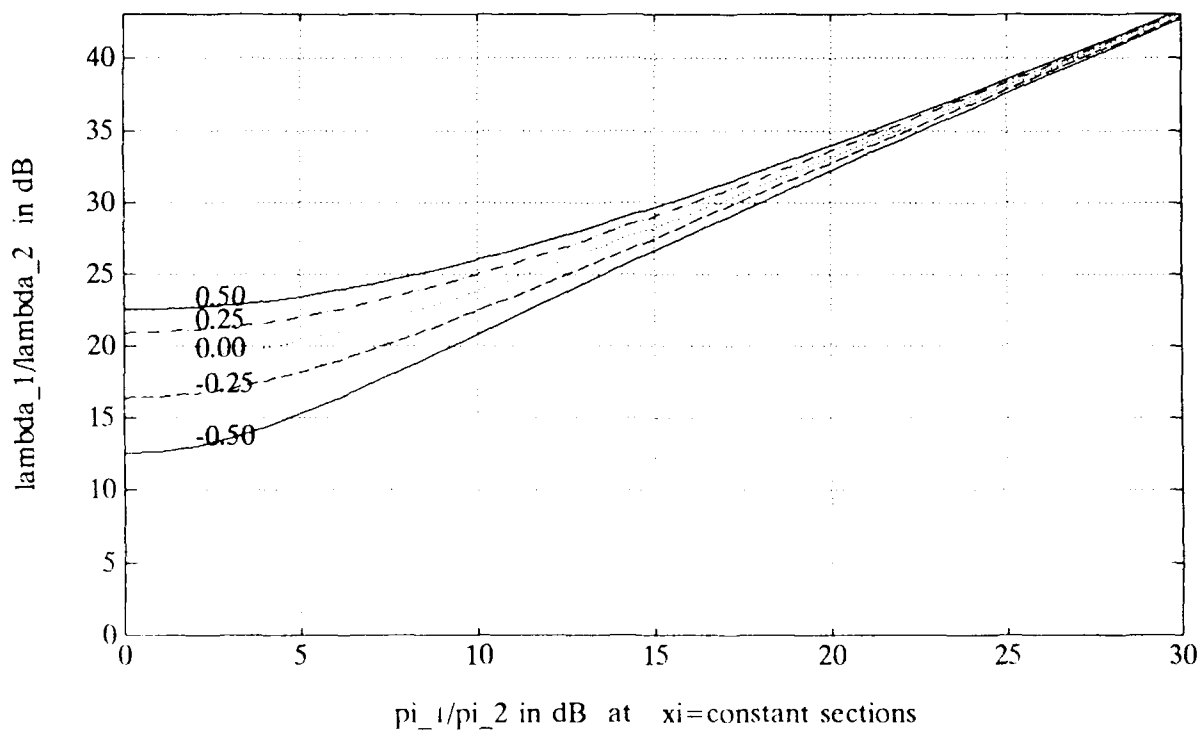


Figure 5.26: $\frac{\lambda_1}{\lambda_2}$ in dB vs $\frac{\pi_1}{\pi_2}$ at $\xi = -0.50, -0.25, 0, +0.25, +0.50$ for $\eta$=0.05.
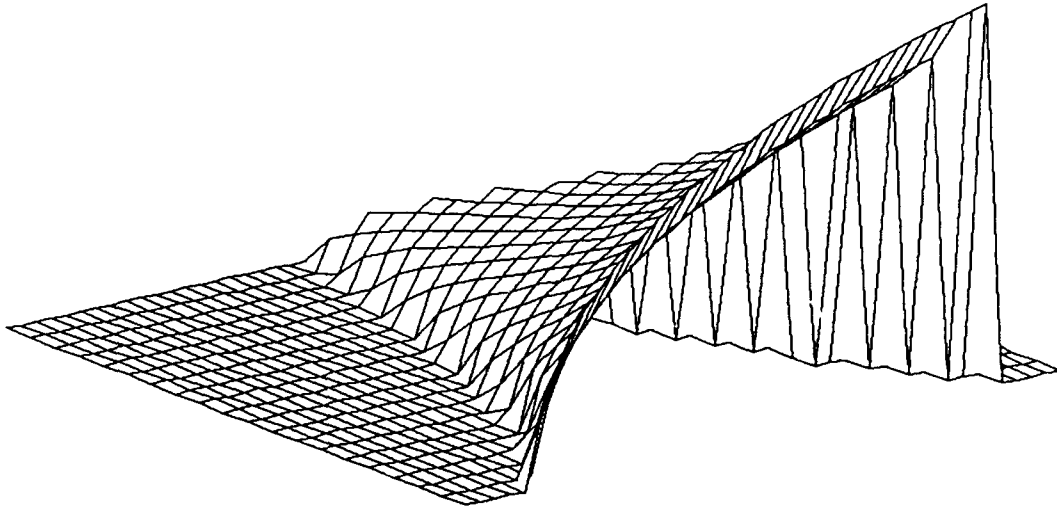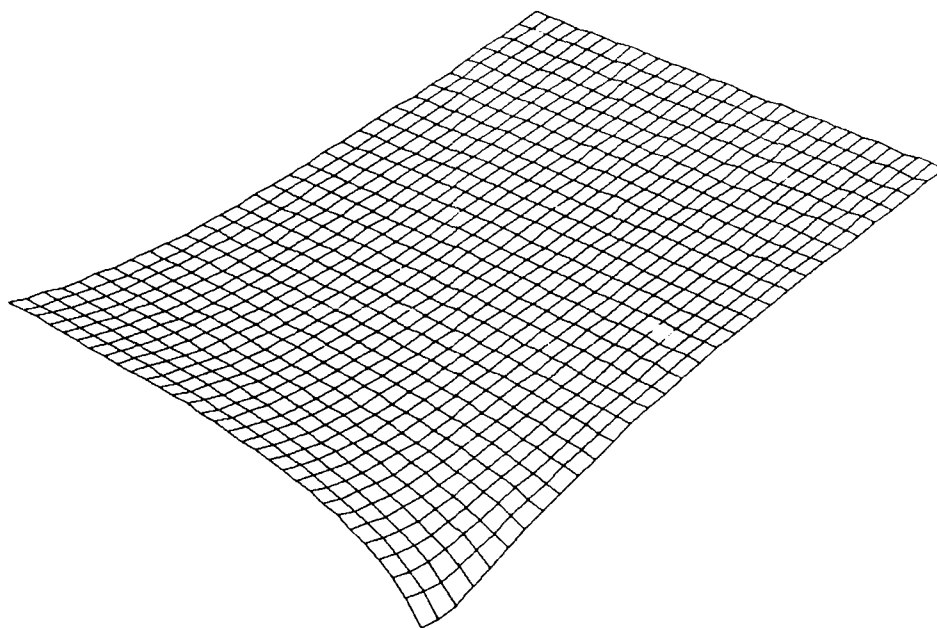
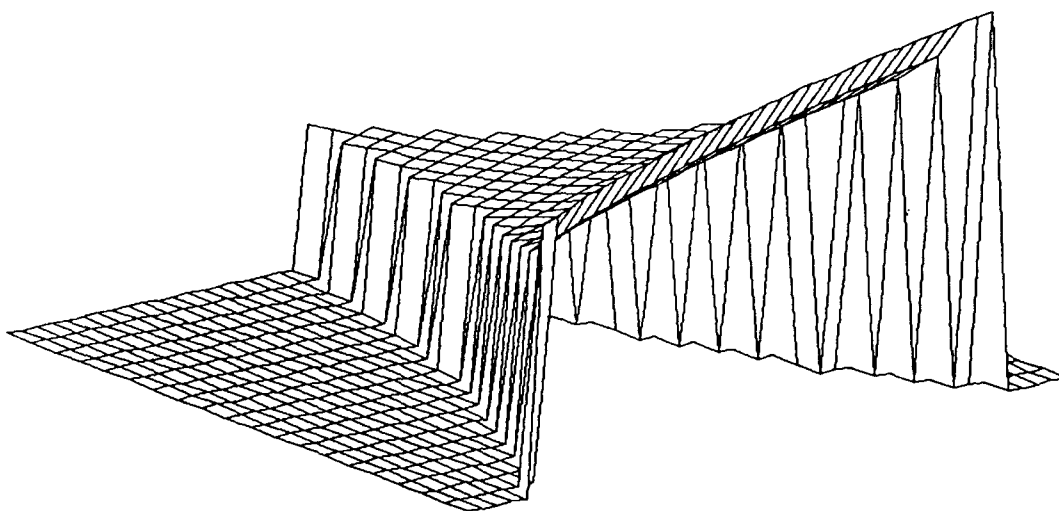Figure 5.27: Mesh plot of $\frac{\lambda_1}{\lambda_2}$ in dB as function of $\xi$ and $\frac{\pi_1}{\pi_2}$ for $\eta=0.05$.
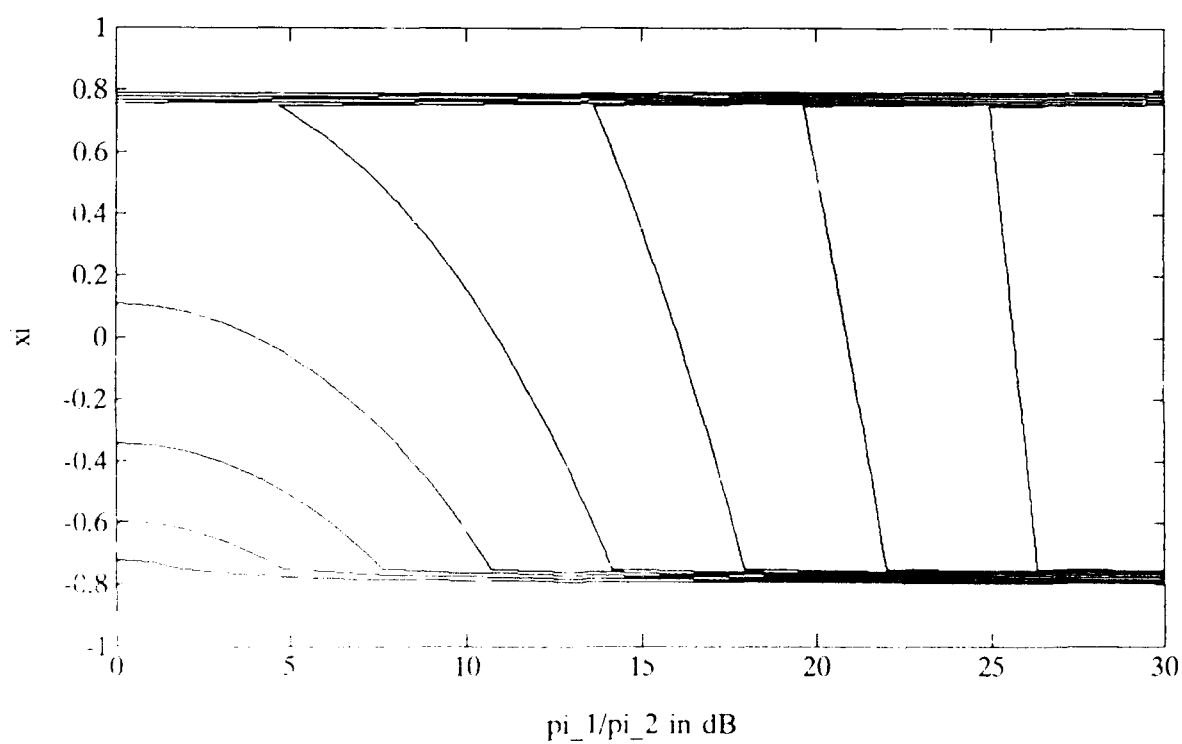


Figure 5.28: Contour plot of $\frac{\lambda_1}{\lambda_2}$ in dB as function of $\xi$ and $\frac{\pi_1}{\pi_2}$ for $\eta=0.05$.

Depending on the relative location of the scenario point to the right boundary curve of the isosceles region, the effect on the small eigenvalue $\lambda_2$ from changing the phase of the source correlation from 90° to 0° can be as high as a 3-dB decrease. See figure 3.6 to reinforce the above discussion.

For the case of almost orthogonal spatial arrivals, the scenario point is near the vertical axis of the isosceles region to start with, no adjustment of the eigenvalue ratio is needed as we move to the 0° temporal correlation. When a scenario is stressed both temporally and spatially, then the relative position of the $(\xi, \eta)$ on the constant $\eta$ line as measured by the fraction distance between the vertical axis to the right boundary of the isosceles region is almost one. In this case, the full 6-dB adjustment is needed.

This can be seen from the following. Given the complex pair $(\phi, \rho)$, we calculate the real pair $(\xi, \eta)$ from

$$\eta = (1 - |\phi|^2)(1 - |\rho|^2),$$

$$\xi = \text{Re}(\rho\phi^*) = |\rho||\phi| \cos(\arg \rho - \arg \phi).$$

For this $\eta$, the boundary point is defined in section 3.2 by

$$|\xi|_{\text{max}} = (|\rho||\phi|)_{\text{max}} = 1 - \sqrt{\eta}.$$

The fractional distance for a 0° temporal correlation scenario point is expressed as

$$\frac{|\xi|}{|\xi|_{\text{max given } \eta}} = \frac{|\rho||\phi|}{1 - \sqrt{(1 - |\phi|^2)(1 - |\rho|^2)}}.$$

When both $|\rho| \approx 1$ and $|\phi| \approx 1$, we have

$$\frac{|\xi|}{|\xi|_{\text{max given } \eta}} \approx |\rho||\phi|(1 + 2\sqrt{(1 - |\phi|)(1 - |\rho|)}) \approx |\rho||\phi| \approx 1.$$

The above discussions about the effect of 6-dB increase on the eigenvalue ratio for highly correlated equipower arrivals from changing the phase of the source correlation from 90° to 0° can be correlated with figures 5.25 and 5.26 for the small phase-independent variable $\eta = 0.05$.

## 5.4 Plots of Signal Eigenvalue Ratio $\frac{\lambda_1}{\lambda_2}$ Over the Vertical Axis $\xi = 0$ as Function of Phase-Independent Variable $\eta$ and Power Ratio $\frac{\pi_1}{\pi_2}$(dB)

Having ascertained that for $\frac{\pi_1}{\pi_2} > 10$ dB the variation of signal eigenvalue ratio $\frac{\lambda_1}{\lambda_2}$ across the phase-dependent variable $\xi$ is not significant, we can focus attention to the condition number's behavior over the vertical axis $\xi = 0$ of the isosceles region.

We plot for $\xi = 0$, signal eigenvalue ratio $\frac{\lambda_1}{\lambda_2}$ as function of the phase-independent variable $\eta$ and power ratio $\frac{\pi_1}{\pi_2}$, next plot slices along constant power ratio $\frac{\pi_1}{\pi_2}$ and then along constant phase-independent variable $\eta$.

There are two versions of these plots. The first version has the phase-independent variable $\eta$ in dB scale covering [−40:0:1], following the convention explained in the previous subsection. The second version has the phase-independent variable $\eta$ in direct or linear scale covering [0.05:1.00:0.05].

### 5.4.1 With Phase-Independent Variable $\eta$ in dB Scale

**Signal Eigenvalue Ratio $\frac{\lambda_1}{\lambda_2}$(dB) vs Phase-Independent Variable $\eta$(dB) Curves at 7 Constant Power Ratio $\frac{\pi_1}{\pi_2}$(dB) for $\xi = 0$**

From figure 5.29 for $\xi = 0$ with seven curves of $\frac{\lambda_1}{\lambda_2}$(dB) vs $\eta$(dB)=−40:1:0
at $\frac{\pi_1}{\pi_2}$(dB)=0,5,10,15,20,25,30, we have the following observations.

At the 0-dB right edge with $\eta$=1 which corresponds to the apex of the isosceles-right-triangle-like region, each of the seven curves corresponding to the 7 $\frac{\pi_1}{\pi_2}$(dB) sections intersects the $\frac{\lambda_1}{\lambda_2}$ dB axis at exactly the same values of each $\frac{\pi_1}{\pi_2}$ curve's labelling, as they should. From $\eta \leq -10$ dB or $\leq$ 0.10 down, i.e., except for the last two vertical grid intervals, these 7 curves are almost all straight lines with slope of −1 in this log-log plot.

We notice the top 3 curves corresponding to $\frac{\pi_1}{\pi_2}$=30, 25, and 20 dB passing through the intersections of horizontal and vertical grid lines. For example, the top curve with $\frac{\pi_1}{\pi_2}$=30 dB passes through these grid points: $(\eta, \frac{\pi_1}{\pi_2}) = (0, 30), (-10, 40), (-20, 50), (-30, 60)$, and $(-40, 70)$. Note the equal spacing among the three curves. When $\frac{\pi_1}{\pi_2} > 10$ dB, we have

$$\frac{\lambda_1}{\lambda_2} \approx (\frac{\pi_1}{\pi_2})/\eta,$$

or that the stress from $\eta$ and $\frac{\pi_1}{\pi_2}$ is multiplicative (divisive) in the direct scale. In dB scale, this is additive, i.e.,

$$\frac{\lambda_1}{\lambda_2}(\text{in dB}) \approx (\frac{\pi_1}{\pi_2})(\text{in dB}) - \eta(\text{in dB}).$$

This approximation starts to degrade when $\frac{\pi_1}{\pi_2}$ is small and $\eta$ is close to 1. So if this additive or multiplicative relation were perfect instead of being just approximate, the $\frac{\pi_1}{\pi_2}$=10-dB curve will intersect at the left vertical line, $\eta = -40$ dB, to arrive at $\frac{\lambda_1}{\lambda_2}$=50 dB, instead of the 51-dB point. But we can see that the approximation even for the $\frac{\pi_1}{\pi_2}$=10-dB curve is excellent.

For $\eta$ larger than 0.10, the lowest 2 curves corresponding to $\frac{\pi_1}{\pi_2}$=0 dB and 5 dB exhibit noticeable curvature, especially for $\frac{\pi_1}{\pi_2}$=0 dB near $\eta$=1. An original 10-dB separation at $\eta = 0$ dB between the two curves $\frac{\pi_1}{\pi_2} = 0$ dB and $\frac{\pi_1}{\pi_2} = 10$ dB is reduced to 5 dB for $\eta \leq -5$ dB.

Figure 5.29: $\frac{\lambda_1}{\lambda_2}$(dB) vs $\eta$(dB)=−40:1:0 at $\frac{\pi_1}{\pi_2}$(dB)=0,5,10,15,20,25,30 for $\xi$=0.
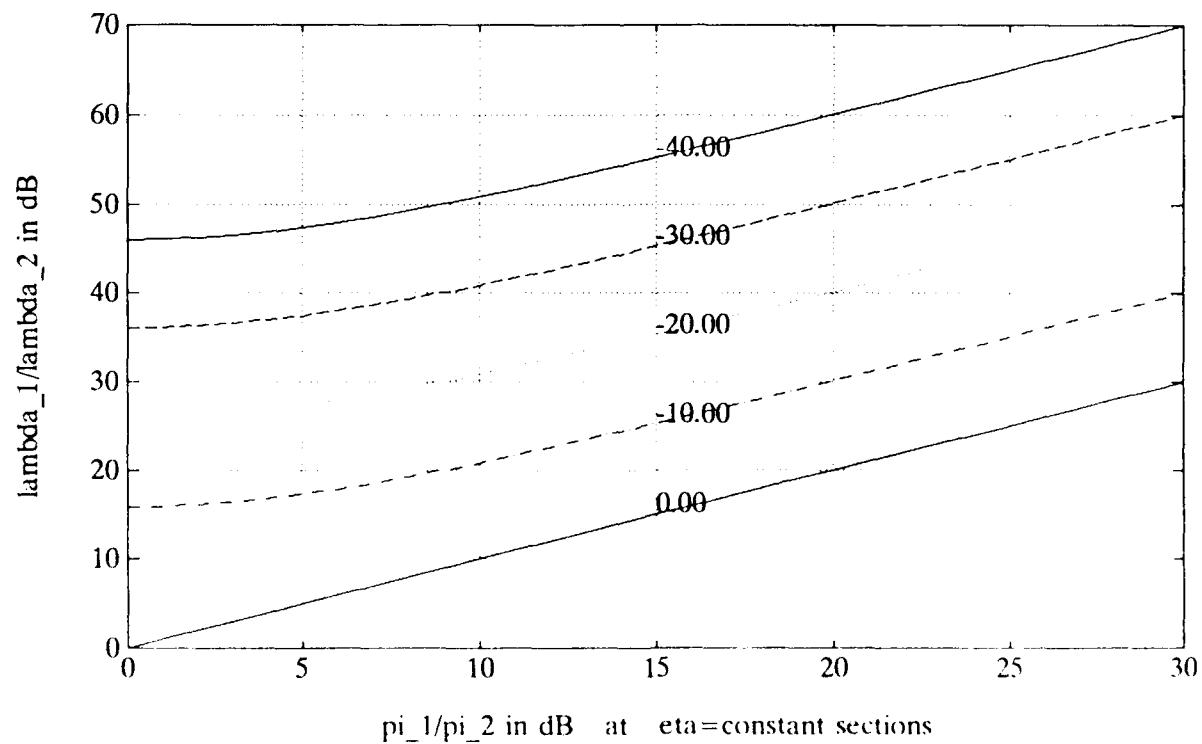


Figure 5.30: $\frac{\lambda_1}{\lambda_2}$(dB) vs $\frac{\pi_1}{\pi_2}$(dB)=0:1:30 at $\eta$(dB)= −40, −30, −20, −10, 0 for $\xi$=0.
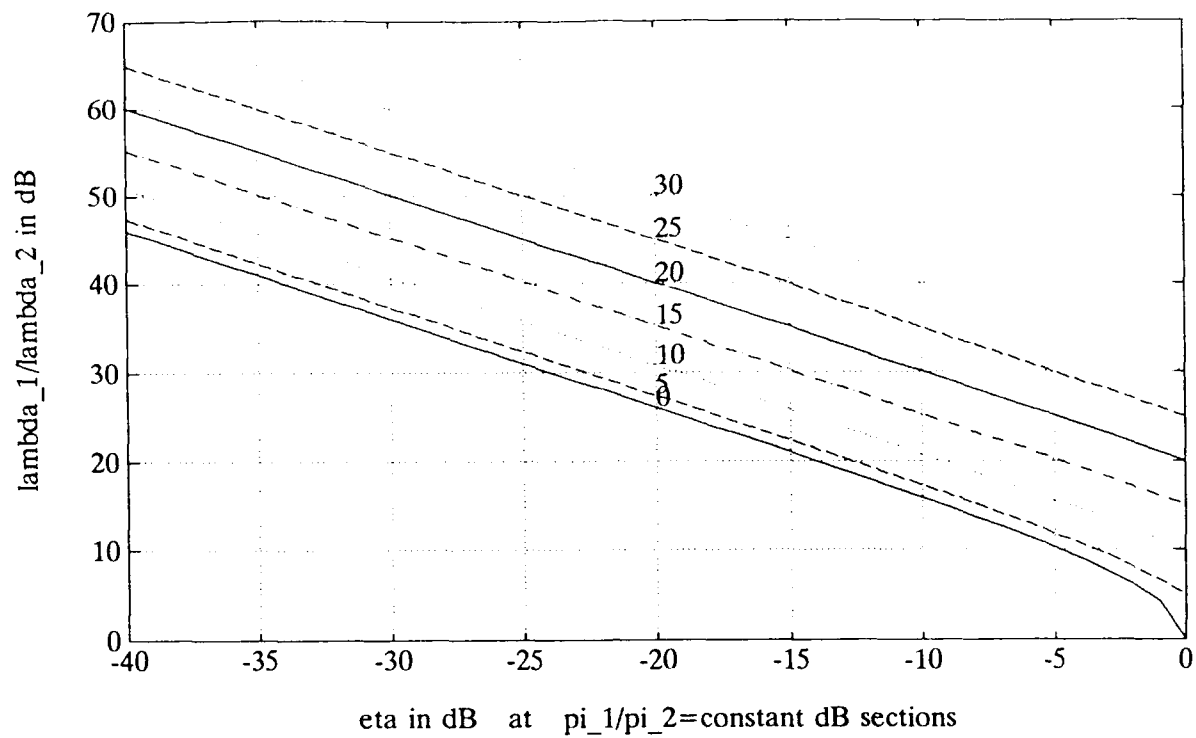
For the $\frac{\pi_1}{\pi_2}$=0-dB curve near $\eta$=1, the apex point area, the stress to the direction-finding scenario due to multipath correlation between arrivals and/or closeness in spatial separation increases much faster than large $\frac{\pi_1}{\pi_2}$ dB curves as $\eta$ decreases. This is caused by the infinite slope of $\lambda$ with respect to $\eta$ at the apex for the equal-power arrival case. Because of this and the variation of $\frac{\lambda_1}{\lambda_2}$ in the $\xi$ direction, we need to examine the surfaces of $\lambda_1$ or $\lambda_2$ or their ratio in detail for the $\frac{\pi_1}{\pi_2}$=0-dB case.

When $\frac{\pi_1}{\pi_2} \approx 0$ dB and $\eta$ is less than 0.10 (or $-10$ dB), we observe that

$$\frac{\lambda_1}{\lambda_2}(\text{in dB}) \approx -\eta(\text{in dB}) + 6.$$

This extra 6 dB accounts for the presence of the infinite slope of $\lambda$ with respect to $\eta$ at the apex for the equal-power arrival case.

Recall that these were predicted in subsection 3.3.3.


**Signal Eigenvalue Ratio $\frac{\lambda_1}{\lambda_2}$(dB) vs Power Ratio $\frac{\pi_1}{\pi_2}$(dB) Curves at Five Constant Phase-Independent Variable $\eta$(dB) for $\xi = 0$**

From figure 5.30 for $\xi = 0$ with five curves of $\frac{\lambda_1}{\lambda_2}$(dB) vs $\frac{\pi_1}{\pi_2}$(dB)=0:1:30
at $\eta$(dB)= $-40, -30, -20, -10, 0$, some of the just mentioned observations can be made clearer from a different perspective.

The lowest curve corresponds to $\eta = 0$ dB, i.e., at the apex point. This perfect straight line with slope of 1 indicates the identical relation between $\frac{\lambda_1}{\lambda_2}$ and $\frac{\pi_1}{\pi_2}$, as it should. The five constant $\eta$ curves are equally spaced in dB. The intersections of these curves with the vertical grid lines reflect how well the corresponding equal spacing can be carried over for $\frac{\lambda_1}{\lambda_2}$ for different $\eta$ values. We see that equal spacing is maintained much better for $\frac{\pi_1}{\pi_2} > 10$ dB than for $\frac{\pi_1}{\pi_2} < 10$ dB. In particular, near the left vertical edge, which corresponds to equal strength arrivals, we can see that the stress rises much faster when $\eta$ decreases from 0 dB, as the DOAs get closer and/or source amplitudes get more correlated. On the other end, the rate of stress rising with respect to the $\frac{\pi_1}{\pi_2}$ abscissa near this left boundary is milder than other $\frac{\pi_1}{\pi_2}$ values. In other words, the slopes of these five curves, except the lowest one corresponding to $\frac{\pi_1}{\pi_2} = 0$ dB, are less than one.

Recall the parabolic slice characterizations for both the equal-arrival special case and the general case over the vertical axis of the isosceles-triangle-like region. For the equal-arrival special case, the slope of $\lambda_2$ with respect to $\eta$ is $\infty$ at the vertex and is $\frac{1}{2}$ at the baseline. For the general case with $\frac{\pi_1}{\pi_2} > 10$ dB, the slope is about 1 throughout the entire region.

The straight lines with slope of $+1$ for $\frac{\pi_1}{\pi_2} > 10$ dB gives another indication of the additive or multiplicative dependency of the total stress on the two contributing factors $\frac{\pi_1}{\pi_2}$ and $\eta$ mentioned above.


**Mesh Surface and Contour Plots of Signal Eigenvalue Ratio $\frac{\lambda_1}{\lambda_2}$(dB) over Phase-Independent Variable $\eta$(dB) and Power Ratio $\frac{\pi_1}{\pi_2}$(dB) for $\xi$=0**

Figures 5.31 and 5.32 for $\xi = 0$ are the mesh surface and contour plots of $\frac{\lambda_1}{\lambda_2}$(dB) vs $\eta$(dB)=$-40$:1:0 and $\frac{\pi_1}{\pi_2}$(dB)=0:1:30.

The previous two plots just discussed are the slices resulting from vertical cutting planes intersecting the mesh surface as displayed here. The contour plot is that resulting from using horizontal cutting planes. The lack of curvature or the straight contour lines for $\frac{\pi_1}{\pi_2} > 10$ dB and the essential equal spacing of the contour lines reinforces the earlier discussions. We have

79

Figure 5.31: Mesh plot of $\frac{\lambda_1}{\lambda_2}$(dB) vs $\eta$(dB)=$-40$:1:0 and $\frac{\pi_1}{\pi_2}$(dB)=0:1:30 for $\xi$=0.
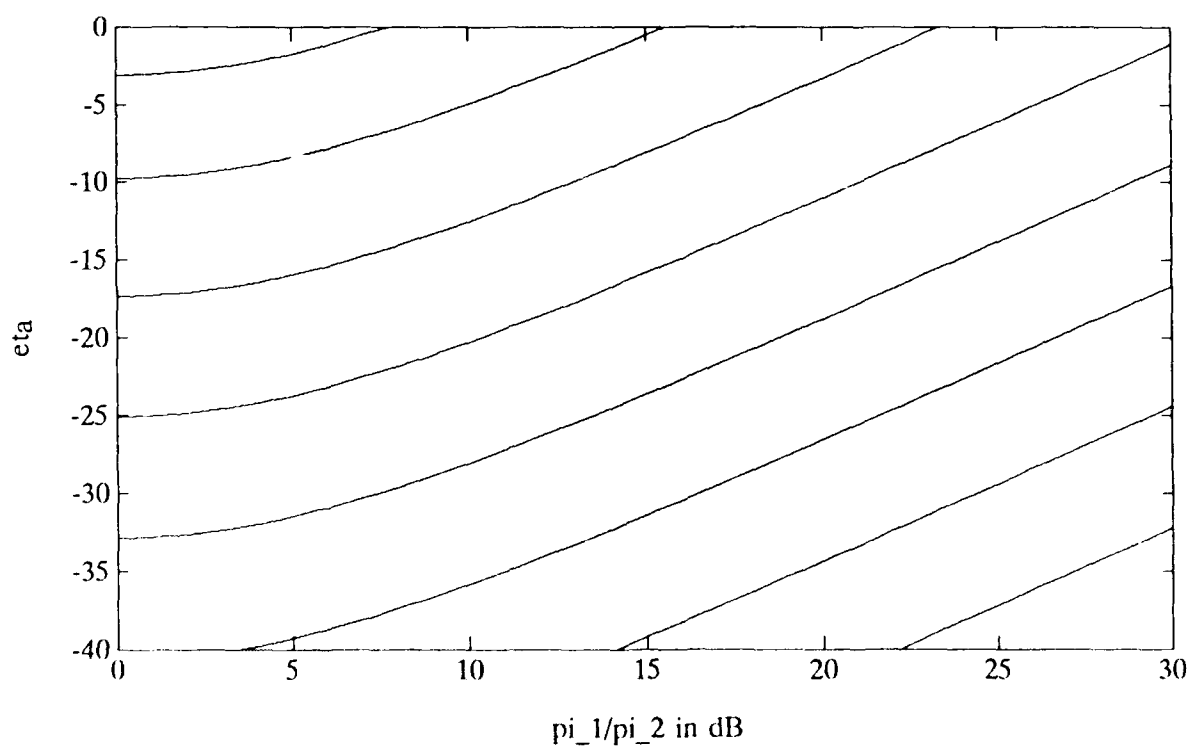


Figure 5.32: Contour plot of $\frac{\lambda_1}{\lambda_2}$(dB) vs $\eta$(dB)= $-40$:1:0 and $\frac{\pi_1}{\pi_2}$(dB)=0:1:30 for $\xi$=0.

discussed in subsection 3.5.4 that for large $\frac{\pi_1}{\pi_2}$, the contours of the eigenvalue ratio $\frac{\lambda_1}{\lambda_2} = l$ for $\xi = 0$ as functions of $\frac{\pi_1}{\pi_2}$ and $\eta$ are $45°$ parallel lines with all three variables $\frac{\lambda_1}{\lambda_2} = l$, $\frac{\pi_1}{\pi_2}$, and $\eta$ in dB scale. All these suggest that a 3-d map with power ratio $\frac{\pi_1}{\pi_2}$ as third coordinate is not needed. The following plots are the "$\eta$ in direct scale" versions of the above "$\eta$ in dB-scale" plots.

## 5.4.2 With Phase-Independent Variable $\eta$ in Direct Scale

**Signal Eigenvalue Ratio $\frac{\lambda_1}{\lambda_2}$(dB) vs Phase-Independent Variable $\eta$ Curves at Seven Constant Power Ratio $\frac{\pi_1}{\pi_2}$(dB) Values for $\xi = 0$**

Figure 5.33 for $\xi = 0$ has seven curves of $\frac{\lambda_1}{\lambda_2}$(dB) vs $\eta$=0.05:0.05:1.00 at $\frac{\pi_1}{\pi_2}$(dB)=0, 5, 10, 15, 20, 25, 30.

**Signal Eigenvalue Ratio $\frac{\lambda_1}{\lambda_2}$(dB) vs Power Ratio $\frac{\pi_1}{\pi_2}$(dB) at Five Constant Phase-Independent Variable $\eta$ Values for $\xi = 0$**

Figure 5.34 for $\xi = 0$ has five curves of $\frac{\lambda_1}{\lambda_2}$(dB) vs $\frac{\pi_1}{\pi_2}$(dB)=0:1:30 at $\eta$=0.05, 0.25, 0.50, 0.75, 1.00.

**Mesh Surface and Contour Plots of Signal Eigenvalue Ratio $\frac{\lambda_1}{\lambda_2}$(dB) over Phase-Independent Variable $\eta$ and Power Ratio $\frac{\pi_1}{\pi_2}$(dB) for $\xi$=0**

Figures 5.35 and 5.36 for $\xi = 0$ are the mesh surface and contour plots of $\frac{\lambda_1}{\lambda_2}$(dB) vs $\eta$=0.05:0.05:1.00 and $\frac{\pi_1}{\pi_2}$(dB)=0:1:30.

We find that the earlier "$\eta$ in dB-scale" plots convey information more effectively and compactly than these "$\eta$ in direct-scale" ones. But the latter ones can be considered as magnified look of the earlier ones of the relatively benign region near the apex with $\eta \geq$ -ts 10 dB or $\geq 0.10$.
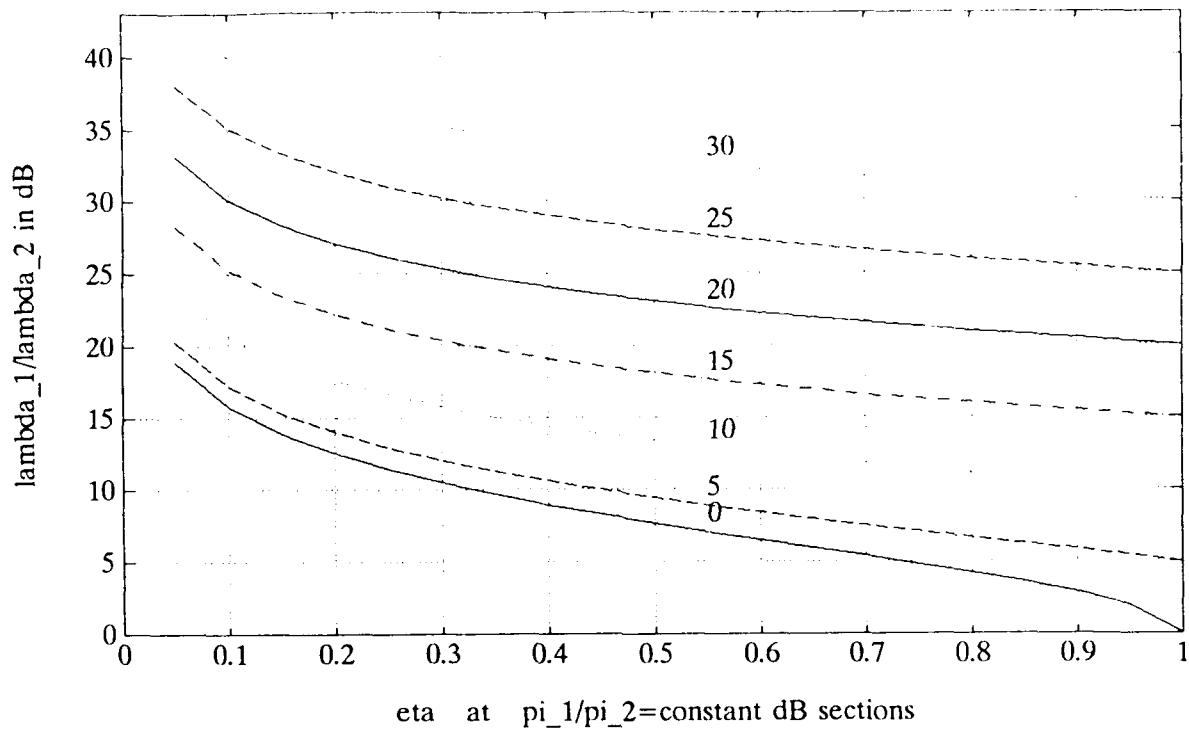
Figure 5.33: $\frac{\lambda_1}{\lambda_2}$(dB) vs $\eta$=0.05:0.05:1.00 at $\frac{\pi_1}{\pi_2}$(dB)=0,5,10,15,20,25,30 for $\xi$=0.
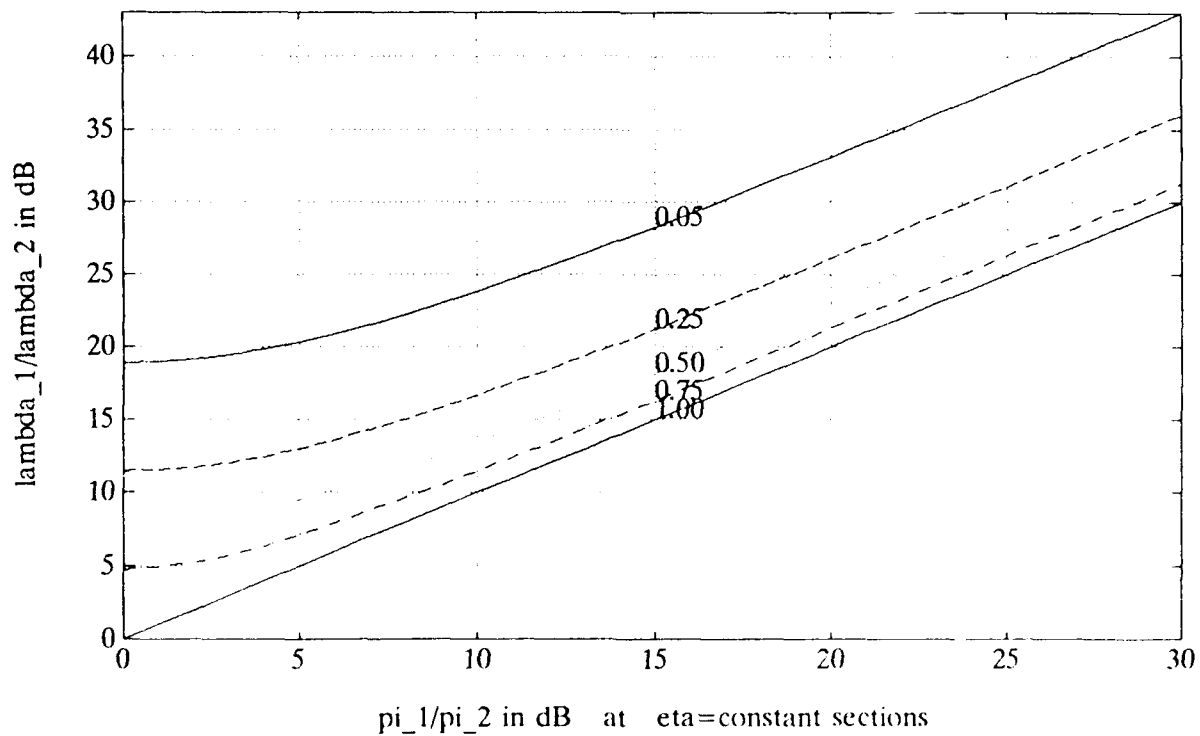


Figure 5.34: $\frac{\lambda_1}{\lambda_2}$(dB) vs $\frac{\pi_1}{\pi_2}$(dB)=0:1:30 at $\eta$=0.05, 0.25, 0.50, 0.75, 1.00 for $\xi$=0.
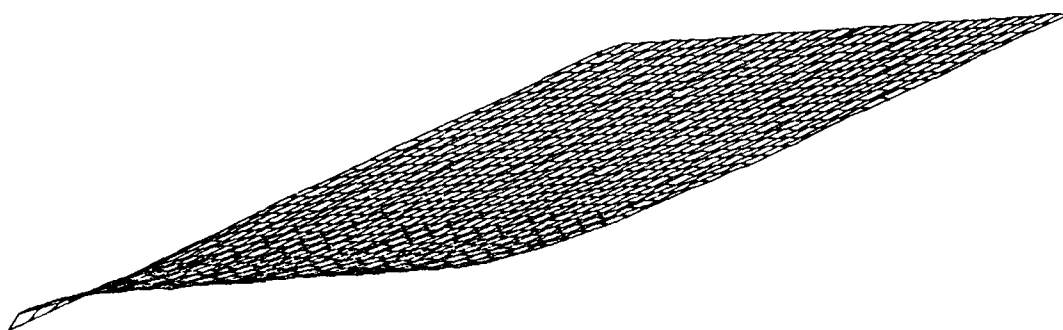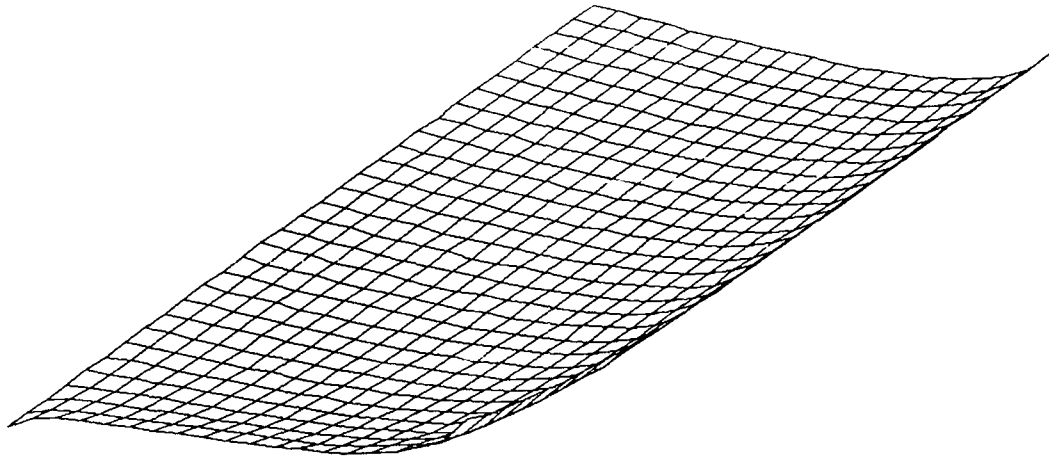
Figure 5.35: Mesh plot of $\frac{\lambda_1}{\lambda_2}$(dB) vs $\eta$=0.05:0.05:1.00 and $\frac{\pi_1}{\pi_2}$(dB)=0:1:30 for $\xi$=0.
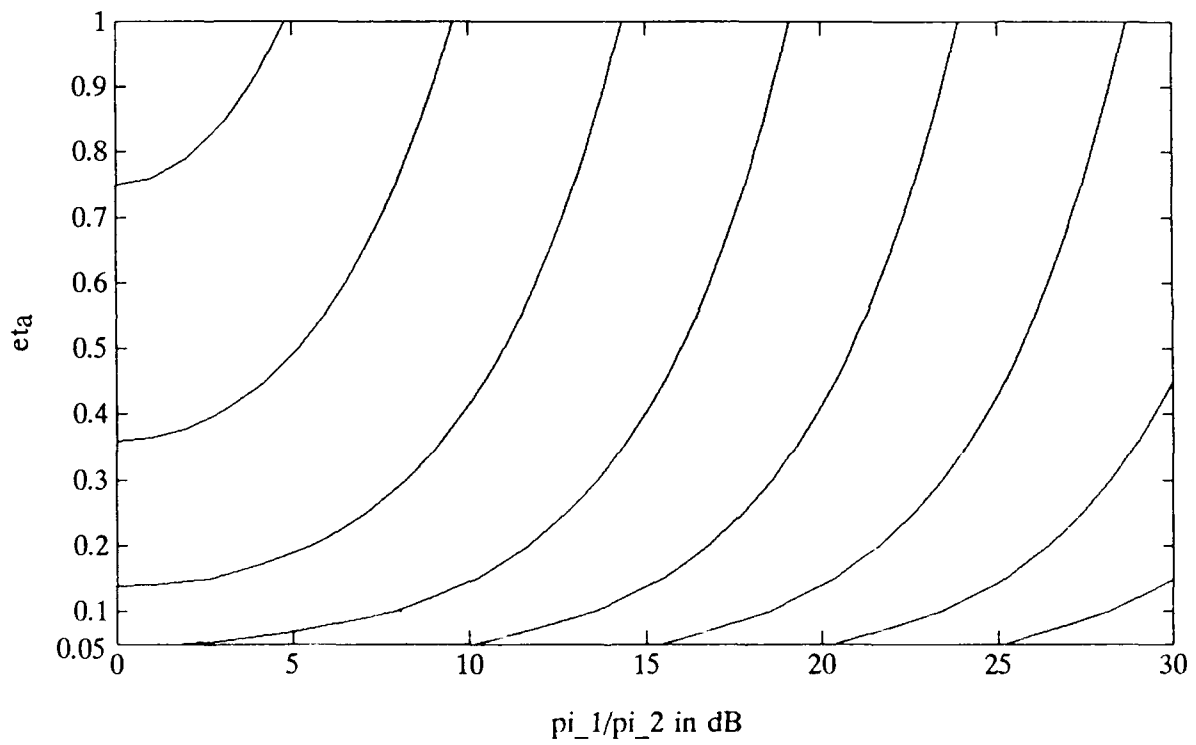


Figure 5.36: Contour plot of $\frac{\lambda_1}{\lambda_2}$(dB) vs $\eta$=0.05:0.05:1.00 and $\frac{\pi_1}{\pi_2}$(dB)=0:1:30 for $\xi$=0.

# Chapter 6

# Some Cadzow's and Ottersten's Scenarios

In this chapter, we will assess some scenarios used by Cadzow[8] and Ottersten[37] in contrasting their results reported on performance comparison between different         ds. We first summarize some approximate results derived in the preceding chapters that will be used in later example scenario discussions. These easy-to-remember formulas enable one to exercise back-of-envelope assessments of scenarios.

## 6.1   A Concise Review of Approximate Formulas Derived Early

Among the three parameters $(\xi, \eta, \frac{\pi_1}{\pi_2})$ appearing in the eigenvalues' expressions, $\eta$ is the most important one. The many-to-one mapping from $(\rho, \phi)$ to $(\xi, \eta)$, or from the Cartesian product of the temporal and spatial correlation unit-disks onto the isosceles-like region, is defined in section 3.1 as

$$\eta = (1 - |\phi|^2)(1 - |\rho|^2),$$

$$\xi = \mathrm{Re}(\rho\phi^*) = |\rho||\phi| \cos(\arg \rho - \arg \phi).$$

When the scenario is stressful, $\eta$ is small and the corresponding annuli with unit outer radius are thin. The area of the temporal correlation $\rho$ annulus can be approximated by the following (aside from a factor of $\pi$):

$$1 - |\rho|^2 = (1 + |\rho|)(1 - |\rho|) \approx 2(1 - |\rho|).$$

For two closely spaced plane waves impinging on a uniform line array (ULA), we have the approximate formula

$$\eta \approx \frac{1}{3}(\pi\theta_{frac\_bw})^2,$$

or

$$\eta(\text{in dB}) \approx 5 + 2 \times \theta_{frac\_bw}(\text{in dB}),$$

as discussed in section 4.2. The formula is at least 90% accurate regardless of the number of sensor elements.

For $\frac{\pi_1}{\pi_2} = 0$ dB and $\eta \leq -10$ dB, we have the approximate formula for $\xi = 0$

$$\frac{\lambda_1}{\lambda_2}(\text{in dB}) \approx -\eta(\text{in dB}) + 6,$$

as derived in section 3.3. For these highly correlated equipower arrivals, the effect on the eigenvalue ratio from changing the phase of the source correlation from 90° to 0° can be as high as a 6-dB increase, as derived in section 6.3.

For $\frac{\pi_1}{\pi_2} > 10$ dB, we have the approximate formula for $\xi = 0$

$$\frac{\lambda_1}{\lambda_2}(\text{in dB}) \approx (\frac{\pi_1}{\pi_2})(\text{in dB}) - \eta(\text{in dB}),$$

as derived in section 3.3. The effect on the eigenvalue ratio from changing the phase of the source correlation from 90° to 0° is negligible for $\frac{\pi_1}{\pi_2} > 15$ dB as discussed in section 5.3.


## 6.2   Temporally Uncorrelated Arrivals

The most stringent scenario used by Cadzow for two nearly broadside uncorrelated arrivals impinging on a circular arc array of eight sensors equally spaced at 3° is now discussed. For $f_0=15$ MHz, a 300-m diameter is 15 wavelengths. As the circular arc is nearly linear, the spatial correlation of the steering vectors of the arrivals for the exact circular arc array is estimated by that of an approximating ULA. A 24°-arc[1] with a 7.5-wavelength radius presents an effective aperture of

$$7.5 \text{ wavelength} \times 24° \times \tfrac{2\pi}{360°} = \pi \text{ wavelength}$$

for broadside DOAs. The 4-dB down Raleigh beamwidth $4\_dB\_down\_bw\_in\_\theta$ is 18.2°. The closest spacing between two arrivals used by Cadzow is 3° which corresponds to a fractional beamwidth of $\theta_{frac\_bw} = 0.16$ for an approximating ULA.

For a ULA with eight sensors and fractional beamwidth $\theta_{frac\_bw} = 0.16$, we read off from figure 4.3 the value of $\lambda_2 = 1 - |\phi| = -14$ dB or $\eta = -11$ dB as we noted $\lambda_2 \approx \frac{\eta}{2}$ in section 4.2 for uncorrelated and equal strength arrivals. The accuracy of reading off curves is probably no better than using the approximate formula for closely spaced arrivals which yields $\frac{2}{6}(\pi \times 0.16)^2 \approx \frac{1}{12}$ or $-11$ dB. Then we read from the curve for $\frac{\pi_1}{\pi_2} = 0$ dB in figure 5.33 with $\eta$ in direct scale the value of $\frac{\lambda_1}{\lambda_2} = 16$ dB. This can also be obtained from the approximate formula which is valid for $\frac{\pi_1}{\pi_2} = 0$ dB and $\eta$ less than $-10$ dB. So, the optimum weight ratio is like 40:1. The tradeoffs conducted by Cadzow were mainly between his (unweighted) algorithm and Det-MLE. The unweighted algorithm was outperformed by Det-ML, but not by much.

The $\frac{\lambda_1}{\lambda_2}$ ratios used by Ottersten for his ULA scenarios are typically in the area of 30 dB, i.e., 1000:1, or higher. For the two equal-SNR uncorrelated arrivals within a Raleigh beamwidth, the most stringent beamwidth separation is $\theta_{frac\_bw} = 1/40 = 0.025$. This is for the three-element half-wavelength spacing case with only 1° separation. For a ULA with three sensors and fractional beamwidth $\theta_{frac\_bw} = 0.025$, we read off from figure 4.1 the value of $\lambda_2 = 1 - |\phi| = -30$ dB, i.e., $\eta = -27$ dB. This can also be obtained from the approximate formula for closely spaced arrivals as $\frac{2}{6}(\pi/40)^2 \approx \frac{1}{500}$. Then we read from the curve for $\frac{\pi_1}{\pi_2} = 0$ dB in figure 5.29 with $\eta$ in dB scale the value of $\frac{\lambda_1}{\lambda_2} = 32$ dB, or 1600:1, which is in agreement with the approximate formula for $\frac{\pi_1}{\pi_2} = 0$ dB and $\eta$ less than 0.10 (or $-10$ dB). Ottersten's results indicate that the degradation from using unit weights is a five-time increase in the DOA standard deviation for the four sensors case and a three-time increase for 10 sensors case.

The next uncorrelated scenario used by Ottersten is for two unequal-SNR arrivals at 30 and 0 dB and spaced much farther apart at 0° and 15° from the broadside. For the most stringent

---

[1] Recall the discussions from section 4.1, the effective aperture of the approximating ULA should be a 24° arc length instead of a 21° one.

case of a three-element half-wavelength spacing ULA, this is about 40% fractional beamwidth. From figure 4.3, we find from $\eta = 1 - |\phi|^2$ vs fractional beamwidth for the three-element case the value of $\eta = -3$ dB, roughly. This can also be obtained from the approximate formula for closely spaced arrivals as $\frac{2}{6}(\pi \times 0.4)^2 \approx 0.48$. Then, we read from the curve for $\frac{\pi_1}{\pi_2} = 0$ dB in figure 5.33 with $\eta$ in direct scale the value of $\frac{\lambda_1}{\lambda_2} = 33$ dB. This can also be obtained from the approximate formula which is valid for $\frac{\pi_1}{\pi_2} > 10$ dB. So, the optimum weight ratio is about 2000:1.

In addition to the higher DOA standard deviation for using the unit weights, the much more offending and eye-catching phenomenon [38, page 68] is the roller-coaster behavior of the standard deviation curve as a function of the number of sensors. That is, the performance can degrade by adding more sensors. This has been found by Ottersten [38, page 69] as highly correlated with the sidelobe behavior of the ULA. Unlike the previous example where the two arrivals stay within the mainlobe, here each arrival gets farther and farther into the sidelobes of the other as more sensors are used. Our plot of the normalized inner product of the two steering vectors agree with Ottersten's plot, but the $\frac{\lambda_1}{\lambda_2}$ ratio curve has the maxima of 34.5 dB and exhibits only 0.5 dB ripples. Evidently, the asymptotic standard deviation expression is closely, if not exactly, proportional to this normalized inner product. This is beyond the scope of our approach, where only noise-free simplification is used.

As this defect of the unit weight has the close relation to the sidelobe phenomena, it probably will not be prominent for a random array. However, the drawback of not using appropriate weighting will be always present and manifested by the deterioration of the DOA standard deviation, especially when high $\frac{\lambda_1}{\lambda_2}$ contrast is there.

## 6.3 Temporally Highly Correlated Arrivals

Ottersten provided two additional scenarios using equal-SNR partially but highly correlated arrivals. This is contrasted to the either 0%- or 100%-correlated and equal-SNR arrivals typically used by Cadzow. Here Ottersten's results are displayed as standard deviation versus SNR. We need to know more about the multipath correlation beyond the magnitude, especially for the case of equal SNRs where the variable $\zeta$ involving the phase term has its most effect. During the discussion of these scenarios, we will first tentatively assume that the phase difference between the two equal-SNR multipaths as 90° and at the end adjust the eigenvalue ratio as we move to the 0° correlation. For these highly correlated equipower arrivals, we have shown in section 5.3 that the effect on the eigenvalue ratio from changing the phase of the source correlation from 90° to 0° can be as high as a four-time or 6-dB increase.

Partial correlation of 99% yields a partial contribution to $\eta$ of $-17$ dB, as $1 - |0.99|^2 \approx 2(1 - |0.99|) = 0.02$. The separation of two DOAs of 7° for a half-wavelength spacing ULA corresponds roughly to $\theta_{frac\_bw} = 0.2$ beamwidth, which contributes about $-9$ dB stress as read off from figure 4.3. This can also be obtained from the approximate formula for closely spaced arrivals as $\frac{2}{6}(\pi \times 0.2)^2 \approx 0.12$. Therefore, we have $\eta = -26$ dB because $\eta$ is exactly multiplicative, or additive in dB, in its two contributing factors, i.e., the multipath correlation part and the closeness of the two steering vectors of the DOAs. So, the eigenvalue contrast here for the noise-free scenario can be read from the curve for $\frac{\pi_1}{\pi_2} = 0$ dB in figure 5.29 using $\eta = -26$ dB as $\frac{\lambda_1}{\lambda_2} = 32$ dB or 1600:1. This is in agreement with the approximate formula valid for $\frac{\pi_1}{\pi_2} = 0$ dB and $\eta$ less than $-10$ dB. After the full 4-dB adjustment needed for the 0° temporal correlation, we have $\frac{\lambda_1}{\lambda_2} = 36$ dB or 4000:1. For moderate SNRs such as those about 0 dB ones, the deterioration of the Det-ML with respect to WSF starts to be noticeable as compared to the lack of distinction

between the two at higher SNRs. This will be elaborated in the next paragraph. The degradation of the unit weighting from that of the optimal one is more than one order of magnitude.

Partial correlation of 90% yields a partial contribution to $\eta$ of –7 dB, as $1 - |0.90|^2 \approx 2(1 - |0.90|) = 0.2$. The 40°-wide separation of two DOAs corresponds roughly to 1.3 beamwidth for a four-sensor ULA which contributes about 0-dB stress as shown from figure 4.7. So, the stress is almost entirely from the partial correlation in the noise-free simplification. Therefore, we have $\eta = -7$ dB or 0.2. This is in agreement with the approximate formula valid for $\frac{\pi_1}{\pi_2} = 0$ dB and $\eta$ less than –10 dB. The eigenvalue contrast here for the noise-free scenario can be read from the curve for $\frac{\pi_1}{\pi_2} = 0$ dB in figure 5.33 with $\eta$ in direct scale using $\eta = -7$ dB as $\frac{\lambda_1}{\lambda_2} = 13$ dB or 200:1. Ottersten used fairly low SNR but a large number of snapshots to distinguish the optimal weights were used from the more intuitive MLE weights. For large SNRs, these two different choices of weights do not have significantly different values. Therefore, this choice may not be important in the HFDF scenarios. But as SNRs decrease, the magnitude of these two different sets of weights depart, and the superiority of the optimal WSF algorithm over the Det-ML gets more pronounced. Any preference of the optimal weights over the more intuitive MLE weights in the passive sonar context is also questionable: to estimate the location of threshold signals, the number of signals must be determined. None of these highly parametric direction-finding algorithms is suitable for threshold signals.

## 6.4 Temporally 100%-Correlated Arrivals

So far, we have contrasted the Monte Carlo simulation comparison results of some of Cadzow's 0%-correlated scenarios and the comparison results of both the Monte Carlo simulation and the asymptotic performance prediction of some Ottersten's uncorrelated and partially correlated scenarios. We found it useful to assess the severity of their scenarios in terms of the noise-free eigenvalue distribution for the two discrete arrivals.

However, such assessment fails when the small eigenvalue for the noise-free simplification is zero, such as the case for the 100%-correlated arrival case which was discussed by Cadzow. Secondly, there is some qualitative discrepancy between the asymptotic and simulation results for the tradeoffs for high-SNR-scenario cases for the 100%-correlation cases between the Det-ML and WSF methods. The asymptotic results cannot differentiate the performances of these two methods by just judging from the weight expressions. Ottersten did not provide any asymptotic and simulation results for the 100%-correlation cases. Whereas Cadzow's simulation results for some 100%-correlated arrival cases indicated that even the unit weighting signal eigenvector method outperform the Det-ML method. For the single dominant eigenvector case, there is no weighting involved at all, consequently there should be no difference between Cadzow's signal eigenvector method and the WSF method.

As the asymptotic Det-ML for the high-SNR case approaches the CRLB, it is puzzling to see how this bound for an unbiased estimator can be exceeded. Ottersten believes that apparently this is because of the longer time it takes for the finite sample size bias to diminish in Det-ML than WSF. Asked to provide some plausible explanations for the reason that the signal eigenvector type methods outperform the Det-ML one, Ottersten thinks that this is because of the rank-reduction advantage provided in using only the dominant eigenvectors. While the original rank-reduction idea was suggested by Scharf and Tufts [47] and Scharf [48] in some different context, they did point out the potential applications to DF.

We can see readily that Cadzow's results fitting two 100%-correlated signals with a single eigenvector was not bad at all. Furthermore, when only one eigenvector is involved, the weighting

of eigenvectors is irrelevant, i.e., the unweighted signal eigenvector and WSF methods are identical. On the other hand, the results from using nonlinear least squares fit to the two unweighted eigenvectors as reported in the two scenarios of the 90%- or 99%-correlated DOAs by Ottersten was disastrous. Ottersten pointed out that in these cases, any consistent detection scheme will detect two arrivals given enough samples. He also pointed that there is a discontinuity in performance at 100% correlation for the unweighted signal eigenvector method, whereas WSF does not.

When a "dominant eigenvalue" becomes difficult to be distinguished from noise level ones, one would intuitively choose not to use it. This is based on the conjecture that retaining this marginally signal eigenvector and using the nonlinear least squares fit to it with an additional linear combination of steering vectors corresponding to the unknown DOAs probably will do more harm than help. Scharf and Tufts gave such practices more legitimate reasoning. Consequently, the problem of deciding the optimal number of signal eigenvectors to be used in practice may not be a simple one.

# Chapter 7

# Conclusions

After describing the scope of the report, chapter 1 starts with a survey of NB DF algorithms for general sensor arrays in element space. This includes a taxonomy table, characterization and asymptotic performance of the main algorithm categories, and the initialization procedure which is the critical item of most high-resolution algorithms. Then, formulating guidelines desired for DF scenario design are developed via the following items: too many parameters for a two-source DF scenario for a given sensor array, simple map(s) to show relative positions of scenarios, yardsticks for measuring stress of scenarios to direction-finding algorithms, and dominant eigenvalues chosen as the key items. Next, we discuss eigenvalues for the noise-free covariance matrix of two discrete sources through the following issues: treatment of this subject in Hudson's text, the original 6-dimensional parameter space for a given sensor array under the noise-free assumption, compact map(s) – another many-to-one reduction, and 3-d map with power ratio $\frac{\pi_1}{\pi_2}$ as third coordinate.

Chapter 2 addresses the notion of stress to direction-finding algorithms and scenarios. First, the three main sources for the signal eigenvalue spread or causes for small signal eigenvalues are reviewed: high spatial and/or temporal correlation and/or high contrast of signal strength between the two arrivals. Next, the eigenvalues in weighting expressions are discussed in three categories: in noise subspace methods, in parametric signal subspace fitting methods, and in non-parametric subspace adaptive beamforming. Then, the drawbacks of the oversimplifying stress-measuring yardstick using condition numbers are mentioned: infinite condition number for all 100%-correlated two arrivals, equal condition numbers corresponding to different CRLBs, CRLB not appealing to intuitive expectation sometimes, and the redeeming value for condition number. At the end, we explain the reasons why special treatment is given for equal-power arrivals and the complementary value of direct-scale and dB-scale plots.

The analytical chapter 3 begins by reviewing the expressions of the eigenvalues of the quadratic characteristic equations of the non-Hermitian product of the temporal- and spatial-correlation matrix. The eigenvalues are normalized with respect to the product of the number of sensors and the sensor level power of the weaker source $\pi_2$. The normalized large and small eigenvalues expressions $\lambda_1$ and $\lambda_2$ are reduced to forms depending only on the real triplet $(\xi, \eta, \frac{\pi_1}{\pi_2})$. Here, $\frac{\pi_1}{\pi_2}$ is the power ratio between the strong and weak sources at the sensor level. The real pair $(\xi, \eta)$ are defined in terms of the normalized temporal- and spatial-coefficients $\rho$ and $\phi$ respectively with each constrained to a unit-disk through

$$\eta = (1 - |\phi|^2)(1 - |\rho|^2),$$

$$\xi = \mathrm{Re}(\rho\phi^*) = |\rho||\phi|\cos(\arg\rho - \arg\phi).$$

While the discussions of eigenvalues in this report are applicable to generic steering vectors, we call $\eta$ the phase-independent variable and $\xi$ the phase-dependent variable for convenience even though such names were motivated by the special case of plane waves impinging onto pairwise symmetric arrays. The phase-independent variable $\eta$ depends only on the magnitude of $\rho$ and $\phi$. The phase-dependent variable $\xi$ depends also on the angular positions of $\rho$ and $\phi$. The mapping from the complex pair $(\rho, \phi)$ to the real pair $(\xi, \eta)$ is many-to-one. The range of this mapping is an isosceles-right-triangle-like region bounded on its left and right by two symmetric parabolas meeting each other at 90° and down below by a straight baseline. We characterize this region thoroughly with respect to the temporal and spatial coefficients of direction-finding scenarios.

Most of this report is devoted to characterizing the behavior of the eigenvalues and their ratio $\frac{\lambda_1}{\lambda_2}$ as functions of the real triplet $(\xi, \eta, \frac{\pi_1}{\pi_2})$. For convenience, we jointly summarize chapter 3, which is mainly on the eigenvalue analysis, and chapter 5, which is mainly on the eigenvalue ratio's display. After the expressions for the eigenvalue and their ratio $\frac{\lambda_1}{\lambda_2}$ for the special cases at the apex, the baseline, and the vertical axis were discussed, we thoroughly characterize the special case of equal-strength arrivals and then the general case.

The special case of equal strength $\frac{\pi_1}{\pi_2} = 0$-dB arrivals share the following common features of general $\frac{\pi_1}{\pi_2}$ power ratios: straight line contours for constant eigenvalue $\lambda$, parabolic $\lambda$ slices for constant phase-dependent variable $\xi$, hyperbolic $\lambda$ slices for constant phase-independent variable $\eta$, and parabolic contours for eigenvalue ratio $\frac{\lambda_1}{\lambda_2}$.

The special case of equal strength $\frac{\pi_1}{\pi_2} = 0$-dB arrivals merits unique attention because of the following. There is an extra 6 dB for signal eigenvalue ratio $\frac{\lambda_1}{\lambda_2}$ over the vertical axis $\xi = 0$, accounting for the presence of an infinite slope of $\lambda$ with respect to $\eta$ at the apex for the equal-power arrival case. This is reflected in the following two approximations. When $\frac{\pi_1}{\pi_2} > 10$ dB, we have

$$\frac{\lambda_1}{\lambda_2}(\text{in dB}) \approx (\frac{\pi_1}{\pi_2})(\text{in dB}) - \eta(\text{in dB}).$$

When $\frac{\pi_1}{\pi_2} \approx 0$ dB and $\eta$ is less than 0.10 (or $-10$ dB), we have

$$\frac{\lambda_1}{\lambda_2}(\text{in dB}) \approx -\eta(\text{in dB}) + 6.$$

Furthermore, for the special case of equal strength $\frac{\pi_1}{\pi_2} = 0$ dB arrivals, the contours of the eigenvalue ratio $\frac{\lambda_1}{\lambda_2} = l$ form a one-parameter family of parabolas having their vertices colocated at $(\xi, \eta) = (-1, 0)$, i.e., at the lower left corner of the isosceles-like triangle and their common tangent the baseline $\eta = 0$. This family include the left boundary of the isosceles-like triangle and the baseline. Because the contours of the eigenvalue ratio $\frac{\lambda_1}{\lambda_2} = l$ pass through the lower left corner of the isosceles-like triangle, this corner is a point of discontinuity for the eigenvalue ratio $\frac{\lambda_1}{\lambda_2}$ for the special case of equal strength $\frac{\pi_1}{\pi_2} = 0$ dB. For example, the two eigenvalues are equal over the left parabolic boundary of the isosceles-right-triangle-like region. Furthermore, the two equally dominant eigenvalues can go down to zero jointly so that the condition number stays as unity throughout. That is, the condition numbers are the lowest possible there. However, both eigenvalues tend to zero as $\eta$ tends to zero, i.e., the baseline of the region.

As power ratio $\frac{\pi_1}{\pi_2}$ increases from unit value, the variation of the large eigenvalue $\lambda_1$ is essentially along the direction of the horizontal phase-dependent variable $\xi$, and that the small eigenvalue $\lambda_2$ essentially along the direction of the vertical phase-independent variable $\eta$.

There is a four-time or 6-dB increase on the eigenvalue ratio $\frac{\lambda_1}{\lambda_2}$ for highly correlated equipower arrivals, both temporally and spatially, from changing the phase of the source correlation or the angle difference between the two unit-disk vectors from 90° to 0°.

The smaller eigenvalue $\lambda_2$ is independent of both the horizontal phase-dependent variable $\xi$ and $\frac{\pi_1}{\pi_2}$ near the baseline for large $\frac{\pi_1}{\pi_2}$, but is a strong function of the vertical phase-independent variable $\eta$. The effect of $\frac{\pi_1}{\pi_2}$ is essentially only felt by the large eigenvalue which is not sensitive to whether the scenario's $(\xi, \eta)$ coordinate is close to the baseline, i.e., whether the arrivals are correlated or close to each other as far as its order of magnitude is concerned.

We also characterize Speiser's eigenvalue bounds specialized to the two-source scenario. These bound expressions involve only the absolute magnitude of the two phasors on the two unit-disks, i.e., only the radius but not the argument of the phasors. Interestingly enough, his two bounds for the equipower case can be identified as the eigenvalue values at the two extreme ends of the permissible phase-dependent variable $\xi$-interval on the constant phase-independent $\eta$ horizontal line of the isosceles region with all expressions calculated from the magnitudes of $\rho$ and $\phi$ only. For given $\eta$, the permissible $\xi$-interval attains its maximum width when the $\xi$-interval extends from the left to the right boundary parabola. The length of such maximum $\xi$-interval increases with decreasing $\eta$, i.e., when the baseline is approached. The bounds for the small eigenvalue may be loose when there is considerable variation in the order of magnitude of the small eigenvalue in the phase-dependent variable $\xi$. For large $\frac{\pi_1}{\pi_2}$, the smaller eigenvalue $\lambda_2$ becomes more independent of the horizontal phase-dependent variable $\xi$, the bounds will get tighter. That is, there is less information loss by neglecting the phase-dependent variable $\xi$.

Even though we assess only those algorithms applicable to general sensor array configurations, we still need to understand the results about plane waves impinging on a ULA, especially those simulation results which could be expensive to duplicate for general arrays. Chapter 4 discusses fractional beamwidth measurement for arrival separation and the smaller eigenvalue $\lambda_2$'s negligible dependence on the number of elements N after using $\theta_{frac\_bw}$ for the equipower uncorrelated case.

In chapter 6, we apply all the previously developed results to assess some scenarios used by Cadzow and Ottersten. For temporally uncorrelated arrivals, we found that the $\frac{\lambda_1}{\lambda_2}$ ratios used by Ottersten for his ULA scenarios are typically in the area of 30 dB, i.e., 1000:1, or more, whereas the mill-cross example used by Cadzow need an optimum weight ratio like 40:1. This explains why different conclusions were drawn by them. The tradeoffs conducted by Cadzow were mainly between his (unweighted) algorithm and Det-ML. The unweighted algorithm was outperformed by Det-ML but not by much. Ottersten's results indicate that the degradation from using unit weights is a 5-time increase in the DOA standard deviation for a 4-sensor case and a 3-time increase for a 10-sensor case. However, in addition to the higher DOA standard deviation for using the unity weights, the much more offending and eye-catching phenomenon is the roller-coaster behavior of the standard deviation curve as a function of the number of sensors. That is, the performance can degrade by throwing more sensors. This has been found by Ottersten as highly correlated with the sidelobe behavior of the ULA.

We also commented on Ottersten's scenarios of temporally highly correlated arrivals and Cadzow's scenarios of temporally 100%-correlated arrivals. For the latter case, the eigenvalue ratio $\frac{\lambda_1}{\lambda_2} = \infty$ and the attempt to assess the severity of their scenarios via the noise-free eigenvalue ratio for the two discrete arrivals fails. There is some qualitative discrepancy between the asymptotic and simulation results for the tradeoffs for high-SNR scenario cases for the 100% correlation cases between the Det-ML and WSF methods. The asymptotic results cannot differentiate the performances of these two methods just judging from the weight expressions. Ottersten did not provide any asymptotic and simulation results for the 100% correlation cases. Whereas Cadzow's simulation results for some 100%-correlated arrival cases indicated that even the unity weighting signal eigenvector method outperform the Det-ML. Ottersten conjectured that the rank-reduction idea by Scharf and Tufts may answer such difference

# Glossary

| | |
|---|---|
| ABF | Adaptive Beamforming |
| ASSP | Acoustic, Speech, and Signal Processing Society |
| BW | BeamWidth |
| CBF | Conventional BeamForming |
| CRLB | Cramer-Rao Lower-Bound |
| dB | decibel |
| Det-ML | Deterministic Maximum Likelihood |
| Det-MLE | Deterministic Maximum Likelihood Estimation |
| DF | Direction-Finding |
| DOA | Directions Of Arrivals |
| EM | Expectation-Maximization |
| EMVDR | Enhanced Minimum Variance Beamforming |
| ESPRIT | Estimation of Signal Parameters via Rotational Invariance Techniques |
| HFDF | High-Frequency Direction-Finding |
| HFM | Hyperbolic Frequency Modulated |
| IEEE | The Institute of Electrical and Electronic Engineers, Inc. |
| LFM | Linear Frequency Modulated |
| LPM | Logarithmic Period Modulated |
| MD | MultiDimensional |
| MFP | Matched-Field Processing |
| MUSIC | MUltiple SIgnal Classification |
| MVDR | Minimum Variance Distortionless Response |
| NB | NarrowBand |
| PCI | Principal Component Inverse |
| SBR | Signal to background ratio |
| SE | Signal Eigenvector |
| SINR | Signal to Interference and Noise Ratio |
| SMI | Sampled Matrix Inverse |
| SNR | Signal-to-Noise Ratios |
| Sto-ML | Stochastic Maximum Likelihood |
| Sto-MLE | Stochastic Maximum Likelihood Estimation |
| ULA | Uniform Line Array |
| WSF | Weighted Subspace Fitting |

# References

[1] Abraham, D. and N. Owsley. "Preprocessing for High Resolution Beamforming." in *Conference Record of the $23^{rd}$ Asilomar Conf on Signals, Systems and Computers*, Pacific Grove, CA, Oct 30-Nov 1, 1989.

[2] Abraham, D. and N. Owsley. "Beamforming with Dominant Mode Rejection," in *Oceans 90 Conference*, Arlington, Virginia, Sep 1990.

[3] Barabell, A.J., J. Capon, D.F. Delong, J.R. Johnson, and K. Senne. *Performance Comparison of Superresolution Array Processing Algorithms*, Tech. Rep. TST-72, Lincoln Laboratory, M.I.T., May 1984.

[4] Box, G.E.P. and G.C. Tiao. *Bayesian Inference in Statistical Analysis*, Addison-Wesley, 1973.

[5] Burdic, W.S. *Underwater Acoustic System Analysis*, Prentice-Hall, Inc., Englewood, N.J., 1984.

[6] Cadzow, J.A. "A High Resolution Direction-of-Arrival Algorithm for Narrow-band Coherent and Incoherent Sources," *IEEE ASSP*, vol 36, no.7, Jul 1988.

[7] Cadzow, J.A., Y.S. Kim, and D.C. Shiue. "General Direction-of-Arrival Estimation: A Signal Subspace Approach," *IEEE AES*, vol. 25, no.1, Jan 1989.

[8] Cadzow, J.A. *Progress Report no.4 for the NOSC Contract on Analysis, Development and Simulation of High Frequency Direction Finding Techniques and Systems*, Sep 14, 1989.

[9] Cadzow, J.A. "Multiple Source Location: The Signal Subspace Approach," in *Conference Record of the $23^{rd}$ Asilomar Conf on Signals, Systems and Computers*, Pacific Grove, CA, Oct 30-Nov 1, 1989.

[10] Cadzow, J.A. "Multiple Source Location—The Signal Subspace Approach," *IEEE ASSP*, vol 38, no.7, Jul 1990.

[11] Chou, S.I. *Hyperbolic Frequency Modulated (HFM) Waveforms and Wavetrains*, Technical Report 1259, Naval Ocean Systems Center, Aug 1988.

[12] Clark, M.P. and R.A. Roberts. "Real-Time Adaptive Beamforming Using Rank-One Eigenstructure Updating," pp.79-83, in *Conference Record of the $23^{rd}$ Asilomar Conf on Signals, Systems and Computers*, Pacific Grove, CA, Oct 30-Nov 1, 1989.

[13] Cox, H. "Resolving Power And Sensitivity To Mismatch Of Optimum Array Processors," *J. Acoust. Soc. Am.*, vol. 54, no.3, pp.771-785, 1973.

[14] Degerine, S., "On Local Maxima of the Likelihood Function for Toeplitz Matrix Estimation," submitted to *IEEE ASSP*.

[15] Evans, J.E., J.R. Johnson, and D.F. Sun. *Application of Advanced Signal Processing Techniques to Angle of Arrival Estimation in ATC Navigation and Surveillance Systems*, TR 582, Lincoln Laboratory, M.I.T., Jun 1982.

[16] Farrier, D. and L. Prosper. "A Signal Subspace Beamformer," in *Proc ICASSP 90, 1990 Intl Conf on Acoustics, Speech, and Signal Processing*, pp.2815-1818, Apr 3-6, 1990.

[17] Farrier, D. "Detection of Arrival Estimation by Subspace Method," in *Proc ICASSP 90, 1990 Intl Conf on Acoustics, Speech, and Signal Processing*, pp.2651-2654, Apr 3-6, 1990.

[18] Ferrara, E. and T. Parks. "Direction Finding with an Array of Antennas Having Diverse Polarizations," *IEEE Transactions on Antennas and Propagation*, vol. AP-31, no. 3, Mar 1983.

[19] Friedlander,B. "Adaptive Beamforming for Large Arrays," in *Conference Record of the $22^{nd}$ Asilomar Conf on Signals, Systems and Computers*, pp.44-48, Monterey, CA, Nov 1988.

[20] Golub, G.H. and V. Pereyra. "The Differentiation of Pseudoinverses and Nonlinear Least Squares Problems Whose Variables Separate," *SIAM Journal on Numerical Analysis*, 10, 1973, pp.413-432.

[21] Haber, F. and M.D. Zoltowski. "A Vector Space Approach to Direction Finding in a Coherent Multipath Environment," *IEEE Transactions on Antennas and Propagation*, vol. AP-34, no. 9, Sep 1986.

[22] Haykin, S. "Radar Array Processing for Angle of Arrival Estimation," in *Array Signal Processing*, ed., S. Haykin, Prentice-Hall, Englewood Cliffs, N.J., chap. 4, 1985.

[23] Hudson, J.E. *Adaptive Array Principles*, Peter Peregrinus Ltd., London, 1981.

[24] Hung, E.K.L., R.M. Turner, and R.W., Herring. "A Pitfall in Using the Pseudoinverse of a Singular Covariance Matrix in Adaptive Signal Processing," *ASSP Workshop on Spectrum Estimation*, pp.253-258, 1983.

[25] Johnson, D.H. and S.R. DeGraaf. "Improving the Resolution of Bearing in Passive Sonar Arrays by Eigenvalue Analysis," *IEEE Trans. ASSP*, vol. ASSP-30, pp.638-647, 1982.

[26] Kaufman, L. "A Variable Projection Method for Solving Separable Nonlinear Least Squares Problems," *BIT*, 15, 1975, pp.49-57.

[27] Kaveh, M. and A.J. Barabell. "The Statistical Performance of the MUSIC and the Minimum-Norm Algorithms in Resolving Plane Waves in Noise," *IEEE ASSP*, vol. 34, no. 2, Apr 1986.

[28] Kirsteins, I.P. and D.W. Tufts. "On the Probability Density of Signal-to-Noise Ratio in Improved Detector," in *Proc ICASSP 85, 1985 Intl Conf on Acoustics, Speech, and Signal Processing*, pp.572-575, Mar 1985, Tampa, Florida.

[29] Kirsteins, I.P. and D.W. Tufts. "Rapidly Adaptive Nulling of Interference," invited paper presented at the G.R.E.T.S.I. Conference at Juan-les Pins, France, Jun 12-16, 1989, to appear in *Lecture Notes in Control and Information Sciences*, Springer Verlag.

[30] Kwon, B.H. and S.U. Pillai. "New Resolution Threshold Results in Three Source Scenes," in *Conference Record of the 23$^{rd}$ Asilomar Conf on Signals, Systems and Computers*, Pacific Grove, CA, Oct 1989.

[31] Lo, J.T., N.K. Nagaraj, and A. Rukhin. "Cyclic Regression for Weighted Subspace Fitting to Find Multiple Signal Directions," in *Oceans 90 Conference*, Arlington, Virginia, Sep 1990.

[32] Martin, G.E. "Signal Subspace Processing Of Experimental Radio Data," in *Proc. of the SPIE: Advanced Algorithms & Architectures for Signal Processing III*, SPIE vol. 975, Aug 1988, pp.101-107.

[33] Munier, J. G.Y. Delisle. "A New Algorithm for the Identification of Distorted Wavefronts," in *Proceedings of NATO ASI, Underwater Acoustics*, pp.87-92, Jul 18-29, 1988, Kingston, Ontario, Canada.

[34] Ottersten, B. and M. Viberg. "Asymptotic Results for Multidimensional Sensor Array Processing," in *Proc. 22$^{nd}$ Asilomar Conf. Sig., Syst., Compt.*, pp.833-837, Monterey, CA, Nov 1988.

[35] Ottersten, B. and M. Viberg. "Analysis of Subspace Fitting Based Methods for Sensor Array Processing," in *Proc ICASSP 89, 1989 Intl Conf on Acoustics, Speech, and Signal Processing*, pp.2807-2810, Glasgow, Scotland, May 1989.

[36] Ottersten, B. and L. Ljung. "Asymptotic Results for Sensor Array Processing," in *Proc ICASSP 89, 1989 Intl Conf on Acoustics, Speech, and Signal Processing*, pp.2266-2269, Glasgow, Scotland, May 1989.

[37] Ottersten, B. Letter to S.I. Chou of NOSC, dated August 17, 1989.

[38] Ottersten, B. *Parametric Subspace Fitting Methods for Array Signal Processing*, PhD thesis, Stanford University, Stanford, CA, Dec 1989.

[39] Owsley, N.L. "Enhanced Minimum Variance Beamforming," in *Underwater Acoustic Data Processing*, Ed. by Y.T. Chan, NATO ASI Series, series E: Applied Science–vol.161, Kluwer Academic Publishers, 1989, pp.285-292.

[40] Pillai, S.U. *Array Signal Processing*, Springer-Verlag, New York, 1989.

[41] Reilly, J.P. and S. Haykin. "Maximum-Likelihood Receiver for Low-Angle Tracking Radar, Part 1: The Symmetric Case," *IEE Proc.*, vol 129, Pt.F, no.4, Aug 1982.

[42] Reilly, J.P. and S. Haykin. "Maximum-Likelihood Receiver for Low-Angle Tracking Radar, Part 2: The Nonsymmetric Case," *IEE Proc.*, vol 129, Pt.F, no.5, Oct 1982.

[43] Reilly, J.P., W.G. Chen, and K.M. Wong. "Fast QR-Based Array Processing Algorithm," in *Proc. of the SPIE: Advanced Algorithms & Architectures for Signal Processing III*, SPIE vol. 975, 15-17 Aug 1988, San Diego, CA.

[44] Reilly, J.P., K.M. Wong, and P.M. Reilly. "Direction Of Arrival Estimation In The Presence Of noise With Unknown, Arbitrary Covariance Matrices," in *Proc. of the SPIE: Advanced Algorithms & Architectures for Signal Processing IV*, SPIE vol. 1152, Dec 1989.

[45] Roy, R. *Estimation of Signal Parameters via Rotational Invariance Techniques*, PhD thesis, Stanford University, Stanford, CA, Aug 1987.

[46] Ruhe, A. and P.A. Wedin. "Algorithms for Separable Nonlinear Least Squares Problems," *SIAM Review*, 22, 1980, pp.318-337.

[47] Scharf, L.L. and D.W. Tufts. "Rank Reduction for Modeling Stationary Signals," *IEEE ASSP*, vol. 35, no.3, pp.350-355, Mar 1987.

[48] Scharf, L.L. "Topics in Statistical Signal Processing," in *Signal Processing*, Eds. J.L. Lacoume, T.S. Durrani, and R. Stora, Course 2, 85-203, Elsevier Science Publishers, 1987.

[49] Schmidt, R.O. *A Signal Subspace Approach to Multiple Emitter Location and Spectral Estimation*, PhD thesis, Stanford University, Stanford, CA, Nov 1981.

[50] Schmidt, R.O., "Multilinear Array Manifold Interpolation," to appear in *IEEE ASSP*.

[51] Speiser, J. and H.B. Arnold. "Array Manifold Effects in Subspace Techniques," in *Proc. of the SPIE: Advanced Algorithms & Architectures for Signal Processing IV*, SPIE vol. 1152, Dec 1989.

[52] Steinberg, B.D. *Principles of Aperture and Array System Design*, John Wiley & Sons, New York, 1976.

[53] Stoica, P. and A. Nehorai. "MUSIC, Maximum Likelihood, and Cramer-Rao Bound," *IEEE ASSP*, vol. 37, no.5, May 1989.

[54] Stoica, P. and A. Nehorai. "MUSIC, Maximum Likelihood, and Cramer-Rao Bound: Further Results and Comparisons," *IEEE ASSP*, vol. 38, no.12, Dec 1990.

[55] Stoica, P. and A. Nehorai. "Performance Study of Conditional and Unconditional Direction-of-Arrival Estimation," *IEEE ASSP*, vol. 38, no.10, Oct 1990.

[56] Stoica, P. and K.C. Sharman. "Maximum Likelihood Methods for Direction-of-Arrival Estimation," *IEEE ASSP*, vol. 38, no.7, Jul 1990.

[57] Swindlehurst, A.L., T. Kailath. "An Analysis of Subspace Fitting Algorithms in the Presence of Sensor Errors," in *Proc ICASSP 90, 1990 Intl Conf on Acoustics, Speech, and Signal Processing*, Apr 3-6, 1990, pp.2647-2650.

[58] Tran, C.V. "Asymptotic Covariance Matrices of Estimation Error Using a Uniform Linear Array," to appear in *Conference Record of the $24^{th}$ Asilomar Conf on Signals, Systems and Computers*, Nov 6-8, 1990, Pacific Grove, CA.

[59] Viberg, M. and B. Ottersten. "Sensor Array Processing Based on Subspace Fitting," Submitted to *IEEE ASSP*, Jan 30, 1989.

[60] Viberg, M., B. Ottersten, and T. Kailath. "Detection and Estimation in Sensor Arrays Using Weighted Subspace Fitting," Submitted to *IEEE ASSP*, Jul 21, 1989.

[61] Viberg, M. *Subspace Fitting Concepts in Sensor Array Processing*, PhD thesis, Linkoping University, Linkoping, Sweden, Oct 1989.

[62] Wu, Q. *Array Signal Processing with Low Signal to Noise Ratio*, PhD thesis, Washington University. Sever Institute of Technology, St. Louis, Missouri, Dec 1989.

[63] Ziskind, I. and M. Wax. "Maximum Likelihood Estimation of Directions of Arrivals of Narrowband Signals in Noise," *IEEE ASSP*, vol.36, no.10, pp.1553-1560, Oct 1988.

[64] Ziskind, I. and M. Wax. "Resolution Enhancement by Periodicity Constraints," *IEEE ASSP*, vol.38, no.4, pp.687-694, Oct 1988.

[65] Zoltowski, M.D. and D. Stavrinides. "Sensor Array Signal Processing via a Procrustes Rotations Based Eigenanalysis of the ESPRIT Data Pencil," *IEEE ASSP*, vol.37, no.6, pp.832-861, Jun 1989.

[66] Zoltowski, M.D. and T.S. Lee. "Maximum Likelihood Based Sensor Array Signal Processing In the Beamspace domain for Low Angle Radar Tracking," *IEEE ASSP*, vol.39, no.3, pp.656-671, Mar 1991.

# Appendix A

# Hyperbola Derivation and Characterization

In the general case discussion, we asserted without proof that for constant $\eta$ slices the characteristic equation can be rearranged to that of a hyperbola in $\lambda$ and $\xi$ as

$$\lambda^2 - \sqrt{\frac{\pi_1}{\pi_2}} 2\xi\lambda - (1 + \frac{\pi_1}{\pi_2})\lambda + \frac{\pi_1}{\pi_2}\eta = 0.$$

In this appendix, we will show that for each $\frac{\pi_1}{\pi_2}$ value, this equation describes a one-parameter $\eta$ family of hyperbolas in $\lambda$ and $\xi$, sharing common asymptotes.

Recall that in the discussion of the special case of $\eta = 0$, i.e., at the baseline, we have the following relations:

$$\lambda_2 = 0,$$

$$\lambda_1 = \frac{\pi_1}{\pi_2} + 1 + \sqrt{\frac{\pi_1}{\pi_2}} 2\xi.$$

When $\xi$ changes from $-1$ to $0$ to $+1$, $\lambda_1$ varies linearly in $\xi$ with the slope equal to $2\sqrt{\frac{\pi_1}{\pi_2}}$ from

$$(\sqrt{\frac{\pi_1}{\pi_2}} - 1)^2 \text{ to } (\frac{\pi_1}{\pi_2} + 1) \text{ to } (\sqrt{\frac{\pi_1}{\pi_2}} + 1)^2.$$

These two straight lines for $\lambda_1$ and $\lambda_2$ will turn out to be the common asymptotes of each family labeled with the particular $\frac{\pi_1}{\pi_2}$ value.

Following the usual treatment for reducing a general second-order plane curve to its canonical form, we make the following coordinate transform

$$\begin{bmatrix} \xi \\ \lambda \end{bmatrix} = \begin{bmatrix} \cos\theta & -\sin\theta \\ \sin\theta & \cos\theta \end{bmatrix} \begin{bmatrix} \Xi \\ \Lambda \end{bmatrix} + \begin{bmatrix} h \\ k \end{bmatrix} = \begin{bmatrix} \Xi\cos\theta - \Lambda\sin\theta + h \\ \Xi\sin\theta + \Lambda\cos\theta + k \end{bmatrix}.$$

Substituting into the original equation, we have

$$(\Xi\sin\theta + \Lambda\cos\theta + k)^2 - \sqrt{\frac{\pi_1}{\pi_2}} 2(\Xi\cos\theta - \Lambda\sin\theta + h)(\Xi\sin\theta + \Lambda\cos\theta + k)$$

$$-(1 + \frac{\pi_1}{\pi_2})(\Xi\sin\theta + \Lambda\cos\theta + k) + \frac{\pi_1}{\pi_2}\eta = 0.$$

This can be rewritten into the following form as

$$C_{\Lambda^2}\Lambda^2 + C_{\Xi\Lambda}\Xi\Lambda + C_{\Xi^2}\Xi^2 + C_\Lambda\Lambda + C_\Xi\Xi + c = 0,$$

with

$$C_{\Lambda^2} = \cos^2\theta + 2\sqrt{\frac{\pi_1}{\pi_2}}\sin\theta\cos\theta,$$

$$C_{\Xi\Lambda} = 2\sin\theta\cos\theta - 2\sqrt{\frac{\pi_1}{\pi_2}}(\cos^2\theta - \sin^2\theta),$$

$$C_{\Xi^2} = \sin^2\theta - 2\sqrt{\frac{\pi_1}{\pi_2}}\sin\theta\cos\theta,$$

$$C_\Lambda = 2k\cos\theta - 2\sqrt{\frac{\pi_1}{\pi_2}}(-k\sin\theta + h\cos\theta) - (1 + \frac{\pi_1}{\pi_2})\cos\theta,$$

$$C_\Xi = 2k\sin\theta - 2\sqrt{\frac{\pi_1}{\pi_2}}(k\cos\theta + h\sin\theta) - (1 + \frac{\pi_1}{\pi_2})\sin\theta,$$

$$c = k^2 - 2\sqrt{\frac{\pi_1}{\pi_2}}hk - (1 + \frac{\pi_1}{\pi_2})k + \frac{\pi_1}{\pi_2}\eta.$$

The rotation of coordinates is obtained by setting $C_{\Xi\Lambda} = 0$, i.e.,

$$\tan 2\theta = 2\sqrt{\frac{\pi_1}{\pi_2}}.$$

Using this result, we rearrange $C_{\Lambda^2}$ and $C_{\Xi^2}$ to see that what we are dealing with are indeed hyperbolas:

$$C_{\Lambda^2} = (1 + \cos 2\theta)/2 + \frac{\sin^2 2\theta}{2\cos 2\theta} = 1/2 + \frac{1}{2\cos 2\theta} > 1,$$

$$C_{\Xi^2} = (1 - \cos 2\theta)/2 - \frac{\sin^2 2\theta}{2\cos 2\theta} = 1/2 - \frac{1}{2\cos 2\theta} < 0.$$

The translation of coordinates is obtained by setting $C_\Lambda = 0$ and $C_\Xi = 0$, or

$$k(2 - 2\sqrt{\frac{\pi_1}{\pi_2}}\frac{1}{\tan\theta}) - h(2\sqrt{\frac{\pi_1}{\pi_2}}) = 1 + \frac{\pi_1}{\pi_2},$$

$$k(2 + 2\sqrt{\frac{\pi_1}{\pi_2}}\tan\theta) - h(2\sqrt{\frac{\pi_1}{\pi_2}}) = 1 + \frac{\pi_1}{\pi_2}.$$

Therefore $k = 0$, as $\tan\theta \neq \frac{1}{\tan\theta}$. We also get $h = -\frac{1}{2}(1 + \frac{\pi_1}{\pi_2})/\sqrt{\frac{\pi_1}{\pi_2}}$. This means that the new coordinate origin is at $(-\frac{1}{2}(1 + \frac{\pi_1}{\pi_2})/\sqrt{\frac{\pi_1}{\pi_2}}, 0)$, i.e., the intersection of the two straight lines for $\lambda_1$ and $\lambda_2$ introduced during the discussion of the special case of $\eta = 0$, i.e., at the baseline.

The remaining constant, c, is $\frac{\pi_1}{\pi_2}\eta$ or $(\frac{1}{2}\tan 2\theta)^2\eta$.

The hyperbola in the new coordinate system has the following form

$$(\frac{1}{2\cos 2\theta} - 1/2)\Xi^2 - (\frac{1}{2\cos 2\theta} + 1/2)\Lambda^2 = \frac{\pi_1}{\pi_2}\eta.$$

The asymptotes have the slopes of

$$\pm\sqrt{\frac{-C_{\Xi^2}}{C_{\Lambda^2}}} = \pm\sqrt{\frac{1 - \cos 2\theta}{1 + \cos 2\theta}} = \pm\tan\theta.$$

A-2

as expected.

The vertex distance from the new coordinate origin is $\Xi_V$ obtained from setting $\Lambda = 0$ as

$$(\Xi_V)^2 = (\frac{1}{2}\tan 2\theta)^2\,\eta\frac{2\cos 2\theta}{1-\cos 2\theta} = \frac{\sin 2\theta}{1-\cos 2\theta}\,(\frac{1}{2}\tan 2\theta)\eta = \frac{1}{1-\tan^2\theta}\eta$$

in terms of $\theta$, or

$$(\Xi_V)^2 = \frac{\cos 2\theta}{1-\cos 2\theta}\frac{\pi_1}{\pi_2}2\eta = \frac{(1+4\frac{\pi_1}{\pi_2})^{-\frac{1}{2}}}{1-(1+4\frac{\pi_1}{\pi_2})^{-\frac{1}{2}}}\frac{\pi_1}{\pi_2}2\eta$$

in terms of $\frac{\pi_1}{\pi_2}$.

For given $\theta$ or $\frac{\pi_1}{\pi_2}$, $\Xi_V$ is proportional to $\sqrt{\eta}$. That is, the rate of increase of $\Xi_V$ with respect to $\eta$ is $\infty$ at $\eta = 0$ and $\Xi_V$ at $\eta = \frac{1}{4}$ is already half of $\Xi_V$ at $\eta = 1$. We note that the useful vertices of these connected hyperbolas are over the boundary of the domain of interest only when $\frac{\pi_1}{\pi_2} = 1$. Without using many data points in the plotting and explicitly drawing the $\Xi$ axis, these aspects may not be easily observed from the plots.

# REPORT DOCUMENTATION PAGE

Public reporting burden for this collection of information is estimated to average 1 hour per response, including the time for reviewing instructions, searching existing data sources, gathering and maintaining the data needed, and completing and reviewing the collection of information. Send comments regarding this burden estimate or any other aspect of this collection of information, including suggestions for reducing this burden, to Washington Headquarters Services, Directorate for Information Operations and Reports, 1215 Jefferson Davis Highway, Suite 1204, Arlington, VA 22202-4302, and to the Office of Management and Budget, Paperwork Reduction Project (0704-0188), Washington, DC 20503

| 1 AGENCY USE ONLY *(Leave blank)* | 2 REPORT DATE | 3 REPORT TYPE AND DATES COVERED |
|---|---|---|
| | November 1990 | Final: Oct 1989—Sep 1990 |

| 4 TITLE AND SUBTITLE | 5. FUNDING NUMBERS |
|---|---|
| EIGENVALUES OF COVARIANCE MATRIX FOR TWO-SOURCE ARRAY PROCESSING | PE: 060211ːN<br>PROJ: 70–SXB2<br>SUBPROJ: RA11W54<br>ACC: ICSXB200 |
| 6 AUTHOR(S)<br>S. I. Chou | |

| 7 PERFORMING ORGANIZATION NAME(S) AND ADDRESS(ES) | 8 PERFORMING ORGANIZATION REPORT NUMBER |
|---|---|
| Naval Ocean Systems Center<br>San Diego, CA 92152–5000 | NOSC TR 1370 |

| 9 SPONSORING/MONITORING AGENCY NAME(S) AND ADDRESS(ES) | 10 SPONSORING/MONITORING AGENCY REPORT NUMBER |
|---|---|
| Naval Ocean Systems Center<br>San Diego, CA 92152–5000 | |

11 SUPPLEMENTARY NOTES

| 12a DISTRIBUTION/AVAILABILITY STATEMENT | 12b DISTRIBUTION CODE |
|---|---|
| Approved for public release; distribution is unlimited. | |

13 ABSTRACT *(Maximum 200 words)*

This report begins with a survey of narrowband direction-finding algorithms in element space. Then it discusses a simple stress measure to direction-finding algorithms applied to scenarios with two sources.

Eigenvalue weighting appears in some noise subspace methods, in parametric signal subspace fitting methods, and in nonparametric subspace adaptive nulling beamforming. For a two-source array-processing scenario, normalized large and small eigenvalues $\lambda_1$ and $\lambda_2$ are reduced to forms depending only on a real triplet: phase-dependent variable $\xi$, phase-independent variable $\eta$, and power ratio $\frac{\pi_1}{\pi_2}$. The pairs $(\xi, \eta)$ are confined to an isosceles-like region.

The main contribution of this work is a manageable presentation of a compact map showing $\lambda_1$, $\lambda_2$, and $\frac{\lambda_1}{\lambda_2}$ as functions of $\xi$, $\eta$, and $\frac{\pi_1}{\pi_2}$ over all possible scenarios. This enables one to see the relative positions among different scenarios. Presented also are some easy-to-remember formulas that enable one to exercise "back-of-envelope" assessment of scenarios.

The small eigenvalue is shown to diminish qualitatively and quantitatively for two-arrival scenarios increasingly stressed with high temporal and/or spatial correlations. The special case of equal-strength signal arrivals ($\frac{\pi_1}{\pi_2} = 1$), also important in low-angle radar tracking, shares many rich structures of general $\frac{\pi_1}{\pi_2}$. The equal-strength case also has several additional unique features for signal eigenvalue ratio $\frac{\lambda_1}{\lambda_2}$, which is important in direction-finding.

| 14 SUBJECT TERMS | | | 15 NUMBER OF PAGES |
|---|---|---|---|
| eigenvalues<br>direction-finding algorithms<br>parabolic slices | isosceles-like region<br>uniform line array (ULA)<br>sampled matrix inverse (SMI) | direction of arrival (DOA) | 113 |
| | | | 16 PRICE CODE |

| 17 SECURITY CLASSIFICATION OF REPORT | 18 SECURITY CLASSIFICATION OF THIS PAGE | 19 SECURITY CLASSIFICATION OF ABSTRACT | 20 LIMITATION OF ABSTRACT |
|---|---|---|---|
| UNCLASSIFIED | UNCLASSIFIED | UNCLASSIFIED | SAME AS REPORT |

| 21a. NAME OF RESPONSIBLE INDIVIDUAL | 21b. TELEPHONE  *(Include Area Code)* | 21c. OFFICE SYMBOL |
|---|---|---|
| S. I. Chou | (619) 553-2541 | Code 761 |

INITIAL DISTRIBUTION

BBN Systems & Technology Corporation
Arlington, VA   22209

Signal Proc Tech, LTD
Palo Alto, CA   94303

The MITRE Corporation
Bedford, MA   01730

Southwest Research, Inc.
San Antonio, TX   78284